Phonon Polariton Interaction with Patterned Materials

by

Eric R. Statz

B.S. Chemistry and B.S. Physics
Pennsylvania State University, 2001

SUBMITTED TO THE DEPARTMENT OF CHEMISTRY
IN PARTIAL FULFILLMENT OF THE REQUIREMENTS FOR
THE DEGREE OF

DOCTOR OF PHILOSOPHY IN CHEMISTRY

AT THE

MASSACHUSETTS INSTITUTE OF TECHNOLOGY

JUNE 2008

MASSACHUSETTS INSTITUTE OF TECHNOLOGY
JUN 10 2008
LIBRARIES

© Massachusetts Institute of Technology 2008. All rights reserved.

ARCHIVES

Author ....
Department of Chemistry
May 1, 2008

Certified by ....
Keith A. Nelson
Professor of Chemistry
Thesis Supervisor

Accepted by ....
Robert W. Field
Chairman, Department Committee on Graduate Students

This doctoral thesis has been examined by a committee of the Department of Chemistry as follows:

Professor Robert W. Field . . . .
Chairman

Professor Keith A. Nelson . . . .
Thesis Supervisor

Professor Jianshu Cao . . . .

Phonon Polariton Interaction with Patterned Materials

by

Eric R. Statz

Submitted to the Department of Chemistry
on May 1, 2008, in partial fulfillment of the
requirements for the degree of
Doctor of Philosophy in Chemistry

Abstract

The generation, propagation and detection of THz phonon polaritons are studied through both femtosecond pump-probe techniques, and Finite Difference Time Domain (FDTD) simulations in this thesis. The theory surrounding the driving, propagation and detection of these modes is treated in a consistent notational system for both analytical solutions and approximate simulated responses.

FDTD simulations in one, two and three dimensions are designed to best mimic lab experimental parameters, with various approximations of both THz pumping and probing developed. Various improvements on the FDTD method with the goal of more rapid simulations and more accurately described simulations of lab experiments from generation to detection are considered and developed.

Experiments on phonon-polaritons interacting with periodicity and confinement in one, two, and three dimensions are all considered, and methods of data processing developed. By comparing FDTD simulation results to experimental results, the full three dimensional fields within these crystals can be investigated, and in many cases fully defined.

The methods demonstrated open up new possibilities for THz spectroscopy in waveguides, microfluidics, and related platforms that include THz generation, propagation, interaction with the sample material, and detection in a compact, integrated structure. The methods also enable the proper description of large-amplitude THz generation and applications in nonlinear THz spectroscopy. Finally, linear and nonlinear THz signal processing applications my exploit the experimental and modeling methods described in this thesis.

Thesis Supervisor: Keith A. Nelson
Title: Professor of Chemistry

Acknowledgments

I want to thank, first and foremost, my advisor Keith, for arguing with me when I'm wrong, questioning me when I'm right, and even encouraging me when nothing seems to work, but mostly for fostering a group culture which could not be better.

To the Nelson group, present and past, my thanks for being colleagues and friends, especially Kit Werley, Kung-Hsuan Lin, and Qiang Wu for making recent times so great. My thanks also to the older crew, Kathy and Ka-Lo for bringing sunshine into the group, just when it needed a change, Darius for always being a dependable rock, and Taeho for being the most patient man I've ever met. Duffy and Josh', I'll remember quantum mechanics thanks to you two. Christoph, Johanna, and Harold, for being receptive audiences for all the 'back in the old days' stories.

Nikolay, David, and Thomas, thanks for teaching everything I know about optics, and showing me the amazing things you'll see if you just stop and watch, well, as long music isn't playing at least. Josh, Peter, Ben, Rebecca and Jamie, I appreciate the directions you pushed and the examples you set.

To my parents and sister, you've always been there, happy to give advice or just an ear. You've also been very understanding when its late at night, the laser is broken, and the last thing I wanted to do is talk. Thank you.

To my friends, Andy, Charley, Damani, and Youssef- thanks for making away-from-lab actually be different, yet still intellectually stimulating. Also, thanks to the gang back in Pennsylvania, Harry, Greg, Kate and Sara, although we've now scattered to the winds, I'll always know where home is.

Contents

1 Introduction **25**

2 Polariton Theory **29**

2.1 Phonon-Polaritons 29

2.2 Polariton propagation through Maxwell's Equations 32

2.3 Dielectric solutions for Slab Waveguides 36

2.4 Dielectric Solutions for Rectangular Waveguides 39

2.5 Impulsive Stimulated Raman Scattering 40

2.6 Probing though E-O sampling 42

3 Finite Difference Time Domain (FDTD) Simulations **45**

3.1 Discretization of Maxwell's equations 46

3.2 Discretization of the phonon modes 48

3.3 Polariton FDTD Implementation 49

3.4 Higher dimensional simulations 50

  3.4.1 2D simulation spaces 51

  3.4.2 3D simulation spaces 54

3.5 Parallelization of the FDTD algorithm 54

3.6 Numerical Stability 58

3.7 Boundary Conditions 59

  3.7.1 Reflective Boundary Conditions 59

  3.7.2 Periodic Boundary Conditions 61

3.8 Simulated Optical Pumping 63
    3.8.1 Fixed Spot Pumping 65
    3.8.2 Ray Optic pumping 68
    3.8.3 Pumping at an angle 71
    3.8.4 Simulated Beam Pumping 72
3.9 Simulated Polariton Imaging 74
    3.9.1 Talbot Imaging and Interferometry 76
3.10 Simulation of Patterned Materials 77
3.11 Simulation optimizations 77
    3.11.1 Memory use optimizations 78
    3.11.2 Speed optimizations 79

4 Phonon-polaritons in Bulk Materials 81

4.1 Experimental Methods 81
4.2 Polariton Generation Through ISRS 83
    4.2.1 Broadband Generation 83
    4.2.2 Narrowband Generation 86
    4.2.3 Cherenkov Cone 86
4.3 Polariton Detection 88
    4.3.1 Real-space Imaging 88
    4.3.2 Space Time Plots 90
4.4 Bulk Polariton Dispersion 90
4.5 Polaritons in Bulk Crystals 92

5 Confinement in One Dimension 93

5.1 Narrowband excitation of LN slabs 94
    5.1.1 Crystal Ion Slicing Slab Fabrication 94
    5.1.2 Dispersion 95
5.2 Broadband excitation of LN 99
5.3 Selective Driving of Multiple Modes 100

5.4 Detection Efficiencies of Differing Modes 103
5.5 Data Filtering though 2D Fourier Transforms 105
    5.5.1 Bandpass filtering 107
    5.5.2 Intelligent filtering 107
5.6 Slab Waveguides as Detectors 108

6 Confinement in two dimensions **109**
6.1 Femtosecond laser machining 109
6.2 Single square waveguides 111
6.3 Waveguide coupling efficiency 112
    6.3.1 Expected coupling efficiency 114
    6.3.2 Experimental coupling efficiency 115

7 Mode Converting Structures **119**
7.1 Structure Design 119
7.2 Experimental 121
7.3 3D Fourier Analysis 124

8 Photonic Crystals **127**
8.1 Photonic Crystal Fabrication 128
8.2 2D Photonic Slab Experiments 128
    8.2.1 Frequency-Specific Excitation 130
    8.2.2 Wavevector-Selected Excitation 131
    8.2.3 Normal Mode Imaging 134

9 Conclusions **137**

List of Figures

2-1 Doubled unit cell of LN, below the ferroelectric phase transition. The arrows indicate the directions of displacements that have moved ions from their positions in the higher-symmetry paraelectric phase into their positions in the ferroelectric phase. 30

2-2 Theoretical potential surface for the A_1 soft mode of LN. 31

2-3 Dispersion curve for the A_1 soft mode of $LiNbO_3$. 35

2-4 Schematic slab waveguide. With the electric field polarized as indicated (vertically), the solutions of the system correspond to a TM slab waveguide. 36

2-5 Dispersion relation of the lowest 6 TE modes of the lower polariton branch within a 50 μm thick LN slab. Electric fields are polarized along the optic axis. 38

2-6 Rectangular waveguide of transverse dimensions a and b. Modes primarily polarized along b yield approximate TE and TM solutions in the regions indicated. 40

3-1 Simulation grid of a 1D FDTD simulation, with $\vec{x}$ corresponding to the direction of wave propagation, $\vec{z}$ the polarization of the electric field, and $\vec{y}$ the polarization of the magnetic field. The electric field and magnetic fields are simulated on grids offset from each other by a distance $\frac{\Delta x}{2}$. 46

3-2 Simulation grid of a 2D transverse electric (TE) FDTD simulation, with two simulated electric fields polarized transverse to the simulation space and one magnetic field polarized normal to the simulation space. The electric field and magnetic fields are simulated on offset grids. . . 51

3-3 Simulation grid of a 3D FDTD simulation, with 3 simulated electric fields and 3 magnetic fields. The offset grid has electric fields polarized normal to the simulation unit cell faces, centered on the faces, and magnetic field polarized parallel to the cell edges, at the center of the edges. 55

3-4 Simulation grid of a 2D FDTD simulation, parallelized across two nodes, node 0 and node 1. The shaded electric fields are passed from node 1 to node 0, the shaded magnetic from node 0 to node 1 57

3-5 Schematic reflective simulation boundary, with a multi-cycle wave packet both before (a) and after (b) interaction with the simulation boundary.. The area labeled 'Reflective Boundary' is not defined within the simulation space but can be considered a perfect conductor because fields are forced to 0 at the bounds of the space. Impacting radiation switches sign and direction o f propagation, but is otherwise unchanged by the interaction with the bounds of the space. 60

3-6 Schematic periodic simulation boundary, with a multi-cycle wave packet both before (a) and after (b) interaction with the simulation boundary.. The areas labeled 'Periodic Boundary' are not defined within the simulation space, and radiation impacting them continues on the opposite side of the simulation space unimpeded. 62

3-7 Schematic absorptive simulation boundary, with a multi-cycle wave packet both before (a) and after (b) interaction with the simulation boundary. The radiation is mostly absorbed by interaction with the perfectly matched layer (PML) pseudo-absorptive boundary, but a small amount of the original wave packet does reflect. 64

3-8 Optical Path Length (OPL) array for a TM simulation assuming a normal incidence pump. The material file shown in (a), with the pump fields entering the simulation space as shown, yields the OPL array shown in b. The z axis of the OPL array gives the total amount of time a pump wavefront takes to reach that x and y coordinate in the crystal. The pump beam takes longer to propagate through the substrate crystal than it does to propagate through the surrounding air. 66

3-9 Polariton Amplification through multiple excitations, diagramatically depicted in 1D. At t=0, a pump pulse is incident on the crystal, and produces leftward and rightward going polariton waves. At a time Δt later, a second excitation pulse hits the crystal to the right of the original excitation region, thus producing constructive interference between the two rightward going waves, and destructive interference between the leftward going waves. 68

3-10 Space-Time plot of simulated echelon amplification, using Fixed-Spot pumping for generating the field, including 10 excitation events over the time period 0-8 ps, and detected using simulated 800 nm imaging. 69

3-11 Simulated polariton response using a 2D TM simulation of generation due to an angled pump.[9] Transient X-ray diffracaction occurs off of the weaker polariton wavefront which in nearly parallel to the top surface of the crystal. Unlike in standard polariton pump-probe experiments, where the cherenkov cone, and the the polariton angle is given by the ratio of pump and THz indicies of refraction, the glancing incidence pump in this experiment produced a generation spot which skittered along the surface of the crystal at $1.1c_0$, thus producing an 8° 'forward angle'. 73

3-12 Simulated fdtd pump field of a line focus excitation before and after down sampling. The degree of down sampling is excessive, as the pump field is no longer smoothly varying on the order of the simulation spatial step. A smaller dx and dy is needed. 74

3-13 Simulated Probe images from full 3D simulations of 300 GHz radiation propagating within 100 μm thick $LiNbO_3$, both before and after a Talbot imaging filter which de-emphasizes low wave-vectors was applied to the probe data. Overall, fringes have become less sharp due to the applied filter, and a small carrier phase shift of approximately 20° has occured. 76

3-14 Patterned material array for the 2D simulation of a $LiNbO_3$ crystal with a square air hole and square metal region. 77

4-1 Experimental setup for real-space polariton imaging, where an 800 nm pulse is split by a 90:10 beam splitter (BS1) to create the pump and probe pulses, and the probe is variably delayed using a mechanical delay stage, then frequency-doubled by a 100 μm BBO crystal. The beam is then expanded using a concave spherical lens (CC) to the so that when passed through the sample, as shown, at about 10° off normal, it fully illuminates the entire region of interest (E), and then is imaged onto a CCD. The pump geometry shown is for narrowband excitation, using a transmissive binary phase mask (PM) to generate two beams which are crossed at the sample by using a 1:1 cylindrical telescope (CL1, CL2). 82

4-2 Dispersion curve of bulk LN, showing the excitation wavevector of a broadband polariton excitation, and the resultant frequencies. Driving wavevectors from 0.8-1.9 cm^{-1} yields frequencies of 0.5-1 THz in the lower polariton branch, and 7.7-7.9 THz in the upper branch. 84

4-3 Schematic illustration of broadband phonon-polariton wavepacket, generated by a cylindrically focused 'line' of light (a), which propagates laterally on a picosecond time-scale (b). Vertically integrating these 2D images yields the polariton field profile, (c) as a function of the lateral dimension only. 85

4-4 Schematic illustration of a narrowband excitation region, indicating the transverse wavelength λ of the generated 8 cycle pulse (a), and the profile of the binary transmission grating (b) used to generate this pattern, when imaged with a 1:1 cylindrical telescope onto the sample, with all diffractive orders other than ±1 blocked. 86

4-5 Considering the polariton pump as a sequence of point source excitations yields the boat-wake-like Cherenkov cone excitation (a), where the angle is determined by the ratio of polariton phase velocity and pump pulse group velocity inside the LN crystal. Because the phase velocity of THz radiation changes significantly, the cone angle changes significantly for lower branch polaritons in the 0-5 THz regime. 87

4-6 Propagation of a 7-cycle polariton wavepacket over a 45 *ps* period. ISRS of crossed 800 nm pulses, generates two counter-propagating polariton wavepackets, which travel away from the generation region at roughly 50 μm/ps. 88

4-7 Experimental bulk dispersion relation of stoichiometric LN compiled from both broadband (squares) and narrowband (triangles) measurements. The upper branch polaritons are only evident in broadband measurements because they are dominated by the lower branch signal until the lower branch signal has propagated away from them, which by which time they have damped away for narrowband measurements. 91

5-1 Electron micrograph of 10 micron LN slabs produced by Crystal Ion Slicing. 95

5-2 Visible light micrograph of a 10 micron LN slab produced by Crystal Ion Slicing. The large slot is a 6 micron width trench produced in the slab using femtosecond laser machining. 96

5-3 Sample geometry of the 10 μm slab waveguide experiment. The lower set of images are experimental images of the narrowband polariton excitations for three different excitation wave-vectors. The upper set of images are the amplitude of E_z from 2D TM FDTD simulations of the fields in the depth of the slabs, under the same excitation conditions. 97

5-4 Theoretical dispersion curves of 10 μm thick LN slabs, determined using the solutions of a dielectric slab waveguide. The x axis, k_x, corresponds to the imposed grating wavevector of the experiment, which gives the periodicity of the excitation in the direction of propagation. 98

5-5 Experimental Dispersion relation of the CIS fabricated 10 μm LN slabs. The points indicate the experimental values determined to belong to the two lowest waveguide modes, and the lines are the theoretical dispersion relations of those two modes. 99

5-6 Broadband phonon polariton propagation in 50μm and 34 μm thick LN films. The left-hand figures show space-time plots of the propagation. The excitation beam reached the crystals at the zero of the time axes and at a location of about 2 mm on the position axes shown. The multiple modes of the waveguide separate spatially as they propagate, due to differing group velocities. The bandpass filter used to clean the raw data is shown on the 50 μm slab Fourier transform. 101

5-7 Theoretical dispersion curves for 34 μm and 50 μm LN slabs, with the lowest 7 waveguide modes indicated. The low-wavevector bound of each mode is where it intersects the light line of radiation propagating in the cladding (in this case air), and at high wavevectors all modes asymptote to the bulk dispersion relation of LN. 102

5-8 Relative driving strengths of the lowest 3 modes of a slab waveguide as a function of slab thickness, by a 50 fs, 100 μm FWHM pump pulse. Results were generated using 2D TM geometry FDTD simulations. Normalized experimental driving strengths are indicated. 104

5-9 Relative detection strengths of the lowest 3 modes of a slab waveguide as a function of slab thickness, by a 50 fs probe pulse. Results were generated using 2D TM geometry FDTD simulations. 106

6-1 Femtosecond laser machining apparatus. The substrate to be patterned is positioned within the beam focus using a computer-controlled 3D linear stage, and machining is executed by using a computer-controlled shutter to allow the intense pulses to reach the sample only at specified locations. The chopper reduces the laser repetition rate to 500 Hz in order to separate successive pulses by a time period that is longer than the 1 ms response time of the shutter. 110

6-2 Coupled waveguide sample geometry. Two 50 μm x 50 μm x 3 mm LN waveguides were separated by a variable distance d. Narrowband 400 GHz phonon-polaritons were driven in the generation waveguide, and their evolution within both waveguides was observed through real-space imaging. 113

6-3 Optical micrograph of the coupled waveguides within the coupling region. All surface irregularities are substantially sub-wavelength for the 100 μm wavelength polariton excitations observed. 113

6-4 Polariton field inside two coupled 50 μm waveguides, observed 35 ps after excitation through real-space imaging, for two waveguide seperations $d = 20$ microns (a) and $d = 10$ microns (b). Images were filtered using 3D fourier bandpass filtering. 113

6-5 Polariton response in both coupled 50 μm waveguides, 40 ps after excitation, for a separation distance of 20 μm. Roughly 10% of the energy has been transferred into the coupled waveguide, and the two waves are $\pi/2$ out of phase. 115

6-6 Polariton response in both coupled 50 μm waveguides, 40 ps after excitation, for a separation distance of 20 μm. Roughly 50% of the energy has coupled into the coupled waveguide, and the two waves are $\pi/2$ out of phase. 116

6-7 Energy transfer into the coupled waveguide as a function of separation distance, monitored 1 mm from the onset of coupling. 117

7-1 Mode converter structure, as designed (a), fabricated for 100 GHz in 250 μm thick $LiTaO_3$ (b), and fabricated for 300 GHz in 50 μm thick $LiNbO_3$ (c). 120

7-2 Magnitude of the E_z component of the electric field of the TM_{10} and TM_{30} modes respectively of a perfect magnetic conductor (PMC). The transverse wavevector, k_z, is higher for the TM_{30} mode. 121

7-3 Mode converter excitation spectrum, measured throughout the input waveguide, outside of the initial generation region. The 300 GHz center frequency spectrum has significant components from 100-500 GHz. . . 123

7-4 300 GHz phonon-polaritons, inside the input waveguide of the mode converting structure, 2 ps after generation. The six cycle wave packet is almost entirely in the TM_{10} mode of the input waveguide. 123

7-5 3D Fourier transform of the output waveguide signal. The peaks of high k_z correspond to conversion to the TM_{30} mode of the waveguide. 124

7-6 Space-time plot of the lowest order TM_{10} mode in the output waveguide. Generated by back Fourier Transforming the full data set, after filtering out high k_z signal. 125

7-7 Mode converter output spectrum, normalized to the input spectrum shown in Figure 7-3. The TM_{30} mode is selectively outputted at 300 GHz.126

8-1 Schematic dispersion relation of a photonic crystal in a material such as LN with a polariton mode. The imposed photonic bandgap and the intrinsic polariton bandgap interact to produce propagating modes at frequencies which would be forbidden in an upatterned crystal[29]. . . 128

8-2 Photonic crystal sample machined in 50 micron thick LN. Six individual 2D slab photonic crystals were fabricated, with hole diameters ranging from 50 microns down to 4 microns as indicated. All photonic crystals have 20 periods in both the x and z dimensions, with a lattice spacing, a of 100 microns between neighboring holes. 129

8-3 Close-up images of photonic crystals machined in 50 micron thick LN. 129

8-4 Space-time plot showing polariton signals, driven by a 300 GHz center-frequency broadband excitation in the unpatterned LN slab region between two neighboring photonic crystals of hole diameters 50 and 30 microns. The narrowband signals appear due to reflections off of the bandgap structures. 131

8-5 Un-normalized spectra of the two reflected polariton responses in Figure 8-4. The blue line corresponds to radiation rejected by the lower filling fraction 30 micron diameter hole photonic crystal, the green to radiation rejected by the 50 micron diameter hole photonic crystal. . 132

8-6 Square lattice photonic crystal excited by a 200 micron center-wavelength wavepacket, inside of the photonic crystal. The six branches of the photonic crystal dispersion relation are driven, with two distinct photonic bandgaps observable at 280 and 610 GHz. A third bandgap at 1.1 THz is also suggested by the data. 133

8-7 Lowest six photonic crystal modes of an air-hole-in-high dielectric 2D slab photonic crystal[27]. Higher order modes exhibit more nodes in the z direction. In the case of the LN photonic crystal studied, these correspond to all 6 eigenmodes of the lower polariton branch. 134

8-8 Photonic crystal with 15 micron diameter holes, driven with a 200 micron center-wavelength broadband polariton excitation. The resultant three dimensional dataset was Fourier-filtered in all three dimensions, discarding all signal which are unsupported by the photonic crystal. The resultant filtered fields approximately 80 ps post excitation are pictured in (a), and a subset image with an additional tight frequency bandpass filter applied is depicted in (b). The image in (b) is of the first excited mode of the photonic crystal. 135

List of Tables

2.1 Phonon frequencies of the lowest A_1 and E modes of LN and LT. Raman and IR data extracted from data reported by Barker and Louden[3, 2] 30

Chapter 1

Introduction

Electromagnetic radiation in crystalline solids interacts with resonant material excitations to form polariton modes, including exciton-polaritons, phonon-polaritons, and plasmon-polaritons among others. In each case the coupling alters the electromagnetic wave properties (dispersion, reflection at interfaces, and attentuation) in ways that offer unique possibilities (recent examples include the surging interest in plasmonics[4, 11] and in exciton-polariton microcavities[12, 40].

In this thesis a systematic study of phonon-polaritons in patterned ferroelectric crystals is presented. This case is particularly interesting because the strongly polar nature of ferroelectric crystals vibrational modes leads to correspondingly strong coupling between the phonon modes and electromagnetic modes of comparable frequency and wavevector. Due to this extremely strong coupling, phonon-polariton modes in ferroelectric crystals display pronounced effects including extremely large "forbidden" gaps between phonon-polariton branches and strong admixtures of vibrational and electromagnetic amplitudes even at frequencies quite far from the uncoupled phonon resonances, but still arising from an avoided crossing between the phonon and electromagnetic modes. These properties suggest a wide range of applications including an integrated platform for phonon-polariton generation, propagation, interaction with material structures and hybrid material constituents, and detection. The platform can be used for linear or nonlinear THz spectroscopy and signal processing and for generation of THz radiation that may be coupled into free space. In many of these applications, specifically designed and fabricated structures that are integrated into the ferroelectric material may play key roles, and even remove the need to couple the fields out in to free space, allowing generation, interaction and detection to all occur in one device. Demonstration and modeling of phonon-polariton interactions with such structures will be a central theme in the work presented in this thesis.

It has long been observed that the interaction of sub-200 fs pulses with various ferroelectric crystals can be used to generate coherent, broadband[1, 15, 14] or narrowband THz radiation, which can then be detected using either a localized probe beam[33] or through spatially resolved imaging[51]. The nature of coupling to various "polaritonic" elements has been studied[50, 53], and applications of polariton generation and detection to THz coherent control have been treated[17].

The goal of this research was the experimental demonstration and quantitative modeling of phonon-polariton interaction with different levels of material confinement, and through those efforts the creation of a testbed for the use of confined THz fields in spectroscopic applications. In particular, THz phonon-polaritons were created through Impulsive Stimulated Raman Scattering (ISRS) off of Raman and IR active modes of the ferroelectric crystals $LiNbO_3$ and $LiTaO_3$. These generated THz fields were allowed to evolve in time, and probed using a variant of standard femtosecond pump-probe techniques, typically using Real-Space imaging[17, 33], where the fields throughout a large lateral region are probed simultaneously, and spatially resolved onto a camera.

Photonic structures such as waveguides, waveguide couplers, mode converters and photonic crystals have been studied extensively in the visible[44], THz[71, 58, 18], and microwave[56] regimes, but these studies have relied on either comparisons of the input and outputs of the system, or scattering of a small fraction of the interacting radiation scattering off of defects, and coupling into a near or far field detector[6]. Polariton real-space imaging allows the detection of the fields while they are still in the structure of interest, and opens up unique possibilites for characterization of radiation within complex structures.

The generation, propagation and detection of these phonon-polaritons are at their core linear and nonlinear optical processes which can be described with classical wave mechanics. Chapter 2 explains the theory surrounding the driving, propagation and detection of these modes, and sets up a consistent notational system which is used throughout the thesis when considering propagating polariton modes.

The various deficiencies of real-space imaging, especially the two-spatial-dimension nature of its images, and other phase matching considerations necessitated the development of computer simulations which can mimic a full polariton experiment including simulated polariton generation, field propagation, interaction with secondary materials, and imaging. Chapter 3 describes a Finite Difference Time Domain (FDTD) simulation approach which can simulate all of these behaviors in one, two or three spatial dimensions, and which also gives a metric of absolute electric fields and normal-mode displacements everywhere within the simulation. Specific simulation optimizations to allow for the fastest, largest, or most accurate simulation of the propagating fields are considered.

Phonon-polariton interactions with structures of increasing dimensions of confinement and patterning are considered in chapters 4-8. The experimental methods used to generate and detect phonon-polaritons are considered in chapter 4, especially as pertinent to the characterization of bulk (thick, unpatterned) crystals of LN. The use of these same methods to deal with crystals with one dimension of confinement, slab waveguides is described in Chapter 5. Slab waveguides produced both through Crystal Ion Slicing (CIS) and conventional polishing techniques were probed using narrowband and broadband polariton methods, and the advantages of both types of measurement are considered. Adding a second dimension of confinement, as discussed in chapter 6, allows the consideration of the classic coupled waveguide geometry, where relatively narrowband fields are directly observed within the coupling region, and coupling efficiencies were measured. Chapter 7 continues with the addition of patterning in the dimension of propagation. Mode converting structures, designed to convert between different output waveguide modes of the structure in a frequency-dependent manner, were designed, fabricated, and charaterized. Lastly, chapter 8 considers the full patterning in three dimensions of LN into a dielectric-slab photonic bandgap crystal. The responses of these 'polaritonic' bandgap crystals to both wavevector specific and frequency specific excitations were measured and modeled.

Chapter 2

Polariton Theory

2.1 Phonon-Polaritons

Phonon-polaritons are admixtures of electromagnetic and vibrational excitations which exist in polar crystals, and which arise due to strong coupling between optic phonons and propagating electromagnetic fields of comparable frequency and wavevector. These excitations propagate with light-like speeds, typically in the 100 GHz to 10 THz frequency regime. In the case of the crystals typically used in this work, $LiNbO_3$ and $LiTaO_3$ (LN and LT), the frequencies most easily observed are from 0.1-4 THz. Because these modes are part phonon and part electromagnetic field, they exert an observable modulation of the local index of refraction of the medium as they propagate, and thus allow direct observation of light-like propagation transverse to the plane of observation. Additionally, this frequency regime is ideal for easy fabrication of various photonic structures, which because of the relatively long wavelengths of the phonon polaritons with which they interact, can have feature sizes of 10 μm or more.

The unit cell of $LiNbO_3$, as pictured in Figure 2-1, has a ferroelectric displacement along the z axis, corresponding mostly to motion of the Li and Nb ions. The lowest frequency phonon mode along this dimension is an A_1 soft mode, Table 2.1, with the potential calculated energy surface in Figure 2-2[25].

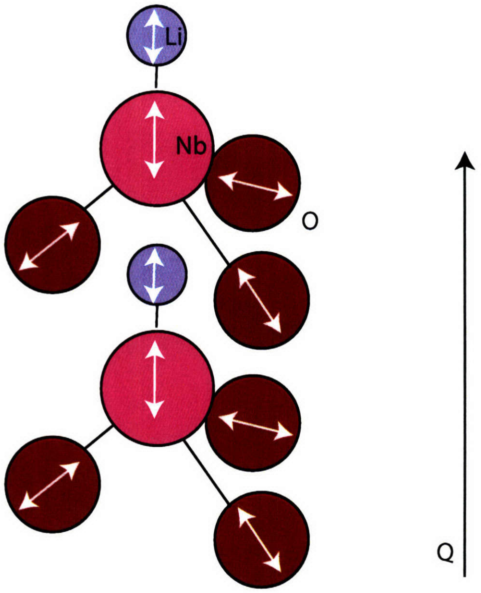

Figure 2-1: Doubled unit cell of LN, below the ferroelectric phase transition. The arrows indicate the directions of displacements that have moved ions from their positions in the higher-symmetry paraelectric phase into their positions in the ferroelectric phase.

Table 2.1: Phonon frequencies of the lowest A_1 and E modes of LN and LT. Raman and IR data extracted from data reported by Barker and Louden[3, 2]

	ν_{TO}(THz)	γ(THz)	ε_0	ε_∞
$LiTaO_3$(A_1 mode)	6.0	0.84	37.6	7.6
$LiTaO_3$(E mode)	4.3	0.42	41.5	17.4
$LiNbO_3$(A_1 mode)	7.6	0.84	26.0	10.0
$LiNbO_3$(E mode)	4.6	0.51	41.5	19.5

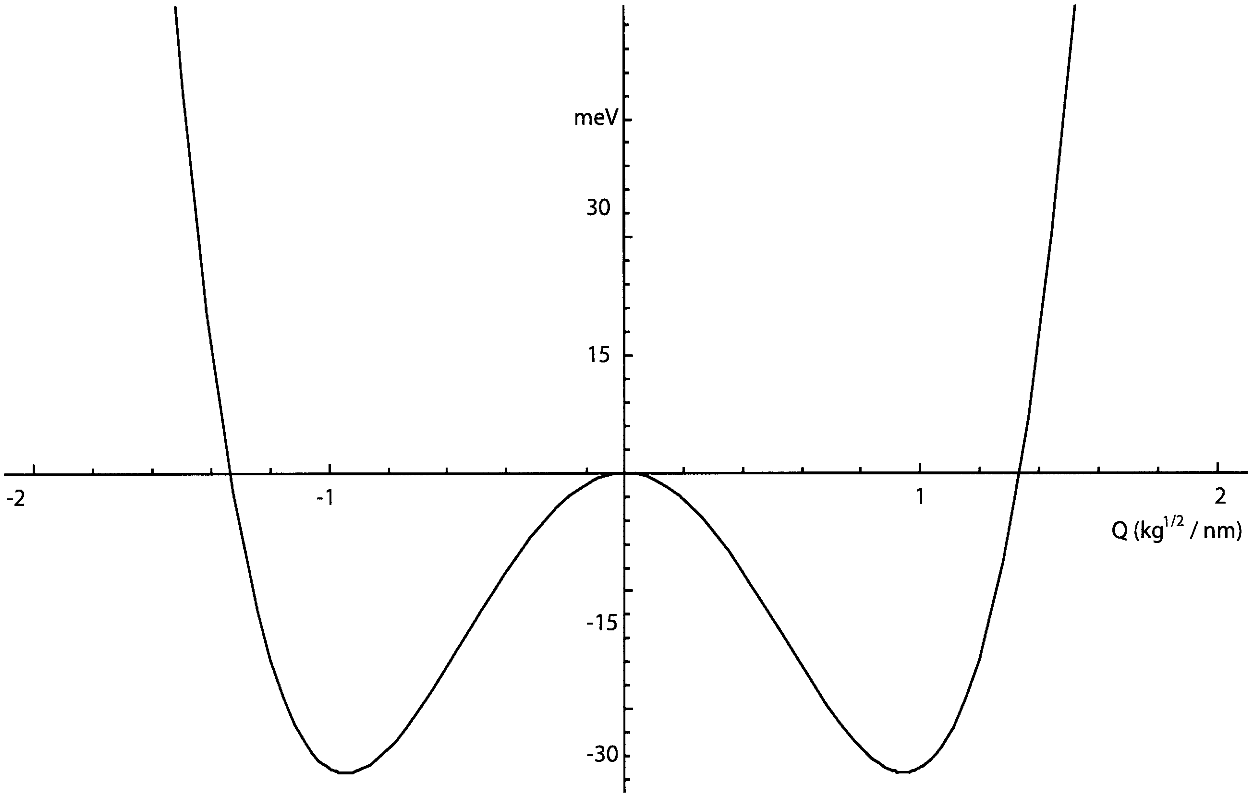

Figure 2-2: Theoretical potential surface for the A_1 soft mode of LN.

In both $LiNbO_3$ and $LiTaO_3$, the 0.1-4 THz phonon-polaritons polarized along the extraordinary axis of the crystal are primarily coupled to the lowest frequency A_1 mode of the crystal, whereas those polarized along the ordinary axes are coupled to the lowest frequency pair of degenerate E modes, corresponding primarily to antisymmetric stretching of the oxygen tetrahedra.

For the purpose of this analysis, only the lowest frequency modes are considered, and they are assumed to be coupled only through the induced electric field.

2.2 Polariton propagation through Maxwell's Equations

The electromagnetic fields, both in the medium of interest and in the surrounding air or vacuum are well described by Maxwell's equations.

$$\nabla \times \vec{E} = -\mu_0 \dot{\vec{H}} \tag{2.1}$$

$$\nabla \times \vec{H} = \dot{\vec{D}} \tag{2.2}$$

$$\vec{D} = \epsilon_0 \vec{E} + \vec{P} \tag{2.3}$$

Here, $\vec{E}$ and $\vec{H}$ are the electric and magnetic fields, μ_0 and ϵ_0 are the vacuum permeability and permittivity, $\vec{D}$ is the displacement field, and $\vec{P}$ is the polarization, each component given by,

$$\begin{pmatrix} \ddot{Q} + \Gamma \dot{Q} \\ P \end{pmatrix} = \begin{pmatrix} b_{11} & b_{12} \\ b_{21} & b_{22} \end{pmatrix} \begin{pmatrix} Q \\ E \end{pmatrix}, \tag{2.4}$$

where Q is the normal mode displacement of a transverse optic phonon as described below in Equation 2.6, and E is a component of $\vec{E}$ parallel to that normal mode[65, 66].

In the case of a uniaxial crystal, such as $LiNbO_3$ or $LiTaO_3$, we can express $\vec{Q}$ as a 3-vector with components along the Cartesian axes. We will use Q_z to designate the displacements along the extraordinary axis of the system, and Q_x and Q_y to designate displacements along the ordinary axes.

For a simple multi-particle system like a single molecule with different atomic masses, the normal mode coordinate $\vec{Q}$ would be defined as,

$$\vec{Q} = \frac{\sum m_p \vec{r}_p}{\mu}, \tag{2.5}$$

where m_p corresponds to the mass of the p^{th} particle, r_p is its displacement from equilibrium, and μ is the reduced mass of the system. For the purpose of long wavelength THz interactions, where we are concerned with not single oscillators, but a large ensemble in, for example, a 1 μm^3 volume, as determined by the propagation length of THz radiation, we use the mass- and volume-normalized coordinate $\vec{Q}$ of a given normal mode i,

$$\begin{aligned} \vec{Q^i} &= \sqrt{NM}\vec{\mathrm{w}^i}, && (2.6) \\ \vec{\mathrm{w}^i} &= \sqrt{\frac{\sum m_p|\vec{r_p^i}|^2}{M}}, && (2.7) \end{aligned}$$

where r_p^i is the displacement of the p^{th} particle from equilibrium due to motion along that particular normal mode, M is the unit cell reduced mass, and N the oscillator density.

The oscillator density N comes from the assumption of one oscillator in each 10-atom unit cell volume; for LiNbO3, with hexagonal lattice coordinates a and c in a rhombohedral setting,

$$N = \frac{4}{\sqrt{3}}\frac{1}{a^2c}. \tag{2.8}$$

From Equation 2.4 comes the equation of motion for a given normal mode of the system, with the three components of $\vec{Q}$ (Q_x, Q_y, and Q_z) directly coupled to the three components of $\vec{E}$.

$$\ddot{Q} + \Gamma\dot{Q} - b_{11}Q = b_{21}E. \tag{2.9}$$

This formula is merely the equation for a forced, damped, harmonic oscillator with $b_{12}E$ as the driving term, Γ as the damping constant, and $b_{11} = \omega^2$ as the natural frequency of the oscillator.

The constitutive relation for electric polarization is,

$$\begin{aligned} P(\omega) &= \epsilon_0\chi(\omega)E(\omega) \\ &= \epsilon_0(\varepsilon_r(\omega) - 1)E(\omega) && (2.10) \end{aligned}$$

where ϵ_0 is the permittivity of free space, $\chi(\omega)$ is the dielectric susceptibility, and $\varepsilon_r(\omega)$ is the relative electric permittivity.

Assuming sinusoidally oscillating solutions in the time domain, Equation 2.9 becomes

$$Q(\omega) = \frac{b_{12}E(\omega)}{\omega_{\mathrm{TO}}^2 - \omega^2 - i\omega\Gamma}. \tag{2.11}$$

Combining this with Equation 2.4, solving for $E(\omega)$, and substituting into Equation 2.10 yields an equation for the relative permittivity,

$$\varepsilon_r(\omega) = 1 + \frac{b_{22}}{\epsilon_0} + \frac{1}{\epsilon_0}\frac{b_{12}b_{21}}{\omega_{\mathrm{TO}}^2 - \omega^2 - i\omega\Gamma} \tag{2.12}$$

The nature of a resonant response is that it should have little effect at frequencies far off of resonance. To this end, consider the limiting cases of $\omega \rightarrow 0$ and $\omega \rightarrow \infty$, and defining ε_0 and ε_∞ to be the values at those limits,

$$\varepsilon_\infty \equiv \lim_{\omega\rightarrow\infty} \varepsilon_r(\omega) = 1 + \frac{b_{22}}{\epsilon_0} \tag{2.13}$$

$$\varepsilon_0 \equiv \lim_{\omega\rightarrow 0} \varepsilon_r(\omega) = 1 + \frac{1}{\epsilon_0}\left(b_{22} + \frac{b_{12}b_{21}}{\omega_{\mathrm{TO}}^2}\right) = \varepsilon_\infty + \frac{b_{12}b_{21}}{\omega_{\mathrm{TO}}^2} \tag{2.14}$$

As ε_0 and ε_∞ have distinct physical meanings, namely the low and high frequency dielectric constants of the system, we will rewrite the coefficients in terms of physically measurable properties.

$$b_{11} = \omega_{\mathrm{TO}}^2 \tag{2.15}$$

$$b_{12} = b_{21} = \omega_{\mathrm{TO}}\sqrt{\epsilon_0(\varepsilon_0 - \varepsilon_\infty)} \tag{2.16}$$

$$b_{22} = \epsilon_0(\varepsilon_\infty - 1) \tag{2.17}$$

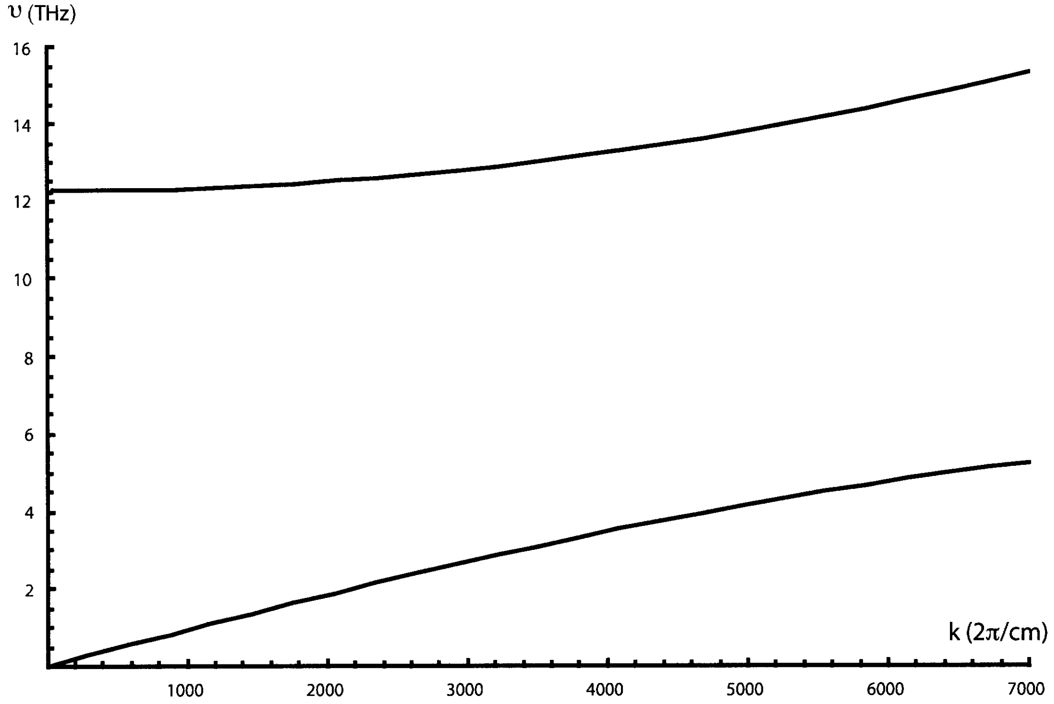

Figure 2-3: Dispersion curve for the A_1 soft mode of $LiNbO_3$.

This allows the rewriting of Equation 2.12, and by using the relationship $\varepsilon_r(\omega) = n^2(\omega) = c^2k^2/\omega^2$, where n is the refractive index, allows solving of the dispersion relationship, $\omega(k)$.

$$\varepsilon_r(\omega) = \varepsilon_\infty + \frac{\omega_{\mathrm{TO}}^2(\varepsilon_0 - \varepsilon_\infty)}{\omega_{\mathrm{TO}}^2 - \omega^2 - i\omega\Gamma} \tag{2.18}$$

$$\omega_\mp(k) = \sqrt{\frac{\omega_{\mathrm{TO}}^2\varepsilon_0 + c^2k^2}{2\varepsilon_\infty} \pm \frac{1}{2}\sqrt{\left(\frac{\omega_{\mathrm{TO}}^2\varepsilon_0 + c^2k^2}{\varepsilon_\infty}\right)^2 - \frac{4\omega_{\mathrm{TO}}^2\varepsilon_0c^2k^2}{\varepsilon_\infty}}} \tag{2.19}$$

Here, the two roots of Equation 2.19 correspond to the lower and upper branches of the polariton dispersion curve, shown in Figure 2-3. Due to the avoided crossing between the phonon and light lines, there is a significant polariton bandgap, i.e. a lack of any propagating waves, between $\omega = \omega_{\mathrm{TO}}$ and $\omega = \omega_{\mathrm{TO}}\sqrt{\frac{\varepsilon_0}{\varepsilon_\infty}} = \omega_{\mathrm{LO}}$, the longitudinal optic phonon frequency.

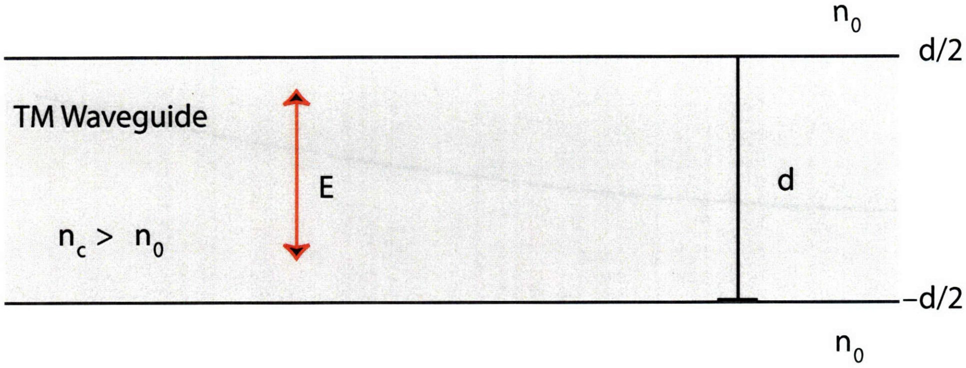

Figure 2-4: Schematic slab waveguide. With the electric field polarized as indicated (vertically), the solutions of the system correspond to a TM slab waveguide.

2.3 Dielectric solutions for Slab Waveguides

Although it is often convenient to describe high-dielectric-contrast waveguides as perfect magnetic conductor (PMC) waveguides, and thus have the solutions exactly correspond to those of the analogous system- a perfect electric conductor (PEC) waveguide, for the dielectric contrasts afforded by typical ferroelectric crystals this is a poor approximation, especially in the thin crystal limit.

Perfect conductor waveguides are characterized by a zero of tangential field at the boundaries of the waveguide, since tangential fields cannot exist in the perfect cladding. In the case of a dielectric waveguide this is not the case, and the more general requirement of tangential field continuity across the boundary must be satisfied.

The generic solution of a TE slab waveguide is

$$\left(\frac{\partial^2}{\partial x^2} - k_y^2 + \omega^2 \epsilon_0 \mu_0 \varepsilon_r\right) E_z(x) = 0. \tag{2.20}$$

The derivation for TE slab waveguide modes follows, for the system depicted in Figure 2-4, a core of high dielectric material for $|y| < d/2$, surrounded by a lower dielectric material of infinite thickness.

Inside the core, the modes are periodic in y, and they decay monotonically in the cladding.

$$\left.\begin{aligned} E_z &= E_0 \cos{(k_y y)} e^{i(-kx+\omega t)} \hat{k} \\ H_x &= -E_0 \sqrt{\tfrac{\epsilon_0 \varepsilon_r}{\mu_0}} \sin{(k_y y)} e^{i(-k_x x+\omega t)} \hat{k} \\ H_y &= -E_0 \sqrt{\tfrac{\epsilon_0 \varepsilon_r}{\mu_0}} \cos{(k_y y)} e^{i(-k_x x+\omega t)} \hat{k} \end{aligned}\right\} |y| \leq \frac{d}{2} \tag{2.21}$$

$$\left.\begin{aligned} E_z &= E_0 e^{\pm k_y' y} e^{i(-k_x x+\omega t)} \hat{k} \\ H_x &= -E_0 \sqrt{\tfrac{\epsilon_0 \varepsilon_r}{\mu_0}} e^{\pm k_y' y} e^{i(-k_x x+\omega t)} \hat{k} \\ H_y &= -E_0 \sqrt{\tfrac{\epsilon_0 \varepsilon_r}{\mu_0}} e^{\pm k_y' y} e^{i(-k_x x+\omega t)} \hat{k} \end{aligned}\right\} |\mp y| \geq \frac{d}{2} \tag{2.22}$$

In these expressions k_y and k_y' are the y components of the wavevector in the core and cladding respectively. k_x is the wavevector component in the direction of propagation, and must be the same in both regions for the system of equations to be true for all times t and positions x.

Ignoring time dependence, and requiring continuity and differentiability of E_z across the boundary, yields

$$\tan{(k_y \frac{d}{2})} = \frac{k_y'}{k_y}. \tag{2.23}$$

$$\cot{(k_y \frac{d}{2})} = -\frac{k_y'}{k_y}. \tag{2.24}$$

corresponding to even and odd symmetry modes of the system respectively.

Defining different x and y components inside and outside the core determines the allowable values of k_y for a given k_x and ω, and the indicies of refraction in the two regions determine $|\vec{k}|$.

$$k_x^2 - (k_y')^2 = \omega^2 \epsilon_0 \mu_0 \tag{2.25}$$

$$k_x^2 - k_y^2 = -\omega^2 \epsilon_0 \mu_0 \varepsilon_r \tag{2.26}$$

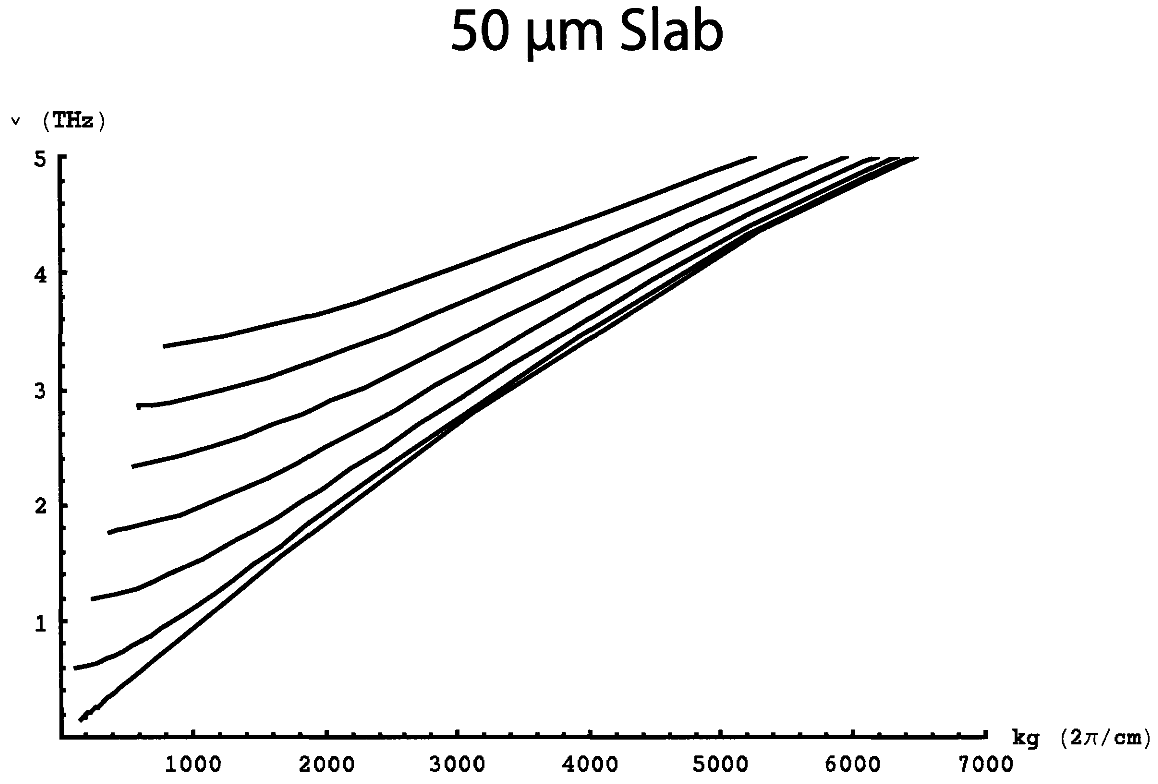

Figure 2-5: Dispersion relation of the lowest 6 TE modes of the lower polariton branch within a 50 *μm* thick LN slab. Electric fields are polarized along the optic axis.

Combining to remove the k_x dependence,

$$\frac{k_y'}{k_y} = \sqrt{\frac{\omega^2 \epsilon_0 \mu_0 (\varepsilon_r - 1)}{k_y^2} - 1}. \tag{2.27}$$

Solving the trancendental system of equations defined by equations 2.23 and 2.27 yields the dispersion relation of all the modes of a given slab waveguide. Calculated dispersion curves of a 50 *μm* thick LiNbO$_3$ slab are shown in Figure 2-5. One important consequence of this system of equations is that a dielectric slab waveguide has no cutoff frequency; for a given frequency, there is at least one supported waveguide mode for any thickness slab waveguide.

For the case of a TM slab waveguide mode, equations 2.23 and 2.24 becomes,

$$\tan(k_y \frac{d}{2}) = \frac{k_y'}{\varepsilon_r k_y}. \tag{2.28}$$

$$\cot(k_y \frac{d}{2}) = -\frac{k_y'}{\varepsilon_r k_y}. \tag{2.29}$$

2.4 Dielectric Solutions for Rectangular Waveguides

Full arbitrary solutions for a dielectric waveguide with confinement in both transverse directions are not obtainable analytically, but a reasonable approximation can be obtained by treating the system as separable in the transverse dimensions. For the system,

$$\nabla^2\psi + \omega^2\epsilon_0\mu_0\varepsilon_r(y,z)\psi = 0, \tag{2.30}$$

which is separable in the limit of

$$\varepsilon_r(y,z) = \varepsilon_{ry}(y) + \varepsilon_{rz}(z) \tag{2.31}$$

A reasonable facsimile of a rectangular waveguide of dimensions a and b as shown in Figure 2-6 gives correct values of ε_r everywhere except the corner regions, which is the limitation of the analytically solvable system.

$$\varepsilon_{ry}(y) = \begin{cases} \varepsilon_0/2, |y| < a/2 \\ \varepsilon_r - \varepsilon_0/2, |y| \geq a/2 \end{cases} \tag{2.32}$$

$$\varepsilon_{rz}(z) = \begin{cases} \varepsilon_0/2, |z| < a/2 \\ \varepsilon_r - \varepsilon_0/2, |z| \geq a/2 \end{cases} \tag{2.33}$$

This allows the results to be rewritten as the product of TE and TM slab waveg-

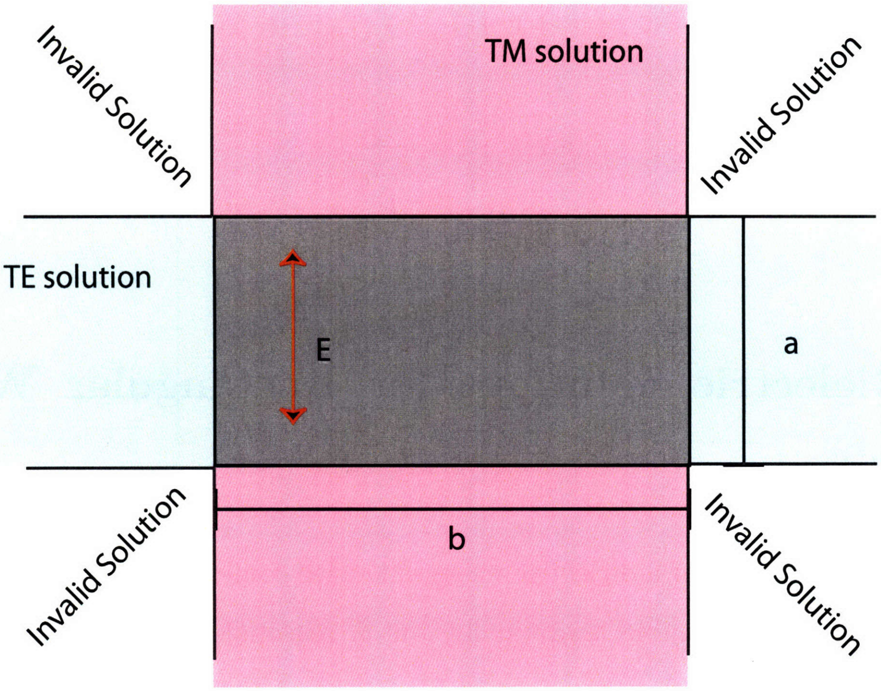
TM solution
Invalid Solution
Invalid Solution
TE solution
E
a
b
Invalid Solution
Invalid Solution

Figure 2-6: Rectangular waveguide of transverse dimensions a and b. Modes primarily polarized along b yield approximate TE and TM solutions in the regions indicated.

uide modes, with solutions given in the previous section. For the lowest order TEM$_{00}$ mode of a waveguide of dielectric constant ε_4 in air, the solution is,

$$\begin{aligned}
\tan(k_z \frac{b}{2}) &= \frac{k'_z}{\varepsilon_r k_z} && (2.34) \\
k'_z &= \sqrt{\omega^2 \epsilon_0 \mu_0 (\varepsilon_r - 1) - k_z^2} && (2.35) \\
\tan(k_y \frac{a}{2}) &= \frac{k'_y}{k_y} && (2.36) \\
k'_y &= \sqrt{\omega^2 \epsilon_0 \mu_0 (\varepsilon_r - 1) - k_y^2} && (2.37)
\end{aligned}$$

2.5 Impulsive Stimulated Raman Scattering

For all of the experiments in this thesis, THz radiation, generated via phonon-polaritons, is initially driven though Impulsive Stimulated Raman Scattering (ISRS) of a short (60 fs) 800 nm pulse in a ferroelectric crystal. During ISRS driving, the ions of the unit cell are unable to respond to the high carrier frequency of the 800 nm optical pump, but the electrons are driven directly. Through their nonlinear coupling to the lattice, the lattice vibrational modes of the unit cell are driven impulsively and may begin to oscillate at their resonance (THz) frequencies. The driving force arises through impulsive stimulated Raman scattering (ISRS) involving mixing among the frequency components of the optical pulse.

Consider the electrostatic energy density stored within the oscillators of the unit cell,

$$W = \frac{1}{2}\vec{D} * \vec{E} = \frac{1}{2}\epsilon(Q)\vec{E} * \vec{E} \tag{2.38}$$

$$\epsilon(Q) = \sqrt{\frac{1}{NM}}(1 + N\alpha(Q)), \tag{2.39}$$

where $\alpha(Q)$ is the polarizability of the mode. Expanding the equation to first order,

$$\epsilon(Q) = \sqrt{\frac{1}{NM}}\left[1 + N\alpha_0 + N\left(\frac{\partial\alpha}{\partial Q}\right)_0 Q\right], \tag{2.40}$$

Taking the gradient of the electrostatic energy density with respect to the normal mode displacement yields,

$$F = \frac{\partial W}{\partial Q} = \frac{1}{2}\sqrt{\frac{N}{M}}\left(\frac{\partial\alpha}{\partial Q}\right)_0 |E_{\mathrm{pump}}|^2 \tag{2.41}$$

This yields a final equation for the time-dependent ISRS driving force,

$$F_{\mathrm{ISRS}}(t) = \frac{1}{2}\epsilon_0\sqrt{\frac{N}{M}}\left(\frac{\partial\alpha}{\partial\vec{\mathrm{w}}}\right) \mathrm{I}_{\mathrm{pump}}(t), \tag{2.42}$$

where $\mathrm{I}_{\mathrm{pump}}(t)$ refers to the instantaneous intensity of the pump field at time t.

2.6 Probing though E-O sampling

A variety of polariton detection methods were used, but they all at the core are derived from localized index of refraction modulation within the ferroelectric crystal, induced by the presence of the THz phonon-polaritons.

To first order, the modulations of the index of refraction are very minute, even for comparatively large THz field strengths, and thus the time-dependent optical index of refraction for a probe beam of polarization i can be written perturbatively in terms of the nonlinear optical coefficients r_{ij},

$$\Delta\left(\frac{1}{n^2}\right)_i = \sum_{j=1}^{3} r_{ij}E_j \tag{2.43}$$

which for the simple case of probe beam and polariton polarizations entirely along the extrodinary axis z reduces to

$$\Delta\left(\frac{1}{n^2}\right)_z = r_{33}E_z^{\mathrm{THz}} \tag{2.44}$$

where r is given by the electro-optic tensor. For 3m crystal such as LN and LT, r takes the form

$$r = \begin{pmatrix} 0 & -r_{22} & r_{13} \\ 0 & r_{22} & r_{13} \\ 0 & 0 & r_{33} \\ 0 & r_{51} & 0 \\ r_{51} & 0 & 0 \\ -r_{22} & 0 & 0 \end{pmatrix} \tag{2.45}$$

In the limit of small THz fields, such that $r_{33}E_z << \frac{1}{n_e^2}$, the total refractive index can be approximated as

$$n_e' = n_e - \frac{n_e^3}{2}r_{33}E_z \tag{2.46}$$

A plane wave of wavelength λ traveling through a thickness d of material with index n_e' would have a net phase shift relative to a plane wave traveling through material of index n_e of

$$\phi_z = -\frac{d}{\lambda}\frac{n_e^3}{2}r_{33}E_z. \tag{2.47}$$

Chapter 3

Finite Difference Time Domain (FDTD) Simulations

This work partially produced in collaboration with Nikolay S. Stoyanov and David W. Ward of the Massachusetts Institute of Technology.

The nature of polariton generation, detection, and interaction with materials exhibiting confinement in all three dimensions is that it is inherently difficult to determine a priori what the signal should look like. Couple this difficulty to small signals and a noisy detection methodology, and it becomes very difficult to determine if what you're seeing is noise or signal.

Thankfully, the propagation of polaritons can be expressed simply through Maxwells equations, and their coupling to the system as the interaction with localized dipoles modeled as forced, damped (an)harmonic oscillators. To model EM field propagation, we use a Finite Difference Time Domain (FDTD) method, which determines the change in the electric field, $\vec{E}$, at a point based on the gradient of the magnetic field, $\vec{H}$ at that point, and conversely for the change of $\vec{H}$.

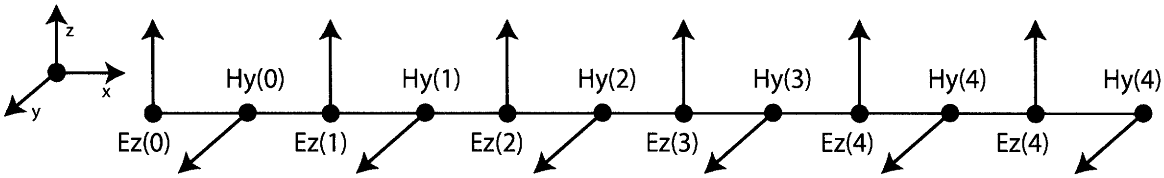

Figure 3-1: Simulation grid of a 1D FDTD simulation, with $\vec{x}$ corresponding to the direction of wave propagation, $\vec{z}$ the polarization of the electric field, and $\vec{y}$ the polarization of the magnetic field. The electric field and magnetic fields are simulated on grids offset from each other by a distance $\frac{\Delta x}{2}$.

3.1 Discretization of Maxwell's equations

Although the simulations described throughout this thesis are more typically performed in two or three dimensions, it is easiest to describe the methodology of producing a system of discrete equations from Maxwell's equations in the case of a 1D simulation.

For this purpose, consider a simulation as shown in Figure (3-1), with two field components, E_z and H_y, and all propagation in the $\hat{x}$ direction. In this case, Maxwell's equations reduce to

$$\frac{\partial E_z}{\partial x} = -\mu_0 \frac{\partial H_y}{\partial t} \tag{3.1}$$

$$\frac{\partial H_y}{\partial x} = \frac{\partial D_z}{\partial t} \tag{3.2}$$

$$D_z = \epsilon_0 E_z + P_z, \tag{3.3}$$

For the purpose of numerically calculating changes in E_z and H_y, an offset grid as shown is preferred.[67] This geometry both allows us to approximate the spatial derivatives of E_z and H_y as merely the difference between neighboring values of E_z and H_y, and guarantees that the field divergence remains zero. Letting x designate the grid points corresponding to E_z, and dx the distance between two grid points

$$\begin{aligned} \left.\frac{\partial H_y}{\partial t}\right|_{x=1.5} &= -\frac{1}{\mu_0}\left.\frac{\partial E_z}{\partial x}\right|_{x=1.5} \\ &= -\frac{1}{\mu_0}\frac{E_z|_{x=2} - E_z|_{x=1}}{dx} \end{aligned} \tag{3.4}$$

$$\begin{aligned} \left.\frac{\partial D_z}{\partial t}\right|_{x=2} &= \left.\frac{\partial H_y}{\partial x}\right|_{x=2} \\ &= \frac{H_y|_{x=2.5} - H_y|_{x=1.5}}{dx}. \end{aligned} \tag{3.5}$$

For the moment, assuming a linear dielectric, $D_z = \epsilon E_z$, and assuming nomalized coordinates ($dx = 1$), yields the final equations

$$\left.\frac{\partial H_y}{\partial t}\right|_{x=(i+\frac{1}{2})} = -\frac{1}{\mu_0}(E_z|_{x=(i+1)} - E_z|_{x=i}) \tag{3.6}$$

$$\left.\frac{\partial E_z}{\partial t}\right|_{x=i} = \frac{1}{\epsilon}(H_y|_{x=(i+\frac{1}{2})} - H_y|_{x=(i-\frac{1}{2})}), \tag{3.7}$$

which is to say, we can calculate the change in H given two neighboring values of E, and vice-versa[69, 68]. One additional consequence of using a Yee cell is that the fields must be interleaved in time in addition to spatially. Thus, the magnetic field is always calculated at a time $\frac{dt}{2}$ after its corresponding electric field, and vice versa. Letting the current time of the electric field be τ, the timestep duration Δt, and dropping the "$x =$" and "$t =$" for clairity, yields

$$\begin{aligned} \left.\frac{dH_y}{dt}\right|_{(i+\frac{1}{2}),(\tau+\frac{\Delta t}{2})} &= -\frac{1}{\mu_0}(E_z|_{(i+1),\tau} - E_z|_{i,\tau}) \\ H_y|_{\tau+\frac{\Delta t}{2}} &= H_y|_{\tau-\frac{\Delta t}{2}} + \Delta t \left.\frac{dH_y}{dt}\right|_{\tau+\frac{\Delta t}{2}} \\ \left.\frac{dE_z}{dt}\right|_{i,\tau} &= \frac{1}{\epsilon}(H_y|_{(i+\frac{1}{2}),(\tau-\frac{\Delta t}{2})} - H_y|_{(i-\frac{1}{2}),(\tau-\frac{\Delta t}{2})}) \end{aligned} \tag{3.8}$$

$$E_z|_\tau = E_z|_\tau + \Delta t \left.\frac{dE_z}{dt}\right|_\tau . \tag{3.9}$$

3.2 Discretization of the phonon modes

Although in the previous section we ended up treating the material as a linear dielectric, all of the interesting polariton responses such as the avoided crossing previously discussed come about through the time dependent polarization imparted by the oscillating phonon mode. To take this into account, we need to both discretize the harmonic oscillator representation of Q in a way compatible with the forward-in-time propagation of Maxwell's equations, and then work the resulting polarization into the equations for the electric field[35, 36, 70].

In our simple, one dimensional case, there is only one phonon mode, Q_z. Discretization of Equation 2.9,

$$\begin{aligned}
\left.\frac{dQ}{dt}\right|_{(\tau-\Delta t)} &= \frac{Q|_\tau - Q|_{(\tau-\Delta t)}}{\Delta t} \\
&= \dot{Q}|_{(\tau-\Delta t)} && (3.10) \\
\frac{\dot{Q}|_\tau - \dot{Q}|_{(\tau-\Delta t)}}{\Delta t} &= -\Gamma \dot{Q}|_{\tau-\Delta t} + b_{11} Q|_{\tau-\Delta t} - F_{\text{Driving}}|_{\tau-\Delta t} && (3.11) \\
F_{\text{Driving}} &= F_{\text{ISRS}} - b_{12} E && (3.12)
\end{aligned}$$

Resolving these equations, so that no current or future values of Q or $\dot{Q}$ are required to calculate the current values, yields

$$\begin{aligned}
Q|_\tau &= Q|_{(\tau-\Delta t)} + \Delta t \dot{Q}|_{(\tau-\Delta t)} && (3.13) \\
\dot{Q}|_\tau &= (1 - \Delta t \Gamma)\dot{Q}|_{(\tau-\Delta t)} + \Delta t (b_{11} Q|_{(\tau-\Delta t)} - F_{\text{Driving}}|_{(\tau-\Delta t)} && (3.14)
\end{aligned}$$

Including the effects of Q into Equation 3.9, completes the coupling.

$$E_z|_{\tau} = E_z|_{\tau} + \Delta t(\frac{H_y|_{(i+\frac{1}{2}),(\tau-\frac{\Delta t}{2})} - H_y|_{(i-\frac{1}{2}),(\tau-\frac{\Delta t}{2})}}{\epsilon_0} - \frac{b_{21}}{\epsilon_0 + b_{22}}\dot{Q}|_{\tau}). \tag{3.15}$$

3.3 Polariton FDTD Implementation

The method described requires four distinct fields in the one-dimensional case; for each x coordinate simulated, a floating point value for E_z, Q_z, $\dot{Q}_z$, and H_y must be stored. Although, for this simple case, it is not necessary, ideally, the calculation of all four of these values would minimal temporary variables. Minimizing unessecary reads and writes to memory becomes very important in higher dimension simulations. Rewriting the descritized equations for Q, $dotQ$, and E, to remove the out of sequence dependancy, relieves the need for temporary variables as long as the operations are performed in order. In array notation, where i, j and k correspond to array indices (or grid points) in the $\hat{x}$, $\hat{y}$, and $\hat{z}$ directions respectively, and dx is the grid spacing in the $\hat{x}$ direction.

for each i

$$\begin{aligned} Q[i] &= Q[i] + \Delta t\dot{Q}[i] \\ \dot{Q}[i] &= (1 - \Delta t\Gamma)\dot{Q}[i] + \Delta t(b_{11}Q[i] + b_{12}E[i] - F_{\mathrm{ISRS}}) \\ E[i] &= E[i] + \frac{\Delta t}{\epsilon_0 dx}\Big(H[i-1] - H[i]\Big) - \frac{b_{21}\Delta t}{\epsilon_0 + b_{22}}\dot{Q}[i] \end{aligned} \tag{3.16}$$

$$t = t + \frac{\Delta t}{2}$$

for each i

$$H[i] = H[i] + \frac{\Delta t}{\mu_0 dx}\Big(E[i] - E[i+1]\Big) \tag{3.17}$$

$$t = t + \frac{\Delta t}{2}$$

The algorithm in Equations 3.16 and 3.17 is iterated for all space, for the desired number of time steps. Careful selection of the bounds of the array index i is required for both loops; although both arrays have the elements $i = 0 ... (i_{\text{MAX}} - 1)$, Equation 3.16 has the range $i = 1 ... (i_{\text{MAX}} - 1)$, and Equation 3.17 the range $i = 0 ... (i_{\text{MAX}} - 2)$. In effect, E fields are never calculated for $i = 0$, and H fields for $i = i_{\text{MAX}}$, but the (permanently 0) values are in turn used to calculate the other field. Conversely, the calculated E field at $i = (i_{\text{MAX}} - 1)$ and H field at $i = 0$ are never used to calculate anything other than their own value at the next time step. The different limits over which the two systems are iterated has important consequences with respect both boundary conditions, and parallelizing the simulation.

Iteration of the full system of equations results in an implicit time propagation; although time is not made explicit in the equations for the fields and only appears in the algorithm above for bookkeeping purposes, time does advance by a full increment by a full Δt for each iteration. The actual time does remain important for calculation of pump and probe fields, so in practice incrementing the absolute time by $\frac{\Delta t}{2}$ twice is a computationally cheap method of bookkeeping.

3.4 Higher dimensional simulations

In going from a single spatial dimension to a higher number of spatial dimensions, the an increased number of the terms of the curl of $\vec{E}$ and $\vec{H}$ from Maxwells equations (Equations 2.1 and 2.2) become non-zero and important. For every additional electric field component considered, a single additional Q component and single additional $\dot{Q}$ component, both parallel to and at the same grid loci as the E component must be considered.

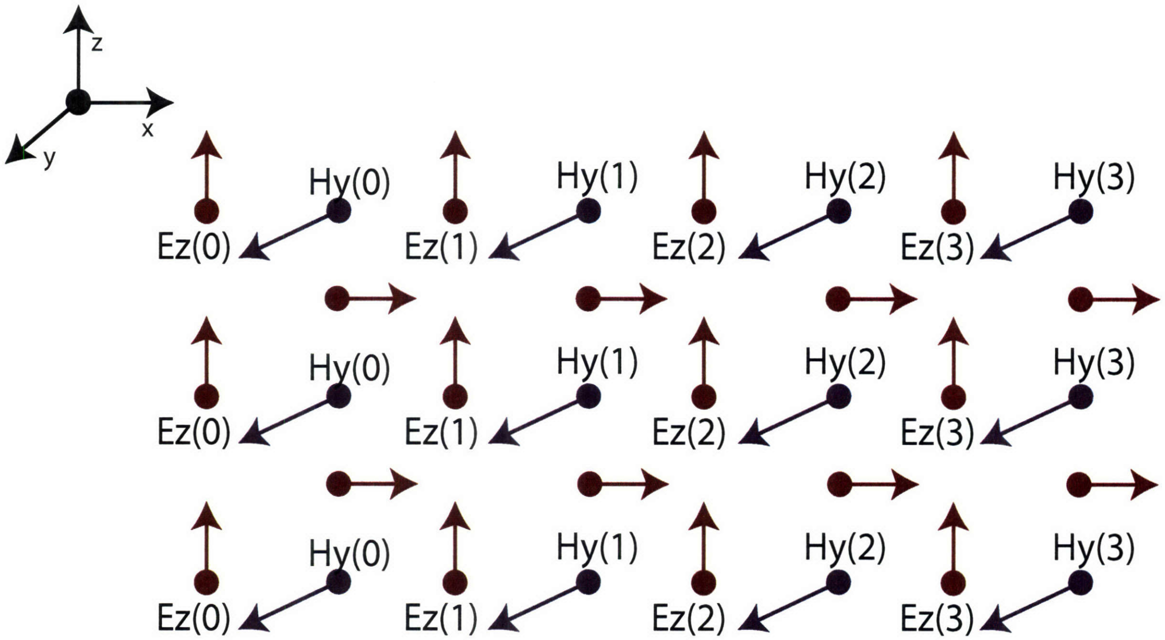

Figure 3-2: Simulation grid of a 2D transverse electric (TE) FDTD simulation, with two simulated electric fields polarized transverse to the simulation space and one magnetic field polarized normal to the simulation space. The electric field and magnetic fields are simulated on offset grids.

3.4.1 2D simulation spaces

The consideration of a 2D space requires the consideration of 3 total field components, a single field component normal to the simulation plane (either E_{normal} or H_{normal}), and two orthogonal field components transverse to the simulation plane, of the opposite kind as the normal field.

The two simulation geometries are labeled by the type of field transverse to the simulation plane. A simulation containing two transverse electric field component and one normal magnetic field component (e.g. E_x, E_z and H_y) would be a Transverse Electric (TE) simulation, and the converse would be a Transverse Magnetic (TM) simulation. This terminology is consistent with that used to describe the polarizations of planar waveguide modes.

As pictured in Figure 3-2, the intracacies of the Yee cell become more apparent in two dimensions. The system is designed so that the spatial derivatives involved in calculating the curls of the fields can be numerically calculated using only two values of the argument field.

In a two dimensional TE simulation, the curl equations (in one dimension, equations 3.1 and 3.2) reduce to,

$$\frac{\partial E_z}{\partial x} - \frac{\partial E_x}{\partial z} = -\mu_0 \frac{\partial H_y}{\partial t} \tag{3.18}$$

$$\frac{\partial H_y}{\partial x} = \frac{\partial D_z}{\partial t} \tag{3.19}$$

$$-\frac{\partial H_y}{\partial z} = \frac{\partial D_x}{\partial t} \tag{3.20}$$

which, as shown in Figure 3-2, means that a given component of H_y should line up with its corresponding component of E_z in z, and with its corresponding value of E_x in x, thus allowing the partials to be rewritten, with i and k being grid locations in x and z respectively,

$$\begin{aligned}\frac{\partial E_z}{\partial x} &= \left.\frac{dE_z}{dx}\right|_{z=const} \\ &= \frac{1}{\Delta x}(E_z[i+1,k] - E_z[i,k])\end{aligned} \tag{3.21}$$

$$\begin{aligned}\frac{\partial E_x}{\partial z} &= \left.\frac{dE_x}{dz}\right|_{x=const} \\ &= \frac{1}{\Delta z}(E_x[i,k+1] - E_x[i,k])\end{aligned} \tag{3.22}$$

$$\begin{aligned}\frac{\partial H_y}{\partial x} &= \left.\frac{dH_y}{dx}\right|_{z=const} \\ &= \frac{1}{\Delta x}(H_y[i,k] - H_y[i-1,k])\end{aligned} \tag{3.23}$$

$$\begin{aligned}\frac{\partial H_y}{\partial z} &= \left.\frac{dE_z}{dx}\right|_{x=const} \\ &= \frac{1}{\Delta x}(H_y[i,k] - H_y[i,k-1])\end{aligned} \tag{3.24}$$

The differences between the array elements for spatial derivatives of E and H (the increment by one for the calculation of E field components, and decrement by one for H field components) occurs because of the offset nature of E and H, just like in the one dimensional equations.

The calculation loops become,

for each i, k

$$\begin{aligned}
Q_x[i,k] &= Q_x[i,k] + \Delta t \dot{Q}_x[i,k] \\
\dot{Q}_x[i,k] &= (1 - \Delta t \Gamma)\dot{Q}_x[i,k] + \Delta t(b_{11}Q_x[i,k] + b_{12}E_x[i,k] - F_{\mathrm{ISRS}}) \\
E_z[i,k] &= E_z[i,k] + \frac{\Delta t}{\epsilon_0 dx}\Big(H_y[i-1,k] - H_y[i,k]\Big) - \frac{b_{21}\Delta t}{\epsilon_0 + b_{22}}\dot{Q}_z[i,k]]
\end{aligned} \tag{3.25}$$

$$\begin{aligned}
Q_z[i,k] &= Q_z[i,k] + \Delta t \dot{Q}_z[i,k] \\
\dot{Q}_x[i,k] &= (1 - \Delta t \Gamma)\dot{Q}_x[i,k] + \Delta t(b_{11}Q_x[i,k] + b_{12}E_x[i,k] - F_{\mathrm{ISRS}}) \\
E_x[i,k] &= E_x[i,k] + \frac{\Delta t}{\epsilon_0 dz}\Big(H[i,k-1] - H[i,k]\Big) - \frac{b_{21}\Delta t}{\epsilon_0 + b_{22}}\dot{Q}[i,k]
\end{aligned}$$

$$t = t + \frac{\Delta t}{2}$$

for each i, k

$$H_y[i,k] = H_y[i,k] + \frac{\Delta t}{\mu_0}\left(\frac{1}{dx}\Big(E_z[i,k] - E_z[i+1,k]\Big) + \frac{1}{dz}\Big(E_z[i,k] - E_z[i,k+1]\Big)\right) \tag{3.26}$$

$$t = t + \frac{\Delta t}{2}$$

where the b coefficients now can potentially have different values for different polarizations, in the case of an anisotropic material. The equivalent equations for a TM simulation would calculate E_y, Q_y, $\dot{Q}_y$, H_x, and H_z.

Just like in the one dimensional case, the algorithm in Equations 3.25 and 3.26 is iterated for all space. Careful selections of the bounds of i and k are required for both loops; although both arrays have the elements $i = 0 \ldots (i_{\mathrm{MAX}} - 1)$ and $k =$

$0...(k_{\text{MAX}} - 1)$, the values are not calculated over the entire range. Equation 3.25 has the range $i = 1...(i_{\text{MAX}} - 1)$,$k = 1...(k_{\text{MAX}} - 1)$. Equation 3.26 has the range $i = 0...(i_{\text{MAX}}-2)$,$k = 0...(k_{\text{MAX}}-2)$. In effect, E fields are never calculated for $i, k = 0$ (the left side and bottom of the 2D array), and H fields for $i, k = i_{\text{MAX}}, k_{\text{MAX}}$ (the top and right of the array), but the (permanently 0) values are in turn used to calculate the other field. Conversely, the calculated E field at $i, k = (i_{\text{MAX}} - 1), (k_{\text{MAX}} - 1)$ and H field at $i, k = 0$ are never used to calculate anything other than their own value at the next time step.

3.4.2 3D simulation spaces

For a fully three dimensional simulation, there is once again only one simulation case- all three components of $\vec{E}$, $\vec{H}$, $\vec{Q}$, and $\dot{\vec{Q}}$ must be considered. Once again the simulation grid is defined so that spatial derivatives along one spatial coordiante implicitly hold the other coordinates constant, to yield the simulation cell shown in Figure 3-3.

3.5 Parallelization of the FDTD algorithm

Since many of the applications of Equation 3.16 require problem spaces larger than that can be easily afforded by a single computer, we parallelize the simulations by distributing equal portions of the problem space over the nodes of a distributed computing cluster. In the simple 1D case, parallelization is trivial, as E_z, Q_z, and H_y at the beginning and end of the distributed problem space can be passed between nodes. The procedure for two-dimensional simulation is more illustrative of the general technique and more easily depicted than the three-dimensional case.

Parallelization of the FDTD simulations onto m nodes is done by subdividing the problem space along one of the spatial axes into m equal segments, $u = 0...(m - 1)$. Each node calculates E, Q and H in the same way as for a serial simulation, but only for its value of u, passing the values of E and H along the boundary to the

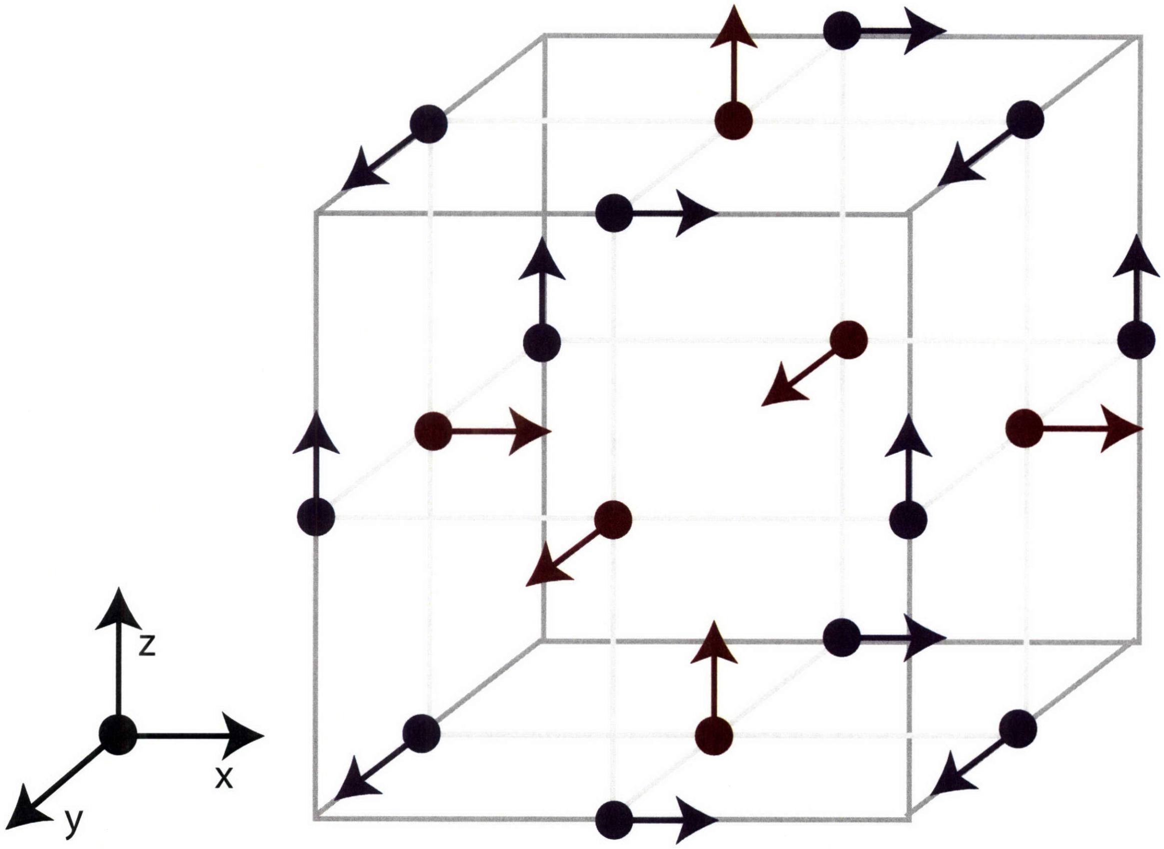

Figure 3-3: Simulation grid of a 3D FDTD simulation, with 3 simulated electric fields and 3 magnetic fields. The offset grid has electric fields polarized normal to the simulation unit cell faces, centered on the faces, and magnetic field polarized parallel to the cell edges, at the center of the edges.

neighboring segments as needed. The choice of dimension upon which to parallelize is arbitrary, but for simulation spaces which are distinctly non-cubic, parallelization by segmenting along the longest axis is proper parallelization, and yields the least parallelizaton overhead.

Since the Yee cell has offset E and H grids, only one field needs to be passed in each direction, with the direction determined by the relative subscripts used in the original algorithm formulation.

For our formulation, Equation 3.16 indicates that E fields at a given array index are calculated from H fields of the same index and one less. Thus, E fields are passed to subdivisions of greater u, H fields to subdivisions of smaller u. Each field is passed once per simulation time step, immediately after the values are calculated. Figure 3-4 illustrates parallelization in two dimensions. Note that since Q is coupled spatially only through the radiation field, no modifications are required for its parallelization: by transferring E, the need to transfer Q is mitigated.

The transferred values of E and H take advantage of the peculiarities of the E and H arrays describes in Sec. 3.3, the values being passed are the calculated, but unused, values from one extreme of the array, and they are being placed into the used, but not calculated spaces of the neighboring simulation space.

In one dimension, the fields have the boundary values given by

$$E[x,u] = \begin{cases} E[0,0] = 0 \\ E[0,u] = E[i_{\mathrm{MAX}} - 1, u+1], \{0 < u < (m-1)\} \end{cases} \tag{3.27}$$

$$H[x,u] = \begin{cases} H[i_{\mathrm{MAX}} - 1, m-1] = 0 \\ H[i_{\mathrm{MAX}} - 1, u] = H[0, u+1], \{0 < u < (m-2)\} \end{cases} \tag{3.28}$$

For example, our 48 GB total memory cluster yields a maximum simulation space U of roughly 600 to 800 billion cells in 2 dimensions, and 450 million cells in 3 dimensions. Given typical spacing values of 5 microns between cells, the cluster is capable of simulating polariton propagation in a 2D region of 100 cm^2, or a 3D region of 23 mm^3.

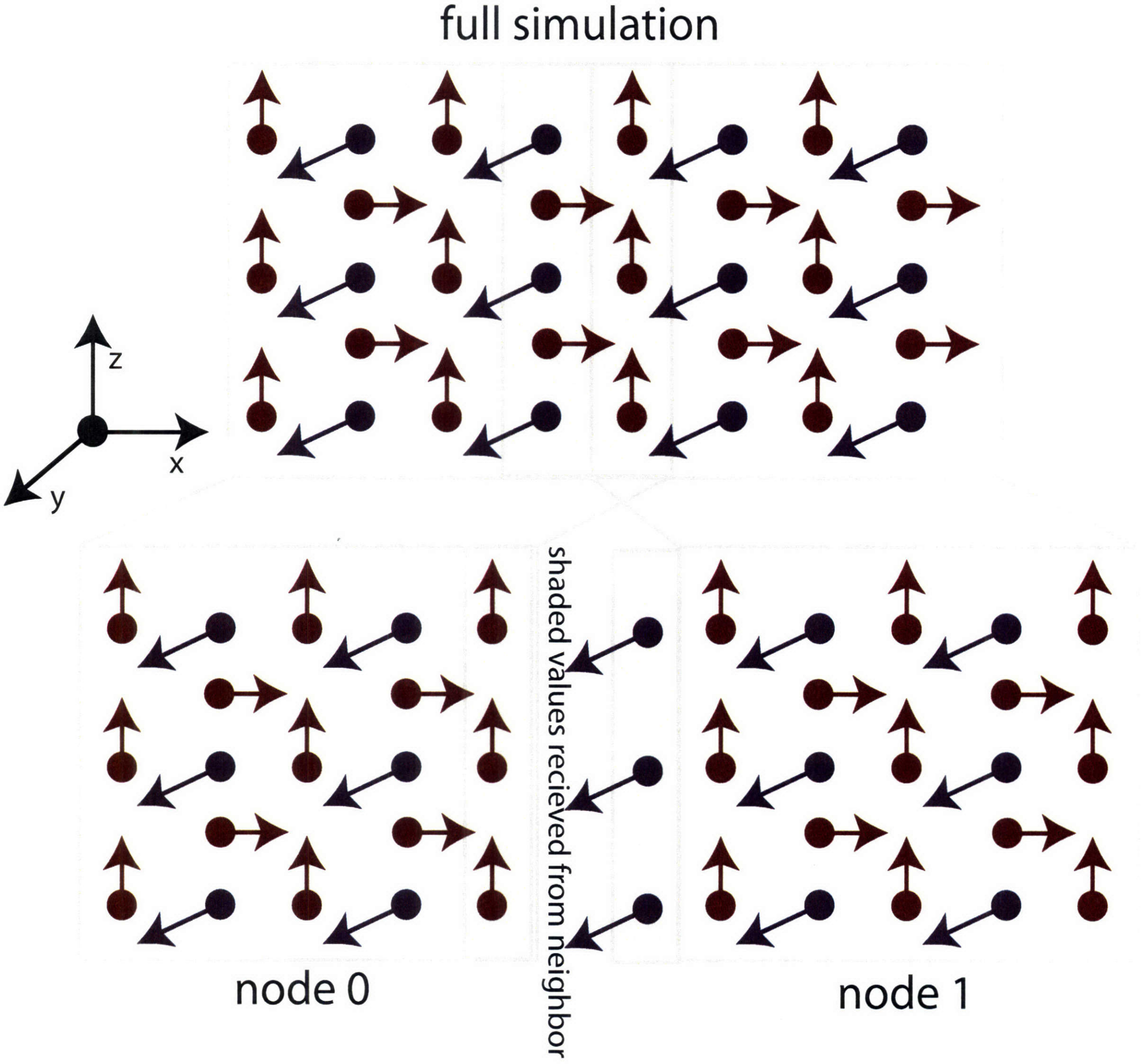
full simulation
z
x
y
shaded values recieved from neighbor
node 0
node 1

Figure 3-4: Simulation grid of a 2D FDTD simulation, parallelized across two nodes, node 0 and node 1. The shaded electric fields are passed from node 1 to node 0, the shaded magnetic from node 0 to node 1

Computation time for parallelized FDTD is almost perfectly linear in the number of cluster nodes, with the only deviation from non-linearity due to the overhead of passing data between neighboring nodes. Since the total data transfer between any two nodes of a properly parallelized three-dimensional U cell simulation will never exceed $U^{\frac{2}{3}}$ cells, of which only 2 field components need to be passed each way. In practice, this means the worst case scenario simulation yields a total transfer of 18 MB between adjacent nodes of a 48 GB simulation space.

3.6 Numerical Stability

Taking the difference of the two adjacent points is a reasonable approximation of the first derivative only in the limit that the function is well behaved and is slowly varying with respect to the time-step. Assuming realistic materials, electromagnetic waves are always continuous and differentiable, thus for the approximation to be valid, the waves just need to be slowly varying both temporally and spatially.

For spatial wavelengths of order λ, a grid spacing of $\lambda/10$ generally suffices to for numerical stability of the spatial derivative, and the Courant condition gives the maximum stable timestep.[54]

$$\Delta z \leq \frac{\lambda_{\min}}{10}, \tag{3.29}$$

$$\Delta t \leq \frac{\Delta z}{2c_0}. \tag{3.30}$$

In practice, fine material structures and strong dielectric contrast often require a smaller spatial grid spacing. Also in high dielectric materials or systems with high frequecy responses relative to their wavevector such as upper branch polaritons and higher modes of photonic crystals, the Courant condition may be insufficient to guarantee stability.

One advantage of these numerical systems is the ease of changing the requisite timesteps. In practice, when running a FDTD simulation of a system which may not be well behaved, taking the direct numerical difference of the simulation output of two simulations which only differ in time or spatial step, and watching for non-zero values is an indication that the simulation with the larger of the two steps is, at least, incorrect. Because of the floating point nature of the math involved, small deviations from zero are to be expected, but any variations larger than the PML reflections should be a sign of problems.

3.7 Boundary Conditions

The boundary conditions of a simulation determine what happens when simulated radiation reaches the bounds of the simulation space, and there are three cases that we consider, namely it can reflect off the simulation edge, be absorbed by the simulation edge, or propagate to the other side of the simulation space. Although absorptive boundary conditions are the most applicable to real world experiments, in that the simulated system is sitting in an effectively infinite space and radiation leaving the system can be expected never to return, it is the hardest to simulate, so the other two conditions are often used.

3.7.1 Reflective Boundary Conditions

The natural state of the simulations as defined in sections 3.3 and 3.4 is this form of boundary condition. The implicit zero values of the fields along the bounds of the simulation space due to the algorithm cause all tangential fields to be zero at all times at the boundary. This is the definition of a perfect conductor, one property of which is a lossless reflection, and no transmission. Schematically, radiation impacting the reflective surface should invert sign and direction of propagation, but be otherwise unchanged by the interaction, Figure 3-5.

A one dimensional system with reflective boundaries at 0 and d could be described as,

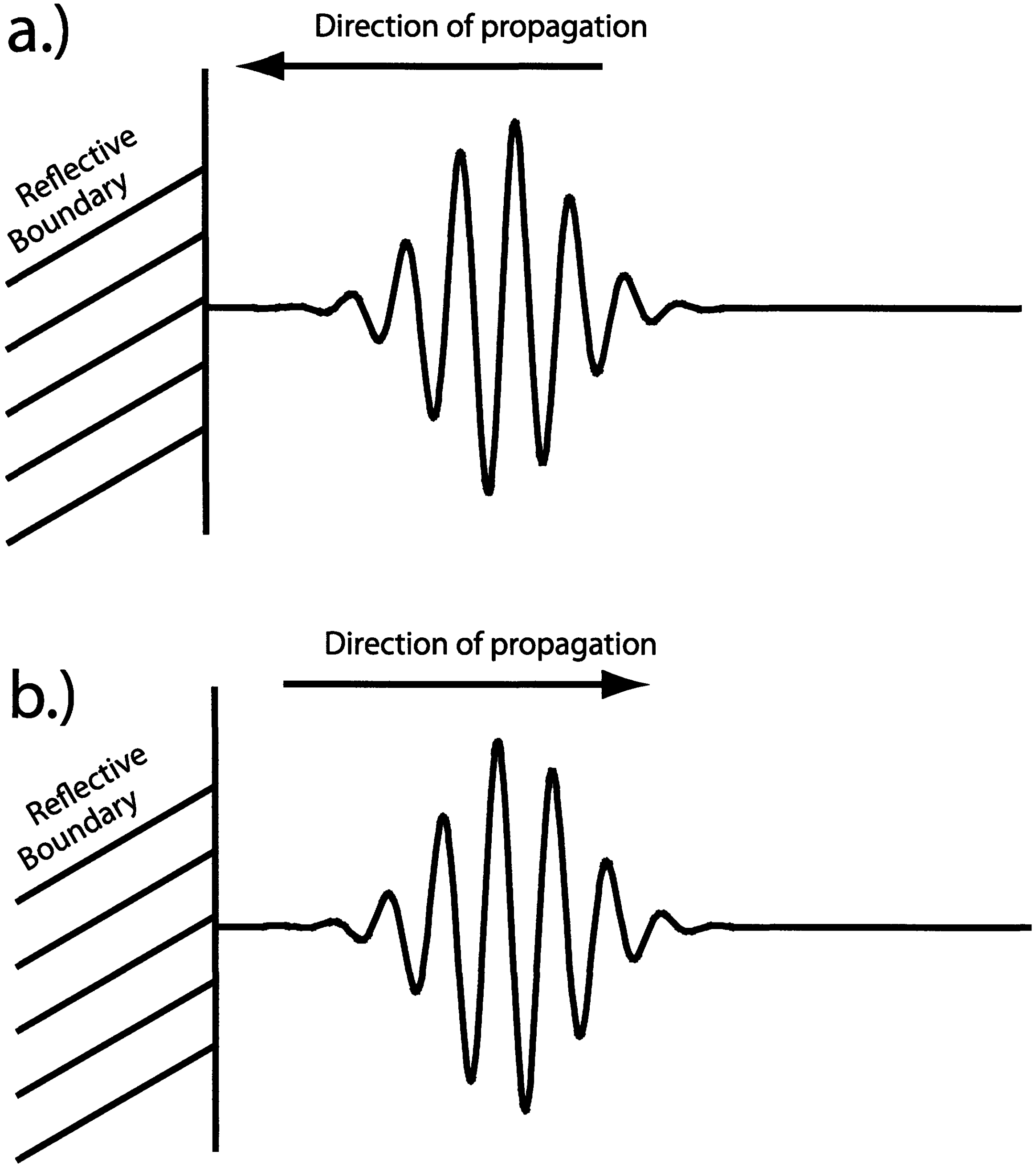
a.)
Direction of propagation
Reflective
Boundary
b.)
Direction of propagation
Reflective
Boundary

Figure 3-5: Schematic reflective simulation boundary, with a multi-cycle wave packet both before (a) and after (b) interaction with the simulation boundary.. The area labeled 'Reflective Boundary' is not defined within the simulation space but can be considered a perfect conductor because fields are forced to 0 at the bounds of the space. Impacting radiation switches sign and direction o f propagation, but is otherwise unchanged by the interaction with the bounds of the space.

$$\left.\begin{array}{l}\frac{\partial E_z}{\partial x} = -\mu_0 \frac{\partial H_y}{\partial t} \\ \frac{\partial H_y}{\partial x} = \frac{\partial D_z}{\partial t}\end{array}\right\} \quad 0 < x < d \tag{3.31}$$

$$\left.\begin{array}{r}E = 0 \\ H = 0\end{array}\right\} \quad \{x \leq 0, x \geq d\} \tag{3.32}$$

the solutions of which are of the form

$$\psi_n(x,t) = \sin\left(n\pi \frac{x}{d}\right) e^{i\omega t} \tag{3.33}$$

All waves impacting the boundaries thus reflect, and energy is fully conserved. To prevent numerical instabilities, all initial fields, whether generated through pumping, or just applied at $t = 0$ must smoothly intersect with the boundaries, so that the spatial derivatives which include the simulation boundaries have small values, or in terms of equation 3.33, $n_{\max}$ must still satisfy the courant condition.

The longest treatable wavelength of a reflective boundary condition simulation is twice the simulation space, but in practice it is much smaller, as the quantization of available wavelengths is severe at long wavelengths.

3.7.2 Periodic Boundary Conditions

A periodic boundary condition corrects for many of the flaws of reflective boundary conditions by allowing waves leaving one limit of the simulation space to continue propagation at the other side of the solution space, Figure 3-6. Thus, for the same system, defined for $x = 0...d$,

$$\left.\begin{array}{l}E(x) = E(x - nd) \\ H(x) = E(x - nd)\end{array}\right\} \quad n = \mathit{integers} \tag{3.34}$$

the solutions of which are now of the form

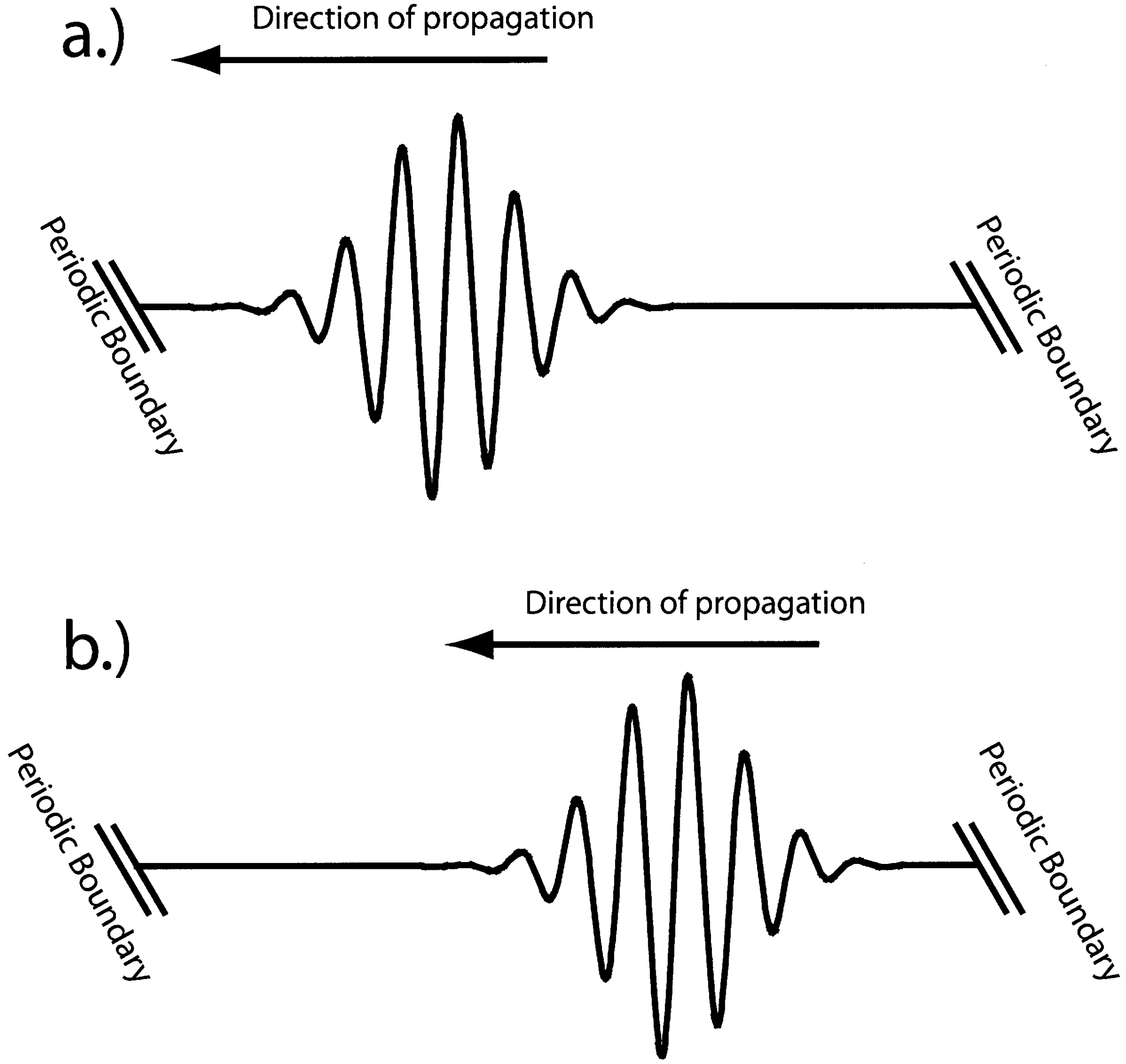
a.)
Direction of propagation
Periodic Boundary
Periodic Boundary
b.)
Direction of propagation
Periodic Boundary
Periodic Boundary

Figure 3-6: Schematic periodic simulation boundary, with a multi-cycle wave packet both before (a) and after (b) interaction with the simulation boundary.. The areas labeled 'Periodic Boundary' are not defined within the simulation space, and radiation impacting them continues on the opposite side of the simulation space unimpeded.

$$\psi_n(x,t) = \sin\left(2n\pi\frac{x}{d}\right)e^{i\omega t}. \tag{3.35}$$

For the purpose of simulation, the method of parallelization can be retasked to produce periodic boundary conditions from the reflective ones. Instead of only passing E fields between neighboring nodes u, as per equation 3.36, the nodes at the lower and upper limits ($u = 0$ and $u = m - 1$) also exchange data:

$$E[x,u] = \begin{cases} E[0,0] = E[i_{\text{MAX}} - 1, m-1] \\ E[0,u] = E[i_{\text{MAX}} - 1, u+1], \{0 < u < (m-1)\} \end{cases} \tag{3.36}$$

$$H[x,u] = \begin{cases} H[i_{\text{MAX}} - 1, m-1] = H[0,0] \\ H[i_{\text{MAX}} - 1, u] = H[0, u+1], \{0 < u < (m-2)\} \end{cases} \tag{3.37}$$

which even works for the non-parallelized case of $m = 1$.

3.8 Simulated Optical Pumping

As per Equation 2.42, the ISRS driving force applied to the phonon modes is proportional to the instantaneous intensity of the laser pump. This means that we do not in practice need access to the underlying carrier frequency and phase of the pump field for the purpose of FDTD simulation.

Consider analytically defined pump which can be expressed as a linear combination of seperable phase and amplitude terms,

$$E_{\text{pump}} = \sum_n E_n^{\text{ampl}}(x,y,z,t)E_n^{\text{phase}}(x,y,z,t) \tag{3.38}$$

$$\text{I}_{\text{pump}}(x,y,z,t) = |E_{\text{pump}}(x,y,z,t)|^2 \approx \sum_n |E_n^{\text{ampl}}(x,y,z,t)|^2 \tag{3.39}$$

Full FDTD simulation of the pump field is possible, but requires use of a simulation

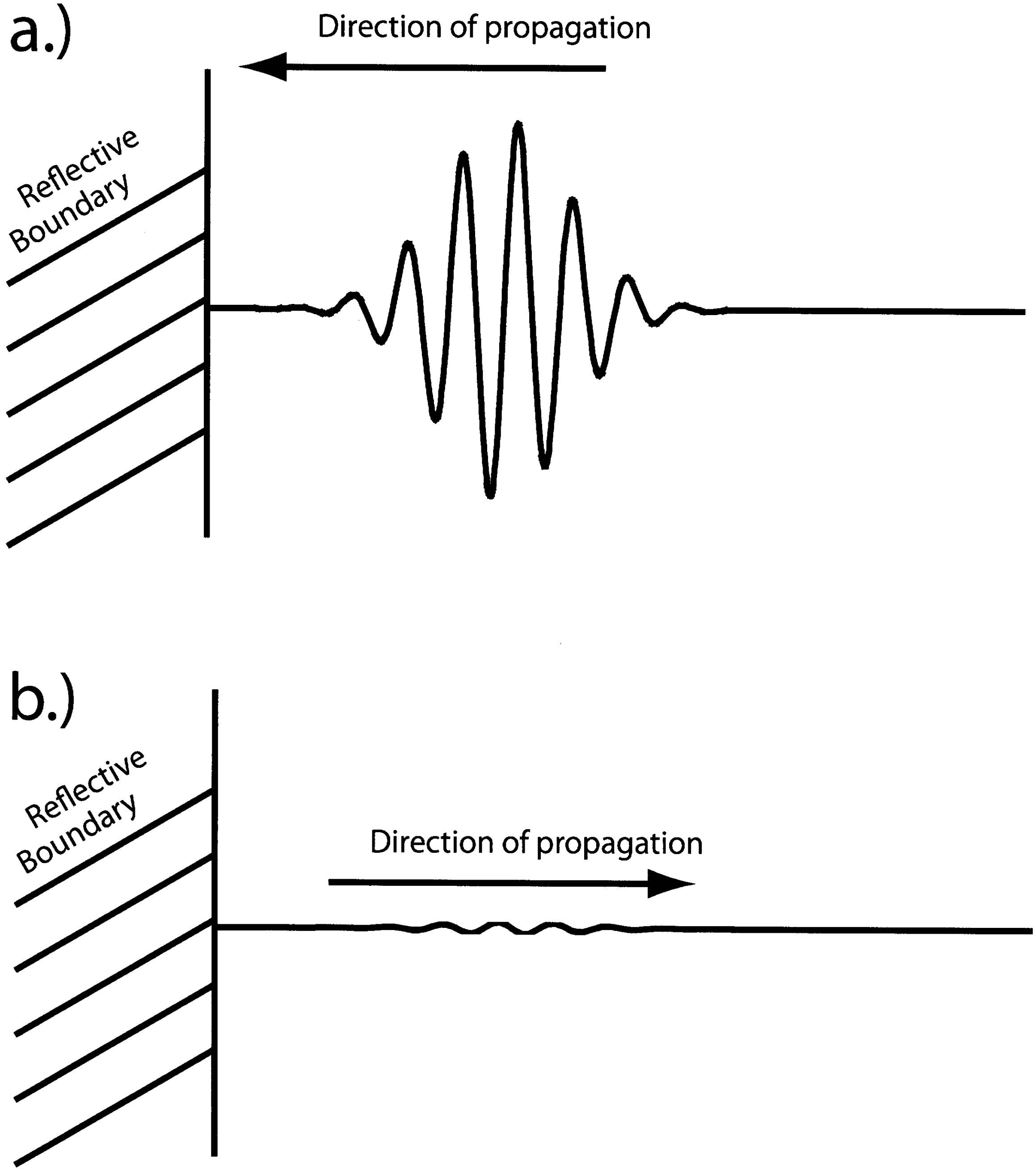
a.)
Direction of propagation
Reflective Boundary
b.)
Reflective Boundary
Direction of propagation

Figure 3-7: Schematic absorptive simulation boundary, with a multi-cycle wave packet both before (a) and after (b) interaction with the simulation boundary. The radiation is mostly absorbed by interaction with the perfectly matched layer (PML) pseudo-absorptive boundary, but a small amount of the original wave packet does reflect.

grid spacing capable of properly describing the input laser pulse. In the typical case of a 1̃00 fs, 800 nm pulse, this means grid spacings of 100 nm, which would cut the maximum simulatable volume by 5 orders of magnitude, and drastically slow down the simulation due to a time step 50 times smaller than needed for propagation of only the THz fields.

As the total energy conversion of pump into THz polaritons is on the order of 1%, and the THz index of refraction modulation for a strong 100 kV/cm response given by Equation 2.47 is under 0.1%, we make the assumptions of non-depleting pumps that are not influenced by any generated THz fields.

For the purpose of simulation, we consider three specific pump cases, of increasing simulation cost and increasing accuracy, fixed spot, ray optic, and gaussian beam.

3.8.1 Fixed Spot Pumping

In practice, for all but the thickest crystals, fixed spot is a sufficient approximation, in which we further approximate equation 3.39 to be separable into time independent x and z, and a time dependent $y(t)$,

$$\mathrm{I}_{\text{pump}}(x', y', z', t) = \mathrm{I}_x(x')\mathrm{I}_z(z')\mathrm{I}_{yt}(y', t), \tag{3.40}$$

where x' y' and z' are defined as the coordinates in the pump-beam frame, not the simulation space frame. For the common case of normal incidence pumping, this pump frame is the same as the simulation frame, but off-normal pumping will result in x' y' and z' being linear combinations of their simulation-space counterparts.

For the simple case of a gaussian line focus of width η (FWHM) and pulse duration τ (FWHM), centered around x_0, t_0, and with pumping at normal incidence to xz, we could write a desired pump field as

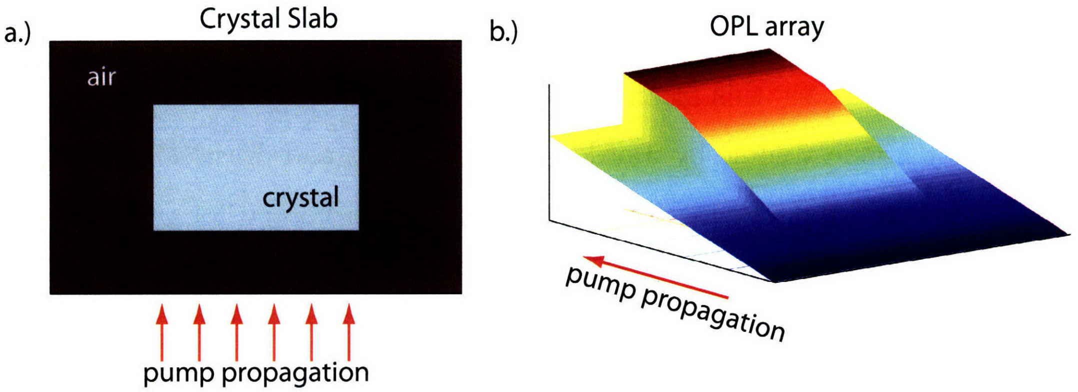

Figure 3-8: Optical Path Length (OPL) array for a TM simulation assuming a normal incidence pump. The material file shown in (a), with the pump fields entering the simulation space as shown, yields the OPL array shown in b. The z axis of the OPL array gives the total amount of time a pump wavefront takes to reach that x and y coordinate in the crystal. The pump beam takes longer to propagate through the substrate crystal than it does to propagate through the surrounding air.

$$\varrho(\alpha, \alpha_0, \eta) = e^{-\frac{(\alpha-\alpha_0)^2}{2\ln(2)\eta^2}} \tag{3.41}$$

$$\mathrm{I}_{\text{pump}}(x', y', z', t) = \varrho_x(x, x_0, \eta)\varrho_z(z, z_0, \infty)\varrho_{yt}(t + t'(y), t_0, \tau). \tag{3.42}$$

The function $t'(y)$ is simply the amount of time a pump beam takes to get to that y coordinate value, assuming that it starts initially at y=0. For a simple, uniform dielectric material of index n, this reduces to,

$$t'(y') = \frac{y'}{c_0 n} \tag{3.43}$$

but to allow for arbitrary shapes and thicknesses of material, the values are calculated iteratively, and stored into a static Optical Path Length array OPL for a given simulation. For a bulk crystal in air, a typical OPL array for a 2D simulation resembles Figure 3-8, where the z axis corresponds to the amount of time a pump pulse takes to get to a given spatial point x, y.

$$
\begin{aligned}
t'(x',0,z') &= t_0(x',z') &\quad (3.44)\\
t'(x',y',z') &= t'(x',y'-\Delta y,z') + \frac{\Delta y}{c_0 n(x',y',z')} &\quad (3.45)\\
\mathrm{OPL}[x',y',z'] &= t'(x',y',z') &\quad (3.46)
\end{aligned}
$$

Combining equations 3.46 and 3.42 yields,

$$
\mathrm{I}_{\mathrm{pump}}(x',y',z',t) = \varrho_x(x,x_0,\eta)\varrho_{yt}(t-OPL[x',y',z'],t_0,\tau). \quad (3.47)
$$

which is the recipe for a line focus pump assuming an infinite simulation space, and a simulated crystal significantly thinner than the raleigh distance of the focused pump.

Unfortunately, the simulation space is never infinite, and for numerical stability of the absorptive boundary condition, the pump fields must be 0 at the boundaries of the solution space. To effect this, the pump fields are multiplied by envelopes sinusoidal in x' and z'.

$$
\mathrm{I}^{\mathrm{corrected}}_{\mathrm{pump}}(x',y',z',t) = \mathrm{I}_{\mathrm{pump}}(x',y',z',t)\sin(\pi\frac{x'}{\mathrm{ie}'\Delta x'})\sin(\pi\frac{z'}{\mathrm{ke}'\Delta z'}), \quad (3.48)
$$

where ie' and ke' are the extreme values (maxima) of the array indicies i' and k', and are thus number of array elements in the $\hat{x}'$ and $\hat{z}'$ directions within the OPL array.

Although this pumping approximation has been expressed as for a single gaussian pump, the static nature of the OPL for a given pump propagation direction allows the method to be expanded to encompass multiple-pulse excitations. One important use of multiple excitations is in polariton amplification, where multiple excitation events are timed and spatially placed so that they constructively interfere with an already

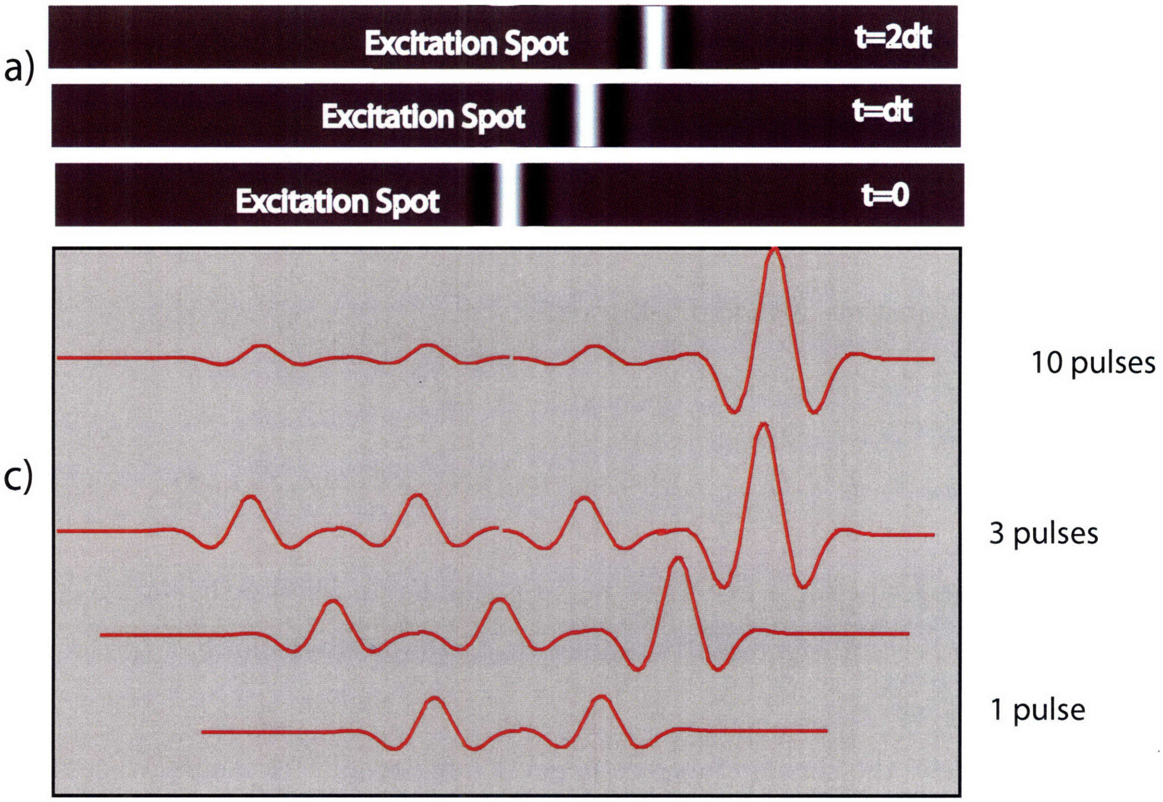

Figure 3-9: Polariton Amplification through multiple excitations, diagramatically depicted in 1D. At t=0, a pump pulse is incident on the crystal, and produces leftward and rightward going polariton waves. At a time Δt later, a second excitation pulse hits the crystal to the right of the original excitation region, thus producing constructive interference between the two rightward going waves, and destructive interference between the leftward going waves.

propagating phonon-polariton wave, Figure 3-9, plotting electric field as a function of space and time yields Figure 3-10.

3.8.2 Ray Optic pumping

In the limit where there is some transverse spatial variation in the pump beam as it propagates through the crystal, a more generic case of pumping is required. The simplest case is a thick crystal, where the pump is only strongly focused in some internal region of the crystal.

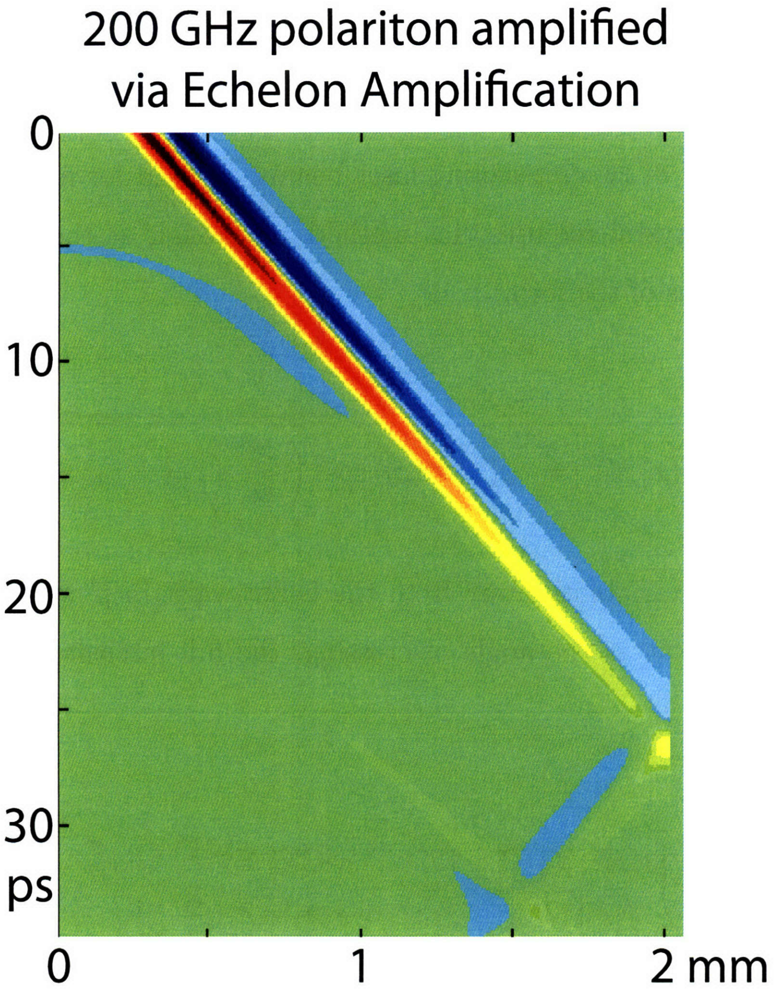

Figure 3-10: Space-Time plot of simulated echelon amplification, using Fixed-Spot pumping for generating the field, including 10 excitation events over the time period 0-8 ps, and detected using simulated 800 nm imaging.

Revisiting the separable equation 3.40, we now treat y' as the optical axis of the experiment, and redifine the equations as:

$$\mathrm{I}^{\mathrm{R-O}}_{\mathrm{pump}}(x', y', z', t) = \mathrm{I}_x(x', y')\mathrm{I}_z(z', y')\mathrm{I}_{yt}(y', t),, \tag{3.49}$$

where all the pulse-propagation time dependance is entirely within the I_{yt} term.

Proper treatment of two interfering laser beams, as used for narrowband pumping within a thick crystal requires this method. Although at the beam waist, the interference pattern is of the form,

$$\mathrm{I}^{\mathrm{R-O}}_{\mathrm{pump}}(x', z') = \varrho(x', x0, \eta)\cos^2\left(\frac{2\pi x'}{\lambda_x}\right)\varrho(z', z_0, \infty), \tag{3.50}$$

there is actually variability away from the beam waist in y' as the beams cross each other. Defining ϕ as the angle of crossing, the full intensity pattern in three dimensions becomes:

$$\begin{aligned}
\sin\left(\frac{\phi}{2}\right) &= \frac{\lambda_{\mathrm{pump}}}{2\lambda_x} && (3.51)\\
\cos\left(\frac{\phi}{2}\right) &= \frac{\lambda_{\mathrm{pump}}}{2\lambda_y} && (3.52)\\
\eta(y') &= \eta_0\sqrt{1+\left(\frac{y'\lambda_{\mathrm{pump}}}{\pi\eta_0^2}\right)^2} && (3.53)\\
\mathrm{I}^{\mathrm{Envelope}}_{\mathrm{pump}}(x', y', z', t') &= \varrho(x', x0, \eta(y'))\varrho(z', z_0, \infty)\varrho_{yt}(t - OPL[x', y', z'], t_0, \tau) && (3.54)\\
\mathrm{I}^{\mathrm{Periodic}}_{\mathrm{pump}}(x', y') &= \cos^2\left(\frac{2\pi x'}{\lambda_x}\right)\cos^2\left(\frac{2\pi y'}{\lambda_y}\right) && (3.55)\\
\mathrm{I}^{\mathrm{E-O}}_{\mathrm{pump}}(x', y', z', t') &= \mathrm{I}^{\mathrm{Envelope}}_{\mathrm{pump}}\mathrm{I}^{\mathrm{Periodic}}_{\mathrm{pump}}, && (3.56)
\end{aligned}$$

where $lambda_{\mathrm{pump}}$ is the pump wavelength inside the crystal.

3.8.3 Pumping at an angle

The generation of the OPL array above has been simplified by assuming normal incidence pumping, whereas many experiments in practice use pump beams which impact the crystal very far off normal. In the case of patterned materials in three dimensions, or grazing incidence excitation where the effects of pumping near the edge of the crystal are important, there is no recourse but to fully simulate the beam as in the next section. Thankfully cases where that is necessary are rare, and instead slight modifications of the ray optic method are sufficient.

Consider a pump beam incident at 10° from normal incidence, near the middle of a thin but transversally large crystal. Although the pump beam will refract upon encountering the crystal, the angle of propagation in the air before contacting the crystal and after leaving the crystal are unimportant as far as the simulation is concerned, and thus refraction need not be directly considered. The pump is merely assumed to pass through the cladding-crystal interface without refracting, and the effects of refraction are on temporal delay and aspect ratio are incorporated into the initial equations for the pump.

Defining ϕ and θ as the pump angles off the normal inside the crystal, in the yz and xz planes respectively, yields the following equations for x', y', and z'.

$$x' = \mathrm{rot}_x(x, y, z, \phi, \theta) \tag{3.57}$$

$$y' = \mathrm{rot}_y(x, y, z, \phi, \theta) \tag{3.58}$$

$$z' = \mathrm{rot}_z(x, y, z, \phi, \theta) \tag{3.59}$$

Aspect ratios are corrected by dividing all physical distances by their corresponding α_{xyz} e.zg. η is replaced by $\frac{\eta}{\alpha_x}$. Lastly, the initial $y' = 0$ values of the OPL array need to correct for the change in delay as the beam crosses the interface.

$$OPL(x', z', y' = 0) = (n_c - n_0)\cos\phi\cos\theta \tag{3.60}$$

This correction factor is due to the delayed entrance of parts of the pump into the polariton generating crystal, due to further propagation in air.

This angled pump method was well used to simulate the polariton response within $LiNbO_3$ of a glancing incidence pump, for the purpose of understanding transient x-ray scattering[9]. Because of the very large scattering cross-section of x-rays incident on LN, the effects of transient diffraction off of the soft mode of LN will be dominated by signal from the first few unit cells of the surface of the crystal, and thus polariton excitations which remain near the surface will dominate the signal. Transient X-ray diffraction was detected off of the shallower angled, weaker excitation near the top face of the crystal, which corresponded to polariton generation only at the crystal/air interface. The simulated polariton response is shown in Figure 3-12.

3.8.4 Simulated Beam Pumping

When the approximate methods of generating an analytic pump field as a function of time fail, or an experimentally measured pump field is desired, a fully numerical pump field can be used for driving instead.

Typically, this pump field is generated through full FDTD simulation of the pump beam propagation, using a simplified, fixed dielectric constant material, for speed of simulation and due to the far off resonance nature of the pump light relative to any modes of typical materials of interest.

The full 4 dimensional (3 spatial, 1 temporal) pump field is recorded, rectified, and down sampled spatially and temporally to the grid of the desired THz simulation, as per figure 3-12.

Although this method is by far the most exact, it is rarely useful in practice, because the simulation to generate the pump field requires typically significantly longer to run, than the entire THz polariton simulation would have required otherwise.

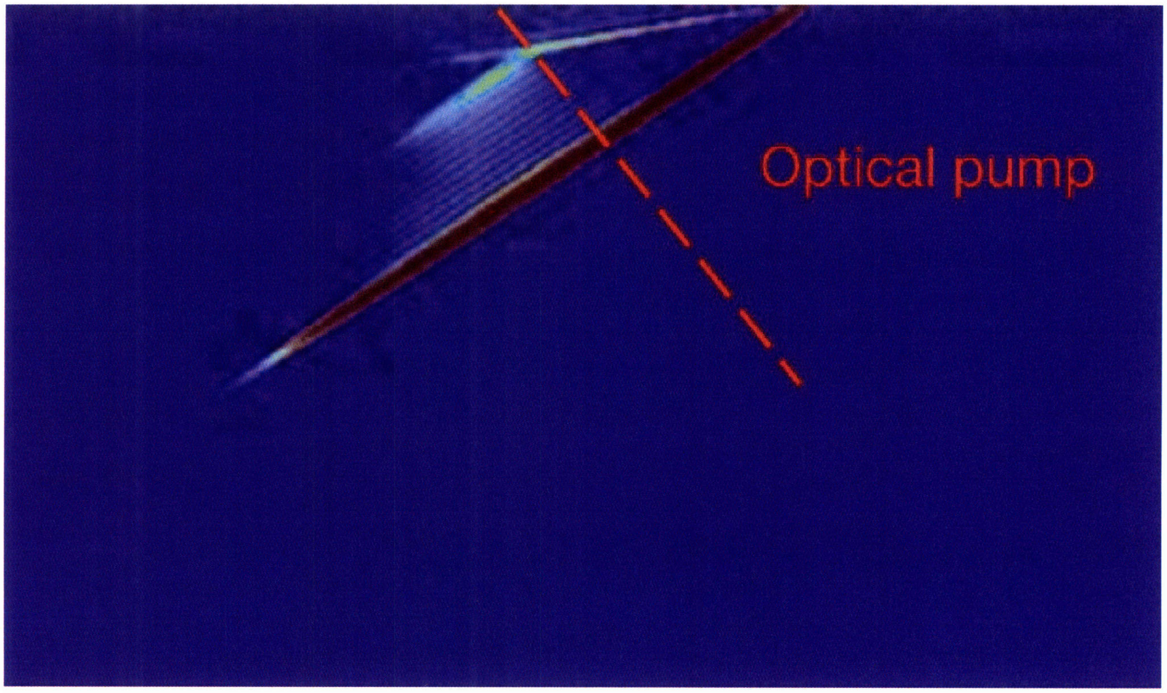

Figure 3-11: Simulated polariton response using a 2D TM simulation of generation due to an angled pump.[9] Transient X-ray diffracaction occurs off of the weaker polariton wavefront which in nearly parallel to the top surface of the crystal. Unlike in standard polariton pump-probe experiments, where the cherenkov cone, and the the polariton angle is given by the ratio of pump and THz indicies of refraction, the glancing incidence pump in this experiment produced a generation spot which skittered along the surface of the crystal at $1.1c_0$, thus producing an 8° 'forward angle'.

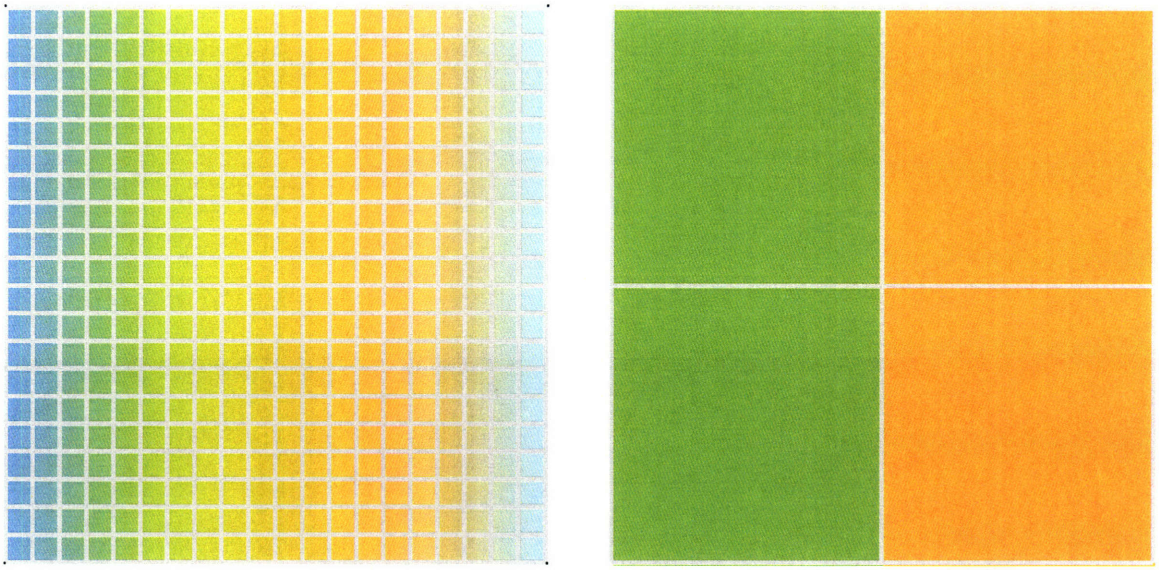

simulated pump field

downsampled fdtd pump field

Figure 3-12: Simulated fdtd pump field of a line focus excitation before and after down sampling. The degree of down sampling is excessive, as the pump field is no longer smoothly varying on the order of the simulation spatial step. A smaller dx and dy is needed.

3.9 Simulated Polariton Imaging

Polariton Imaging through the pockel's effect, as described in section 2.6 is approximated for the purpose of simulation by a spatially and temporally dependent integration of the normal mode displacements of the crystal.

An additional OPL array is generated as per equation 3.46, using the appropriate values of $n(x', y', z')$ for the probe wavelength, and appropriate axes for the direction of probe beam propagation.

The temporal differential of this array is calculated,

$$\mathrm{dOPL}[i, j, k] = \mathrm{OPL}[i, j, k] - \mathrm{OPL}[i, j-1, k]. \tag{3.61}$$

To do the time-dependent integration, an array R of the same dimension of the simulation is generated, and zeroed, but instead of having entirely spatial dimensions, it has one dimension which is temporal, and has $\frac{\mathrm{OPL_{MAX}}}{dt}$ elements.

At each timestep of the simulation, the value of R is incremented by the nearest value of Q,

$$R[i,j,k] = R[i,j,k] + Q[x(i), y(j), z(k)] \tag{3.62}$$

Next, *remainder* $\left(\frac{t}{\mathrm{dOPL}}\right) < dt$ is evaluated for each location $R[i,j,k]$, and if true, $R[i,j,k] = R[i,j-1,k]$.

The probe output,

$$Probe[i,k,t] = R[i, j_{\mathrm{MAX}}, k] \tag{3.63}$$

is thus the integrated Q values for a probe wavefront leaving the simulation space at time t.

The probing algorithm is thus for each time t:

for each i, j, k

$$\begin{aligned} R_x[i,j,k] &= R_x[i,j,k] + Q_x[x(i,j,k), y(i,j,k), z(i,j,k)] \\ R_y[i,j,k] &= R_y[i,j,k] + Q_y[x(i,j,k), y(i,j,k), z(i,j,k)] \\ R_z[i,j,k] &= R_z[i,j,k] + Q_z[x(i,j,k), y(i,j,k), z(i,j,k)] \end{aligned} \tag{3.64}$$

if $(t\%\mathrm{dOPL}[i,j,k] < dt)$

$$R[i,j,k] = R[i,j-1,k] \tag{3.65}$$

$$Probe[i,k,t] = R[i, j_{\mathrm{MAX}}, k] \tag{3.66}$$

Based on equation 2.47, it is actually possible to calculate the actual probe beam phase shifts from these values of $Probe[i,k,t]$, but for most experiments, simply retaining $Probe_z$, is sufficient, and proportional to an experimental probe image.

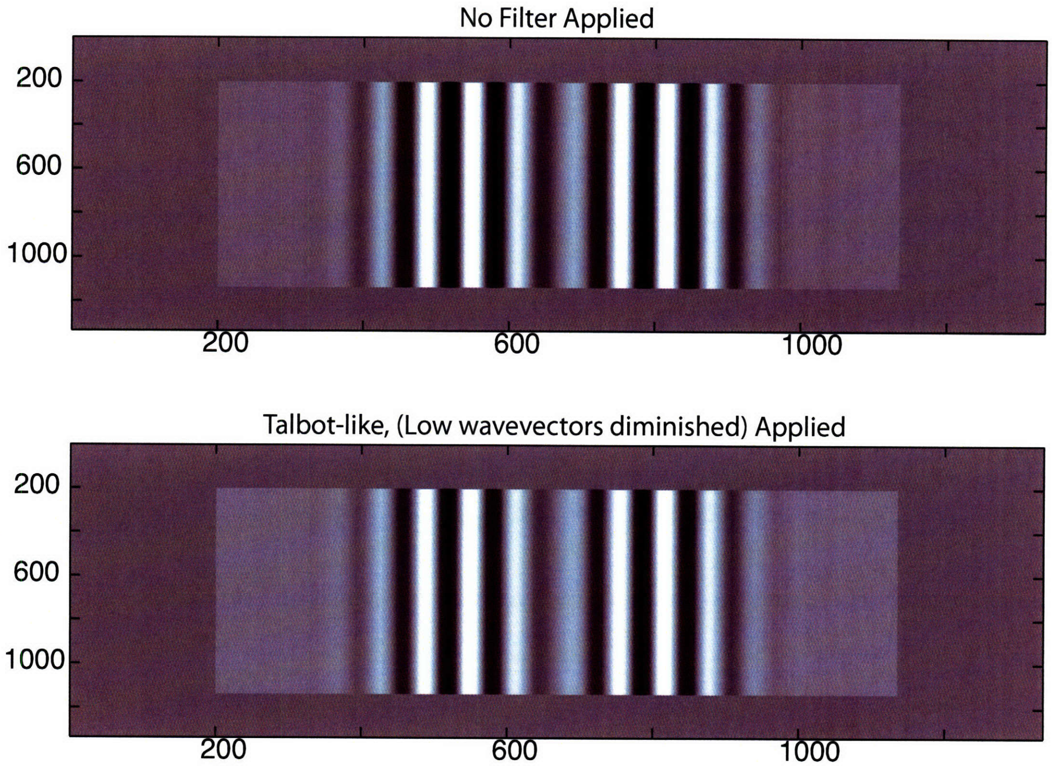

Figure 3-13: Simulated Probe images from full 3D simulations of 300 GHz radiation propagating within 100 μm thick $LiNbO_3$, both before and after a Talbot imaging filter which de-emphasizes low wave-vectors was applied to the probe data. Overall, fringes have become less sharp due to the applied filter, and a small carrier phase shift of approximately 20° has occured.

3.9.1 Talbot Imaging and Interferometry

As described by Peter Meier[41], no experimental method of polariton detection is in practice an exact replica of the actual fields inside the crystal, and different methods will have differing frequency and spatial inaccuracies.

The best way to deal with these inaccuracies from a simulation standpoint is to apply them entirely after the fact, as spatial frequency dependent filters upon the simulated probe output. For example, multimode propagation inside a 100 micron LN slab, appears in Figure 3-13, both before and after correction for the inaccuracies of Talbot imaging.

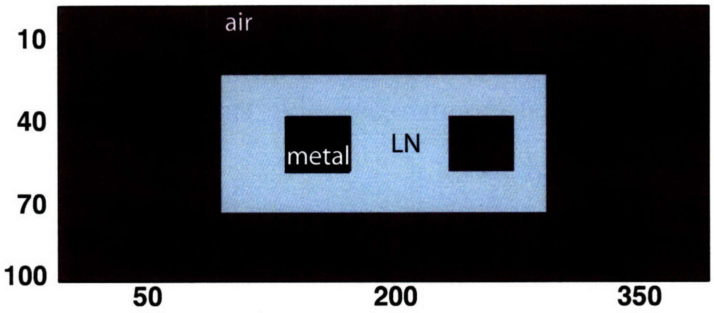

Figure 3-14: Patterned material array for the 2D simulation of a $\mathrm{LiNbO_3}$ crystal with a square air hole and square metal region.

3.10 Simulation of Patterned Materials

As alluded to in previous sections, the case of Q defined for all space is rarely a good approximation of experimental conditions, and in fact, for the case of an absorptive boundary condition, not tractable. For these reasons, the ability of the FDTD method to deal with arbitrarily shaped media is ideal.

For each point in the simulation space, it is possible to define the material by specifying material values such as ε_0, ε_r and b_{ij}. To this end, a material array $\mathrm{MAT}[i, j, k]$ can be defined, where its values correspond to what material exists at that grid point, as per Figure 3-14, and the constants in the FDTD equations replaced by functions such as

$$\varepsilon_r = \varepsilon_r(\mathrm{MAT}[i, j, k]). \tag{3.67}$$

Although it is not needed to calculate values of Q for regions without a coupled oscillator, such as air regions, it is not harmful, as the coupling $b_{12} = 0$ yields no change for Q.

3.11 Simulation optimizations

FDTD simulations of large 3D systems requires long computational times on the order of days for even relatively short (~10 ps) simulations, and the time increases by orders of magnitude for any simulation which is too large for the available memory on the simulation computers.

To allow the simulation of large systems in reasonable timeframes, there are a significant number of optimizations used.

3.11.1 Memory use optimizations

Memory optimizations only become particularly important for full three-spatial dimension simulations, as all two and one dimensional simulations typically have at least an order of magnitude fewer grid points to consider.

For a three dimensional simulation, most important part of the simulation design is the minimization of the number of values that have to be retained for each grid locus of the simulation. There is no choice but to keep track of the three components of E, H, Q and $\dot{Q}$, but as few ancillary arrays as possible should need to be maintained, and other arrays that fill the full space should typically use as small data types as possible.

Typically, in addition to the 12 physical field arrays, only one other three dimensional arrays which is also maintained as 64 bit floating point numbers are required, the space-time integrating probe array R. Potentially, if dual-polarization probing is simulated, one other full sized 64 bit array corresponding to the other probe polarization must be maintained, and if probing is not considered, none of these arrays are used.

By re-normalizing units, so that the magnitudes of E, H, and Q are all close to unity, it is practical to use smaller 32 bit floating point values to describe all these fields for simulations near equilibrium. Unfortunately, the unit conversions from a re-normalized system are especially brutal, and the optimization fails spectacularly in the limit of anharmonic behavior. In practice, this optimization is only worth using on computer architectures that natively support only 32 bit floating point numbers, as it is also a significant speed increase in this case.

The OPL arrays for both pump and probe are also full sized floating point arrays, but use 32 bit floating points to halve the amount of memory required for maintaining them.

One last full sized arrays corresponding to the material array is maintained as an 8 bit integer, limiting the number of materials available per simulation to 256, typically only 2-3 materials are needed anyways.

The PML integral fields are not defined within the bulk of the simulation, only existing in the regions along the edges of the full simulation space. These arrays are not defined on surfaces between simulation nodes either. Unfortunately, to accomplish this, the internal loops of the simulation were segmented into boundary regions and internal regions, at the cost of roughly 20% longer time-steps, and the cost could easily have been much worse without creative organizing of the iteration order of the algorithm based on the field being calculated.

3.11.2 Speed optimizations

Often competing with memory optimizations are tricks played to speed up each timestep of the simulation.

At the greatest cost to memory use, the Q arrays are defined everywhere. Since we are concerned with simulation arbitrarily shaped materials for the most part, there is no way to creatively tune the loops as was done for the PML boundary arrays.

The calculation of pump intensities is fairly computationally intensive, requiring much more than the basic arithmetic required to calculate Q, E and H in its absence. Because of this computational cost, and the practical consideration that pumping usually only occurs for some small fraction of the overall simulation time, the temporal loop is split into two segments, one that allows pumping, and calculates its effects, and another part that ignores the possibility of pumping.

Probing is very time-intensive, more than doubling the amount of time a simulation takes, even for the simplest probe geometries (single polarization, normal incidence). Because of this, probing is always disabled, unless explicitly being considered.

The OPL arrays are themselves a speed optimization. It would be possible to calculate the delay of pump or probe getting to a grid point whenever it was being considered, but the speed costs of this outweigh the memory costs of retaining the information. Non-normal incidence pumping and probing would be especially difficult trying to calculate these values in situ.

One thing which upon reflection should have been obvious is finding ways at all costs to avoid *if* statements inside the main loops. It is far better to break up a loop into three seperate loops, as is done in the case of PML boundaries (near one edge of the space, in the middle, and near the other edge), than to use if statements and be able to write one single loop covering all three cases.

Chapter 4

Phonon-polaritons in Bulk Materials

This work produced in collaboration with David W. Ward of the Massachusetts Institute of Technology.

In this chapter we look at the general experimental methods of polariton generation and detection, especially as is applicable to propagation in bulk (thick) crystals of $LiNbO_3$ (LN). Both broad and narrowband THz excitations are considered, and excitation irregularities in the depth of the crystal are characterized.

4.1 Experimental Methods

Two different laser systems were used for phonon-polariton experiments: a home-built Ti:sapphire multi-pass amplifier (800 nm central wavelength, 50 fs, 1 kHz repetition rate, 900 μJ/pulse), seeded by a KLM Labs TM-1 oscillator (790 nm central wavelength, 15 fs, 76 MHz repetition rate, 3 nJ/pulse), and a Coherent Legend Ti:sapphire regenerative amplifier (790 nm, 40 fs, 1 kHz repetition rate, 2.5 mJ/pulse) seeded by the same oscillator.

The polariton imaging methods used are all a variant of the typical ultrafast pump-probe technique, in which a single laser pulse is split into a pump and probe

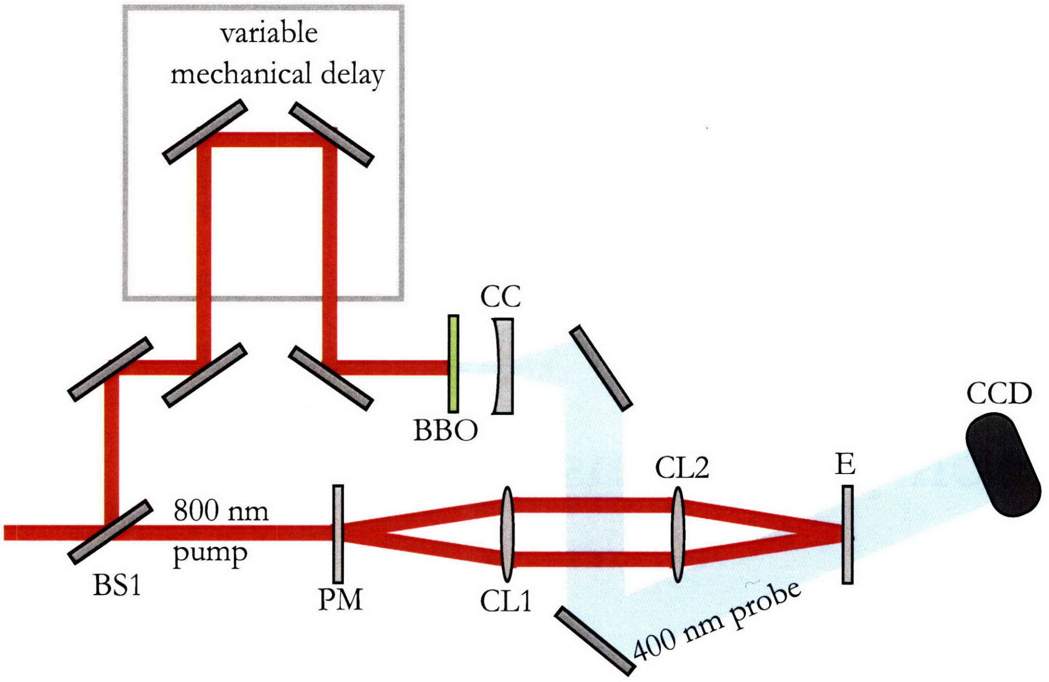

Figure 4-1: Experimental setup for real-space polariton imaging, where an 800 nm pulse is split by a 90:10 beam splitter (BS1) to create the pump and probe pulses, and the probe is variably delayed using a mechanical delay stage, then frequency-doubled by a 100 μm BBO crystal. The beam is then expanded using a concave spherical lens (CC) to the so that when passed through the sample, as shown, at about 10° off normal, it fully illuminates the entire region of interest (E), and then is imaged onto a CCD. The pump geometry shown is for narrowband excitation, using a transmissive binary phase mask (PM) to generate two beams which are crossed at the sample by using a 1:1 cylindrical telescope (CL1, CL2).

pulse using a beamsplitter, and one of the pulses is variably delayed by a mechanical delay stage. The pulses are then crossed at the sample, where a modulation of the probe beam due to phonon polaritons is produced, as shown in Figure 4-1.

The experimental images were collected using two different imaging systems. The images in thin films and bulk materials were collected using a Pulnix 3000 camera (600x400 resolution, and 8 bit pixel depth), which allows qualitative measurements of the fields. The work in patterned materials, such as waveguides, mode converters and photonic crystals was collected using a Princeton Instruments Pixis 2048 camera (2048x2048 resolution, 16 bit pixel depth), allowing for quantitative comparison of field amplitudes.

The crystals used for these experiments were poled, x-cut $LiNbO_3$, most were doped with 5% mass fraction MgO to reduce photo-refractive effects. This uniaxial crystal has strong electro-optic coefficients, is readily commercially available in high quality, and exhibits IR and Raman-active phonon modes with light polarizations along both the ordinary and extraordinary axes, making them ideal for polariton generation and detection.

4.2 Polariton Generation Through ISRS

Phonon-polaritons were generated within LN by focused amplified femtosecond pulses through impulsive stimulated Raman scattering, as described in section 2.5. Equation 2.42 indicates that $F_{\mathrm{ISRS}} \propto I_{\mathrm{pump}}$, and thus the polariton wavepacket form and amplitude is determined by the pump intensity profile. The frequencies generated are determined by the dispersion relation of the system driven, as per Figure 4-2.

Most polariton excitations fall into two general categories, broadband and narrowband.

4.2.1 Broadband Generation

Broadband, roughly single-cycle phonon-polaritons are generated by cylindrically focusing the pump light onto the crystal, with the dimension of focusing corresponding to the lateral dimension of propagation, as shown in Figure 4-3. The beam waist w_0 of the pump beam at the focus is given by,

$$\lambda_{\mathrm{center}} = w_0 = \frac{4\lambda}{\pi}\frac{F}{D}, \tag{4.1}$$

where F is the focal length of the lens used, D the diameter of the spot incident on that lens, λ is the wavelength of light (usually 800 nm), and $\lambda_{\mathrm{center}}$ is the central wavelength of the polariton wavepacket that is generated.

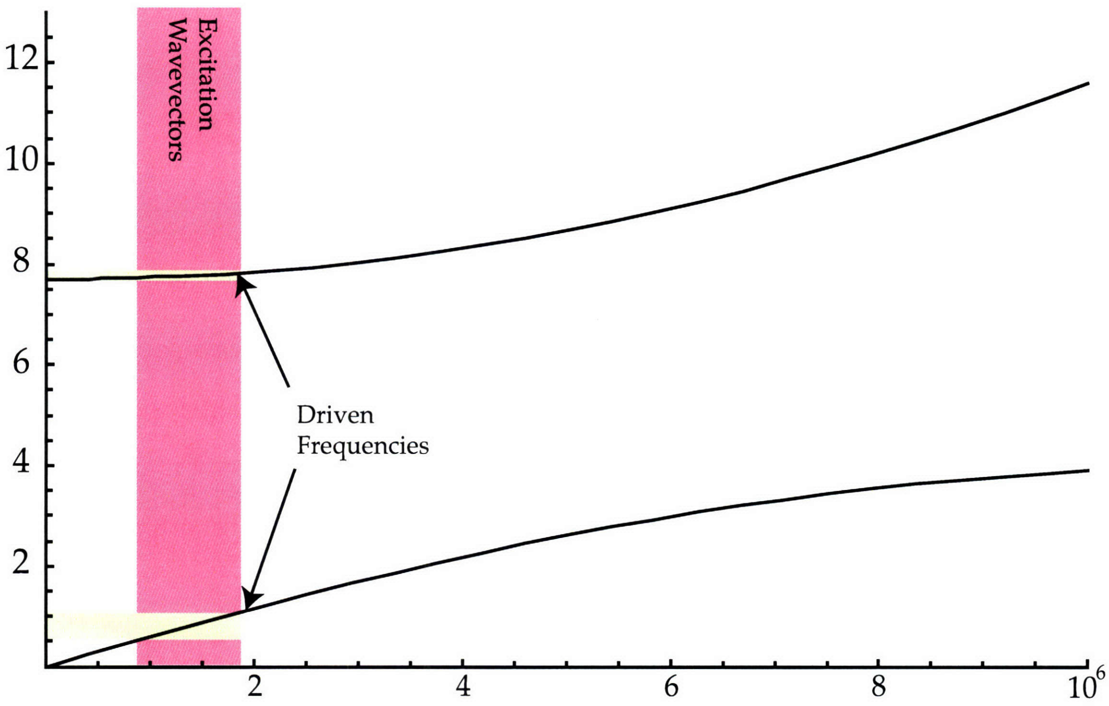

Figure 4-2: Dispersion curve of bulk LN, showing the excitation wavevector of a broadband polariton excitation, and the resultant frequencies. Driving wavevectors from 0.8-1.9 cm^{-1} yields frequencies of 0.5-1 THz in the lower polariton branch, and 7.7-7.9 THz in the upper branch.

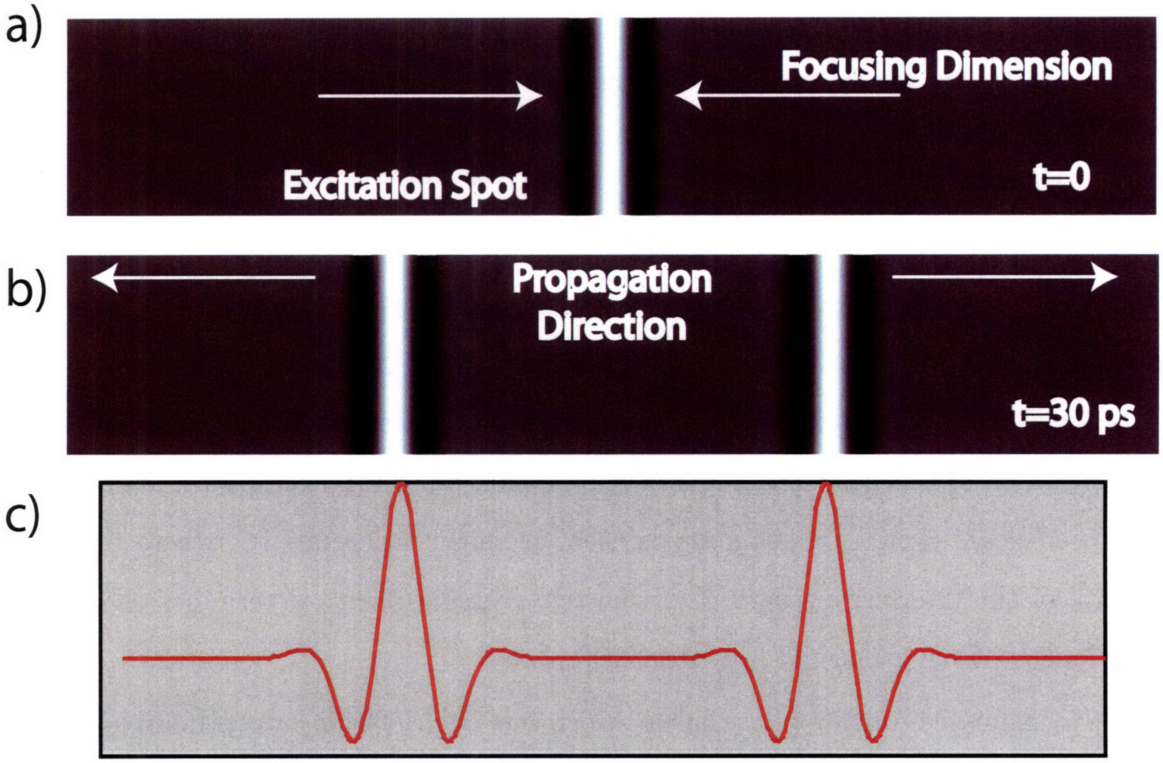
a)
Focusing Dimension
Excitation Spot
t=0
b)
Propagation
Direction
t=30 ps
c)

Figure 4-3: Schematic illustration of broadband phonon-polariton wavepacket, generated by a cylindrically focused 'line' of light (a), which propagates laterally on a picosecond time-scale (b). Vertically integrating these 2D images yields the polariton field profile, (c) as a function of the lateral dimension only.

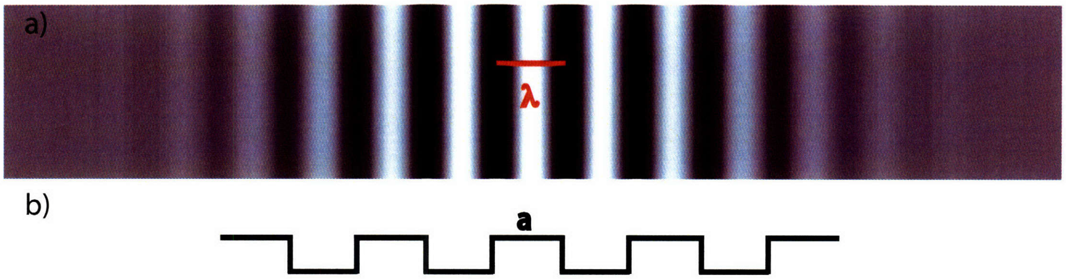

Figure 4-4: Schematic illustration of a narrowband excitation region, indicating the transverse wavelength λ of the generated 8 cycle pulse (a), and the profile of the binary transmission grating (b) used to generate this pattern, when imaged with a 1:1 cylindrical telescope onto the sample, with all diffractive orders other than ± 1 blocked.

4.2.2 Narrowband Generation

Although broadband measurements are often ideal for studying the behavior of polaritonic structures, the limited intensity of any given frequency component makes it difficult to do fine-grained quantatitatve measurements. When more narrowband waves, which in this case means 5-50 cycle phonon-polariton excitations, are desired, a crossed-beam excitation geometry is used, as shown in Figure 4-1, where the periodicity of the interference pattern of the two crossing beams determines the center wavelength of the generated polariton wavepacket.

A transmissive binary phase mask which has been designed to primarly diffract into the ± 1 orders of diffraction is used to split the incident beam into two beams to be crossed at the sample. All orders other than ± 1 are blocked, and the ± 1 orders are imaged using a 1:1 cylindrical telescope onto the crystal. This geometry produces a sinusoidal interference pattern with $\lambda_{\text{center}} = a$, where a is the feature size of the binary phase mask (and thus half its period), as shown in Figure 4-4.

4.2.3 Cherenkov Cone

When considering polariton excitation as the pump pulse travels through a thick piece of LN, it is important to consider that the pump is only acting on a small region (in

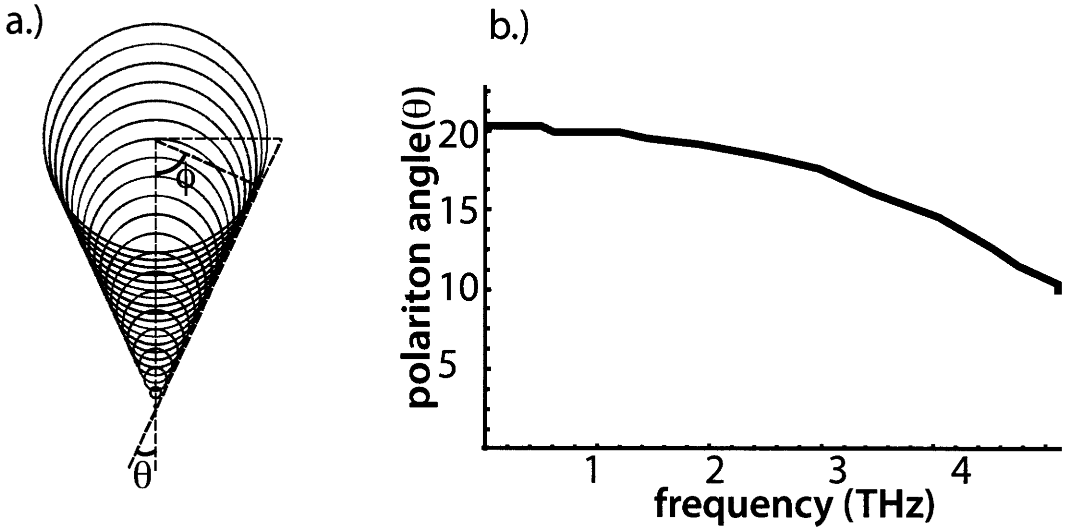

Figure 4-5: Considering the polariton pump as a sequence of point source excitations yields the boat-wake-like Cherenkov cone excitation (a), where the angle is determined by the ratio of polariton phase velocity and pump pulse group velocity inside the LN crystal. Because the phase velocity of THz radiation changes significantly, the cone angle changes significantly for lower branch polaritons in the 0-5 THz regime.

the depth) of the crystal at any given instant in time; a 50 fs pump pulse is only 6.5 microns long inside the crystal. Because of this, pumping occurs at the input face of the crystal before it happens at the output face. Since the pump pulse travels through the crystal signifcantly faster than the generated THz radiation (125 $\mu m/ps$ for 800 nm, 50 $\mu m/ps$ for THz), this produces a Cherenkov cone as shown in Figure 4-5[1]. The angle between the generated THz response and the pump θ, and the corresponding polariton forward component, ϕ, is given by,

$$\theta = \sin^{-1}\left(\frac{v_p^{\mathrm{pol}}}{v_g^{\mathrm{pump}}}\right) \tag{4.2}$$

$$\phi = \cos^{-1}\left(\frac{v_p^{\mathrm{pol}}}{v_g^{\mathrm{pump}}}\right), \tag{4.3}$$

where v_p^{pol} is the polariton phase velocity, and v_g^{pump} the pump group velocity. For low frequency (below 1 THz) phonon-polaritons, $\phi \approx 26°$

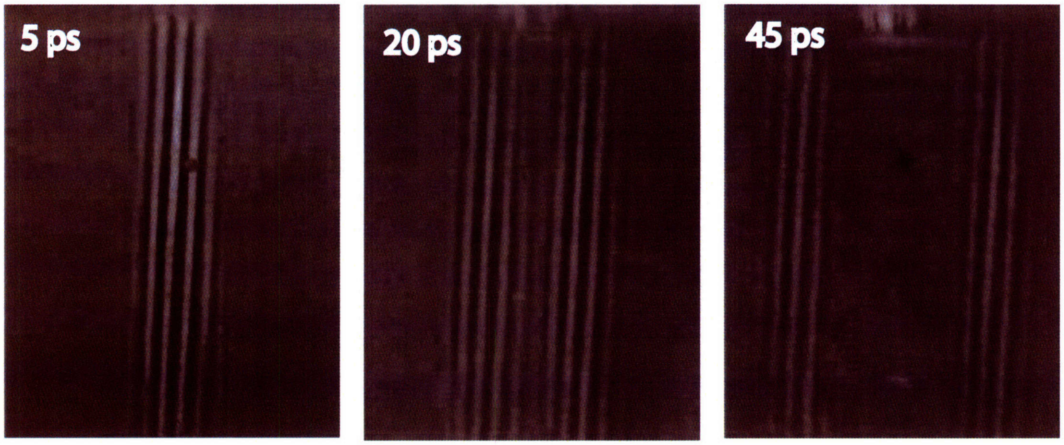

Figure 4-6: Propagation of a 7-cycle polariton wavepacket over a 45 *ps* period. ISRS of crossed 800 nm pulses, generates two counter-propagating polariton wavepackets, which travel away from the generation region at roughly 50 μm/ps.

4.3 Polariton Detection

All polariton signals in this thesis were recorded using variants of real-space imaging, wherein the polariton excitation within a sample crystal was monitored throughout the entire crystal all at once [32, 33, 16]. Other methods of monitoring polaritons at single points such as optical Kerr effect (OKE), terahertz field induced second harmonic generation (TFISH), and wavelength shifting can yield higher signal to noise at a single point than imaging based techniques[59, 57, 7], but real-space imaging allows selective filtering based on the spatial Fourier components of each time slice (image).

4.3.1 Real-space Imaging

With real-space imaging, the intent is to monitor the entire polariton excitation profile inside the crystal at all spatial points for a given time-step, in essence, to collect a ‘real space’ image of the polariton fields at a given instant in time, and then to repeat that measurement at many different time-steps to produce a three dimensional data set (one temporal, two spatial), which can be represented as a movie showing polariton propagation. See Figure 4-6.

It is important to note that the polariton images at each time step are merely two dimensional projections of three dimensional fields, with signals dependent on the quality of velocity matching between the propagating THz phonon polariton phase velocity, and the probe beam group velocity. Using a probe beam of the same wavelength as the initial generation beam, and of the same propagation direction, should guarantee matching between the initially generated phonon polariton and the probe pulse, since by virtue of the generation mechanism, the THz fields generated by the pump are matched to the pump group velocity in the sample, as described in Section 3.8. Since the pump pulse that generates the polaritons moves from the front to the back of the crystal at the same speed as the probe pulse that monitors them, phase matching for monitoring of the initial response is assured.

Unfortunately, having a strong pump and weak probe coincident on a sample and of the same wavelength renders it impossible to prevent excessive pump light from reaching the detector, overwhelming the polariton images, and likely damaging the detector. To allow the filtering out of pump light, a different wavelength of probe light is used, in this case 400 nm. Although 400 nm light is easy to produce through SHG in a BBO crystal, it is non-ideal because of the distinctly different indicies of refraction for 800 nm and 400 nm light within $LiNbO_3$ (n_e of 2.18 and 2.33 respectively), and to properly match the probe group velocity to the THz phase velocity requires a probe incidence angle of roughly 10° away from normal, which allows velocity matching to the polariton wave travelling laterally in the same direction as the probe. The THz response that propagates in the other lateral direction is not optimally phasematched. A separate phase-matching issue arises because of the forward propagation component of the polaritons. The probing process is phase-matched while they are propagating forward, but after they reach the back of the crystal, undergo total internal reflection, and move from the back towards the front crystal face, the probing is no longer phase-matched. For some crystal thicknesses ($\sim 1/2$ mm) multiple polariton reflections off the back and front faces occur, giving rise to alternately stronger and weaker signals as the probe phase-matching condition is alternately met and not met [59, 52, 16].

4.3.2 Space Time Plots

The typical phonon-polariton experiment, where signals are uniform along the optic axis of the crystal, and thus only exhibit interesting dynamics in one spatial dimension and time, can be described by those two dimensions. To produce this two-dimensional representation from the three-dimensional data-set produced by real-space imaging, integration is performed across the invariant dimension (the vertical dimension in the images shown in this thesis), producing a two-dimensional data set with significantly better signal to noise, since the integration is effectively averaging across the signals that were recorded by the CCD camera along the integration dimension.

These two-dimensional representations, referred to as space-time plots, are conducive to the easy visualization of wave propagation properties such as group velocity and phase velocity. Performing a two dimensional fourier transform on a space-time plot directly yields the experimental dispersion relation of the system, and allows the filtering out of noise at many wavevectors and frequencies.

4.4 Bulk Polariton Dispersion

Using both narrowband and broadband excitations, and correcting for the polariton forward component due to the Cherenkov cone, it is possible to map out the lower polariton branch, and to see the presence of the upper branch. Figure 4-7 uses narrowband measurements of the high-k parts of the dispersion curve, corresponding to grating periodicities of 6-75 μm, and broadband measurements to access longer wavelength responses of the lower branch and to see the upper branch. The upper polariton branch is only visible in broadband measurements, because its weak signal is only observable after the lower branch polariton has propagated away.

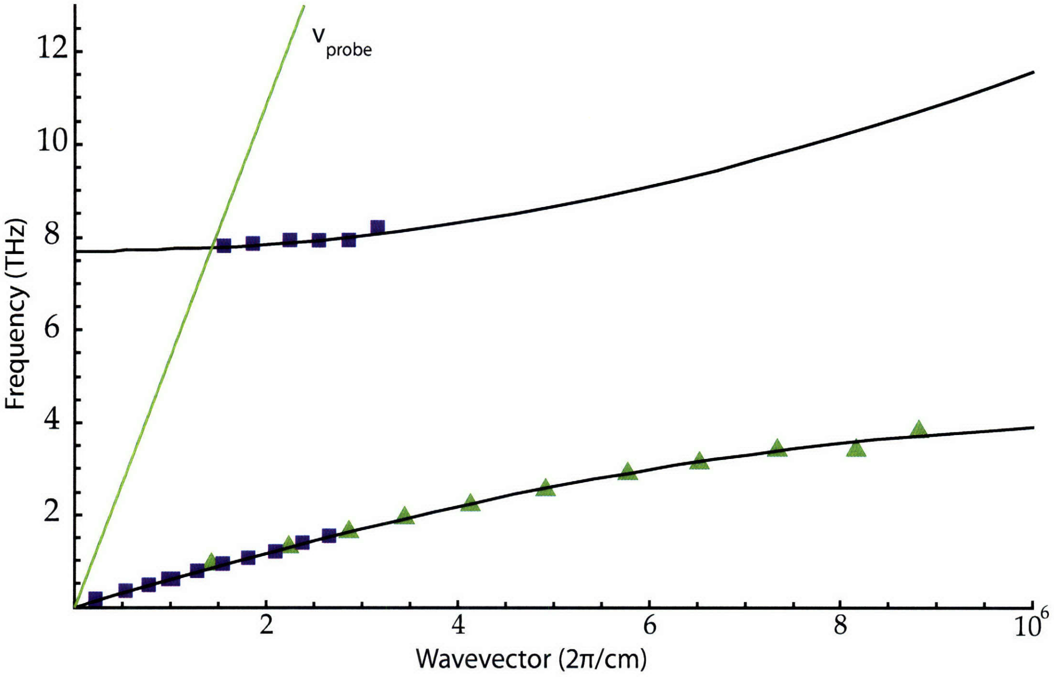

Figure 4-7: Experimental bulk dispersion relation of stoichiometric LN compiled from both broadband (squares) and narrowband (triangles) measurements. The upper branch polaritons are only evident in broadband measurements because they are dominated by the lower branch signal until the lower branch signal has propagated away from them, which by which time they have damped away for narrowband measurements.

4.5 Polaritons in Bulk Crystals

Polariton propagation in bulk ferroelectric crystals allows the driving and detection of relatively strong THz electromagnetic fields. By shaping the input optical pump pulse, arbitrary polariton waveforms can be generated, and through careful phase-matching of a probe pulse to the generated phonon polaritons, their propagation can be observed. Correction for the forward angle of propagation due to the cherenkov cone allows the mapping of both the lower and upper branches of dispersion within the bulk crystals studied.

Although thick crystals allow the creation of large total-energy THz pulses, and the detection of small responses due to the volume-integrated nature of both pumping and probing, the importance of phase-matching on both pumping and probing makes thick crystals less than ideal for quantitative measurements. Polariton images from thin samples will be presented in subsequent chapters of this thesis.

Chapter 5

Confinement in One Dimension

This work produced in collaboration with David W. Ward and Christopher Werley of the Massachusetts Institute of Technology, and Ryan Roth and Richard Osgood of Columbia University.

When considering the effects of confinement on polariton generation and response, we start with the simplest case– confinement in one dimension. As a crystal becomes thin relative to the polariton wavelength inside the crystal, the effects of reflection off of the front and back faces of the crystal become dominant; phonon-polaritons no longer propagate at their normal bulk crystal velocity (50 $\mu m/ps$), instead travelling at a speed much closer to propagation rates in air.

With the confinement dimension to be into the depth of a crystal, the system under nomal experimental conditions (x-cut crystal, pump and probe polarized along the optic axis) is described as a slab waveguide with primarily transverse electric (TE) modes: two electric field components, both parallel to the pseudo-infinite dimensions of the slab.

In the sufficiently thin limit, in which all the interesting confinement effects on propagation are evident, the phase-matching condition on probing is relaxed since any differences in the propagation times for pump and probe pulses through the thin crystal are negligible. This reduced velocity matching consideration allows us to direct the probe light through the crystal parallel to the pump light or at any convenient angle. The preferential detection of one polariton propagation over the other direction is no longer a problem, vastly simplifying both experiment and simulation.

The alternating forward and backward polariton propagation components in bulk crystals leave their mark in thin films, where spatial overlap and interference among the multiply reflected waves leads to multiple waveguide modes having different numbers of nodes in the depth of the crystal. What in bulk is described in terms of forward and backward wavevector components, now has to be expressed as a sum of the eigenmodes of the system, and there will typically be significant amplitude in the lowest 2-4 slab waveguide modes.

5.1 Narrowband excitation of LN slabs

Narrowband, 10-50 cycle radiation was generated in 10 micron thick LN slabs, that were fabricated by Crystal Ion Slicing (CIS) as described below. An 800 nm pump in a crossed excitation-beam narrowband geometry excited the TE modes of the freestanding film, and polariton propagation was observed using 400 nm real-space imaging. The experiment was repeated for 18 different propagation constants (grating periods) ranging from 10-100 microns.

5.1.1 Crystal Ion Slicing Slab Fabrication

Congruent x-cut crystals of LN were implanted with He$^+$ ions at an energy of 3.8 MeV and an ion dosage of 2 x $10^1$6 ions/cm^2, by using an ion gun. Implantation under these conditions generates a relatively intact crystal surface region, from the surface down to a depth of 10 μm, and then a 1 μm thick damaged region where the He ions preferentially deposit. The location of this damaged region is determined by the energy of the incident He$^+$ atoms, and the level of damage on the dosage[37, 45, 46].

The samples were cut into 4 mm x 4 mm blocks, cleaned, and the patterned side bonded to a Si wafer. Electrostatic bonding to the Si wafer was accomplished by heating to 100 °C for at least 20 minutes. The heating generated a pyroelectric

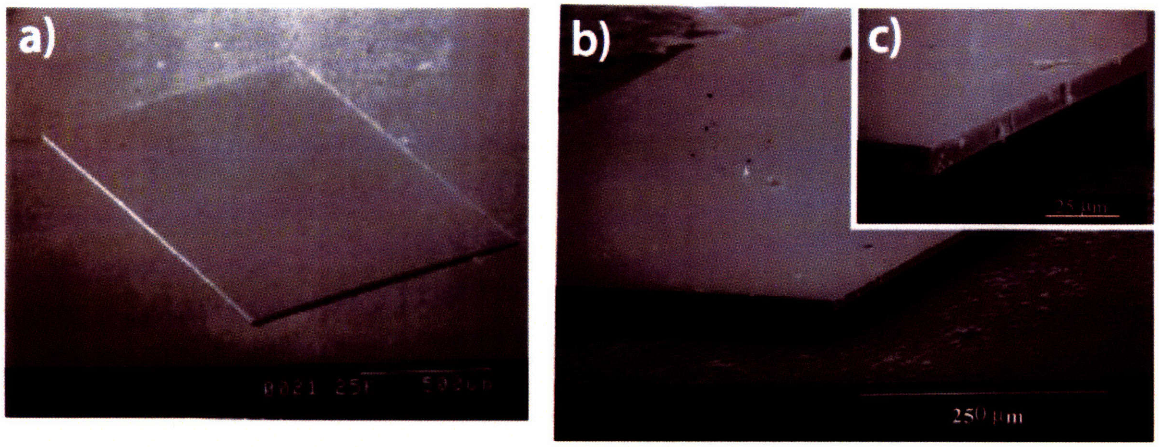

Figure 5-1: Electron micrograph of 10 micron LN slabs produced by Crystal Ion Slicing.

charge in the LN, which held the sample to the SiO_2 layer on the surface of the Si wafer.

Exfoliation, the splitting of the LN crystal along the damaged region, was achieved through thermal snapoff. The coupled LN-Si system was heated to 500 °C for 5 seconds, causing fracturing of the crystal in the region damaged by the implanted He ions, thus freeing the surface film from the substrate LN crystal.

The film was decoupled from the Si wafer by wetting with a drop of methanol, yielding a freestanding 10 μm film of LN, with large (>1 mm) transverse dimensions, as shown in Figure 5-1.

These thin film samples were fabricated and provided by Ryan Roth and Richard Osgood of Columbia University.

5.1.2 Dispersion

Thin crystals of LN generated through CIS were believed to remain single domain, and to maintain the properties of the substrate crystal from which they were segmented, and this behavior had been checked for short range interactions by looking at SHG of 800 nm light by the crystals both before and after segmentation[37, 45, 46]. The question remained whether the cracking pattern, illustrated in Figure 5-2, was

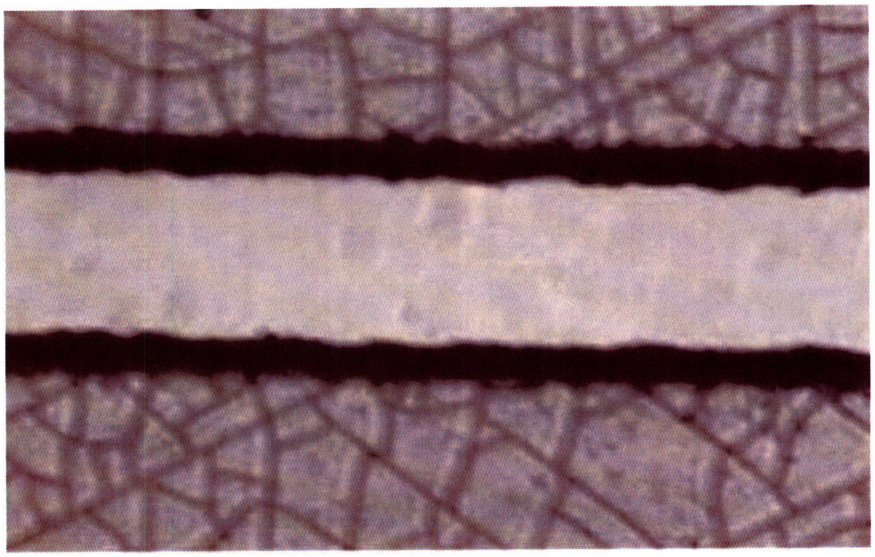

Figure 5-2: Visible light micrograph of a 10 micron LN slab produced by Crystal Ion Slicing. The large slot is a 6 micron width trench produced in the slab using femtosecond laser machining.

evident of domain flipping or other changes to longer-range order of the originally single-domain crystal. Measurement of the THz dispersion relation of the thin films, and comparison to theoretically determined dispersion for crystals of this thickness, indicates the high quality and single domain nature of the slabs.

The LN slab was mounted so that in the region of interest it was free standing, yielding a dielectric slab waveguide with symmetric boundary conditions as treated in Section 2.3. The relatively low optical quality of the thin films, and their extreme thinness, yielded relatively weak polariton responses as measured through polariton imaging, so to produce maximal signal at each frequency of interest, a narrowband phonon polariton generation method was used.

Narrowband, 10-50 cycle THz polariton waves were generated using the crossed beam geometry described in Chapter 4, and was repeated with transverse wavelengths ranging from 6 to 100 μm, corresponding to wavevectors ranging from 10,000 to 600 cm^{-1}. The number of cycles was determined by maintaining a constant 1 mm (wide) x 600 μm (high) spot size on the sample.

Phonon-polariton fields were probed using real-space imaging, some results of

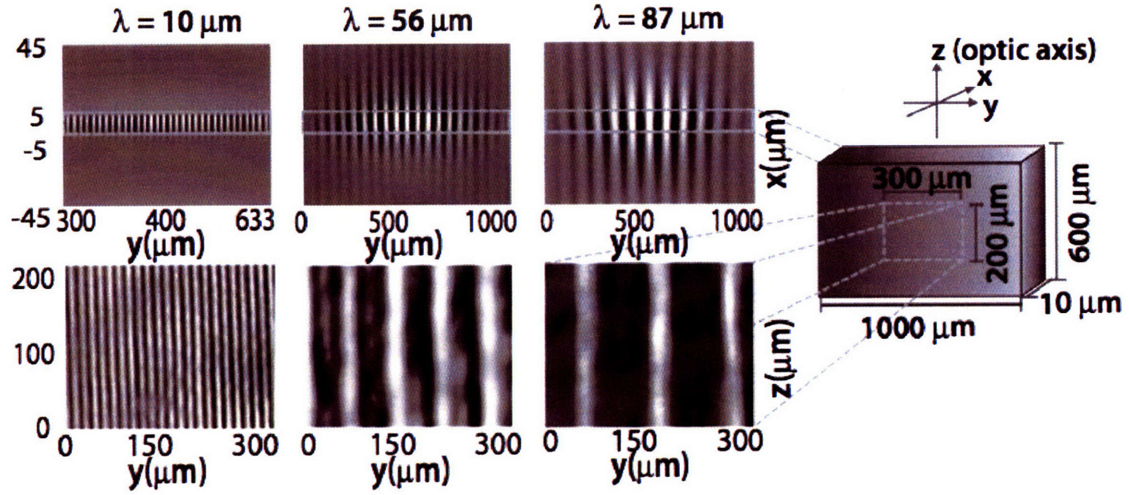

Figure 5-3: Sample geometry of the 10 μm slab waveguide experiment. The lower set of images are experimental images of the narrowband polariton excitations for three different excitation wave-vectors. The upper set of images are the amplitude of E_z from 2D TM FDTD simulations of the fields in the depth of the slabs, under the same excitation conditions.

which are shown in Figure 5-3. The spatial scale was determined by using a calibration image, and the temporal scale was determined by the mechanical delay stage. The nature of the excitation in the depth of the crystal was investigated using 2D FDTD simulation of generation and propagation.

When considering bulk crystals, it was nessecary to convert the transient grating wavelength, λ_g, imposed by the crossed pulses to the actual polariton wavelength, λ_{pol}, by considering the Cherenkov cone angle since polariton propagation included a forward as well as lateral component. Although this is still true in the slab waveguide case (the polariton wavelength is not equal to the imposed wavelength), the imposed wavevector is actually the more useful metric of the propagating mode's properties. In the parlance of waveguides, what we refer to as k_x is the propagation constant (β) of the waveguide excitation, and the dispersion relations of all the waveguide modes are plotted as a function of it, as shown in Figure 5-4.

Because of the low signal levels in the 10 micron films, and narrowband excitation, it was difficult to detect the higher order waveguide modes of the waveguide.

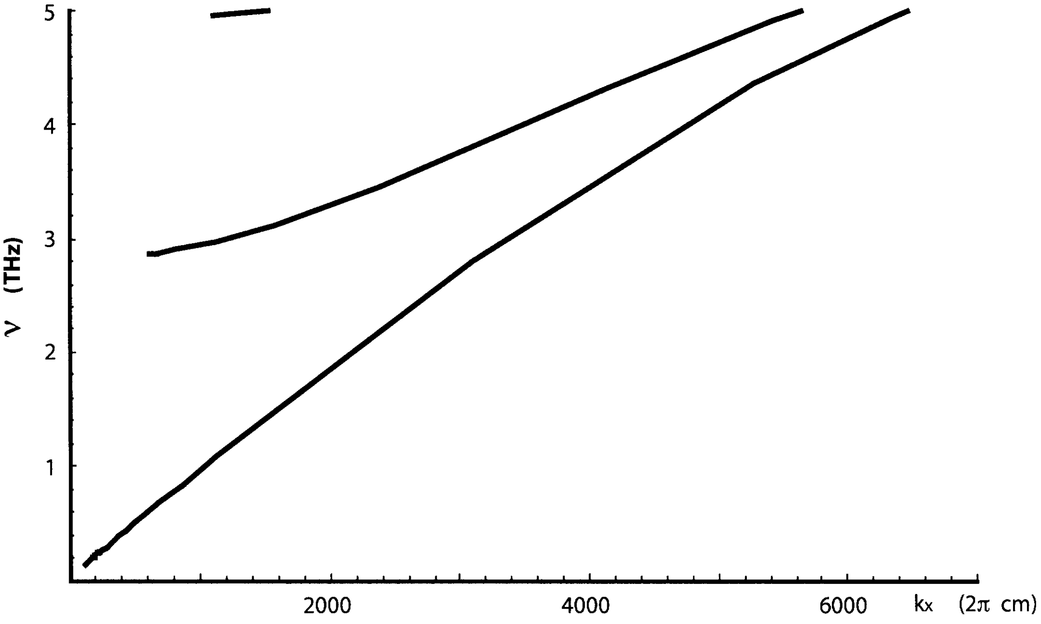

Figure 5-4: Theoretical dispersion curves of 10 μm thick LN slabs, determined using the solutions of a dielectric slab waveguide. The x axis, k_x, corresponds to the imposed grating wavevector of the experiment, which gives the periodicity of the excitation in the direction of propagation.

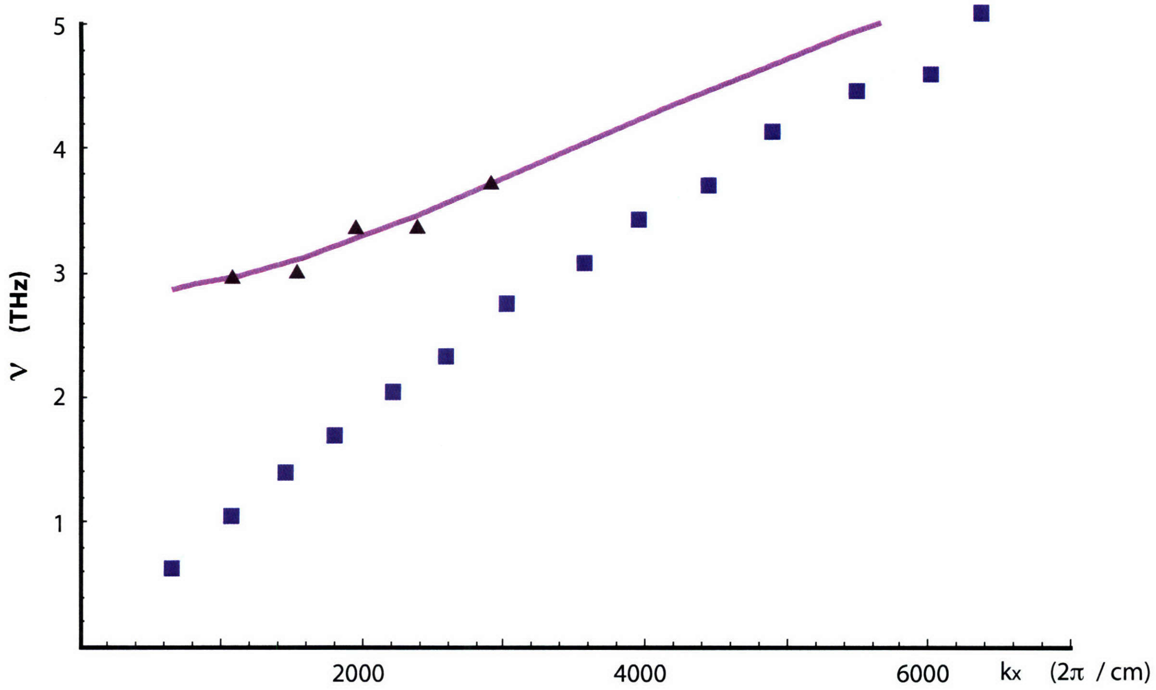

Figure 5-5: Experimental Dispersion relation of the CIS fabricated 10 μm LN slabs. The points indicate the experimental values determined to belong to the two lowest waveguide modes, and the lines are the theoretical dispersion relations of those two modes.

The dispersion relation for the lowest order modes for both experiment and FDTD simulation yields Figure 5-5.

5.2 Broadband excitation of LN

Although the narrowband study of the lowest frequency waveguide mode the thin LN slabs in the previous section shows the strength of the method, any higher order waveguide modes are undetectable, partially because in the absence of lateral spatial separation of the modes due to differing propagation velocities, the low signal levels from the very thin crystals render the higher-order modes undetectable.

To combat these effects, broadband phonon-polariton wavepackets were generated in 34 and 50 μm thick crystals, of much higher optical quality, which were commercially obtained. These thicker crystals were fabricated by cutting and polishing of bulk LN crystals, and thus do not have the optical defects that plagued real-space imaging in the 10 μm films. Using real-space imaging, the wavepacket evolution was recorded for each crystal. The single-cycle broadband excitation wavepacket that was produced had a central wavelength of $\tilde{1}00$ μm.

The resultant data sets were vertically integrated to produce space-time plots, and fourier-filtered using a band pass filter in both frequency and wave vector, as shown in Figure 5-6. The space-time plots show the excited wavepackets propagating away from the generation region in both lateral directions. The wavepackets are superpositions of several planar waveguide modes that separate spatially after a short time due to their differing group velocities.

The dispersion relations resulting from Fourier transformation of the space-time plots in both dimensions are shown in the right-hand plots of Figure 5-6. Several trends, consistent generally with waveguide theory, are apparent from the results: the frequency gap between distinct waveguide modes decreases with an increase in film thickness, the number of modes accessible within the wavevector range generated increases with crystal thickness, the group velocity becomes progressively smaller for higher order modes, and the phase velocities are faster than those of the bulk LN crystal. In the 34 μm thick film, the effective indices of refraction are 3.0 for the lowest-order mode (m = 0) and 1.5 for the second mode (m = 1). In the 50 μm thick film, the values are 4.0, 2.0, and 1.2 for the three modes m = 0, 1, and 2 respectively. The expected dispersion relationships of the two dielectric slabs are shown in Figure 5-7.

Especially evident in the fourier transforms in Figure 5-6, the horizontal gaps at approximately 450 cm^{-1} are due to artifacts of Talbot imaging, as described in Section 3.9.1.

5.3 Selective Driving of Multiple Modes

Qualitative analysis of the modes excited, as shown in Figure 5-6, shows that higher frequency (and thus higher order) modes are more weakly excited than the lowest

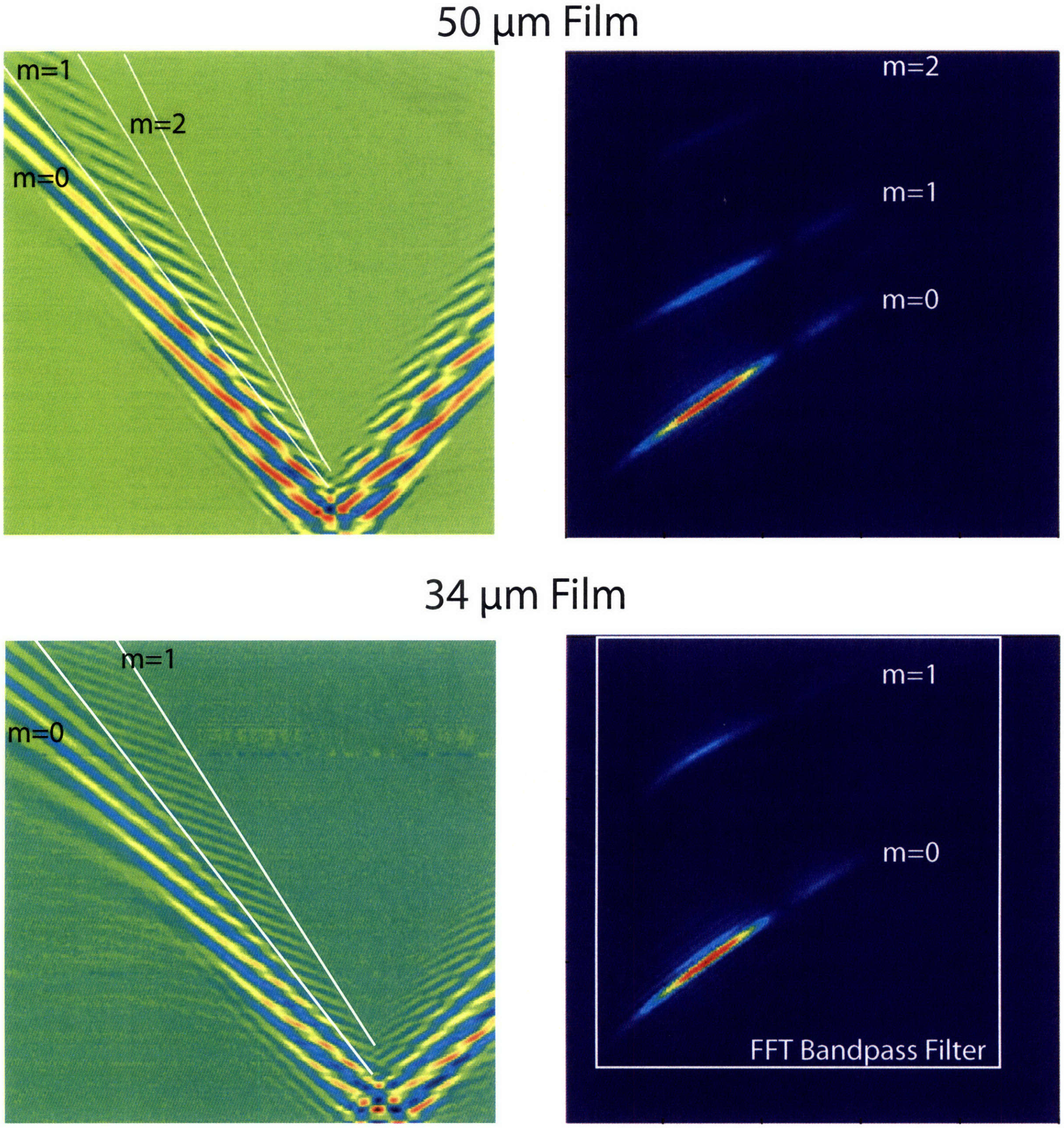

Figure 5-6: Broadband phonon polariton propagation in $50\mu m$ and 34 μm thick LN films. The left-hand figures show space-time plots of the propagation. The excitation beam reached the crystals at the zero of the time axes and at a location of about 2 mm on the position axes shown. The multiple modes of the waveguide separate spatially as they propagate, due to differing group velocities. The bandpass filter used to clean the raw data is shown on the 50 μm slab Fourier transform.

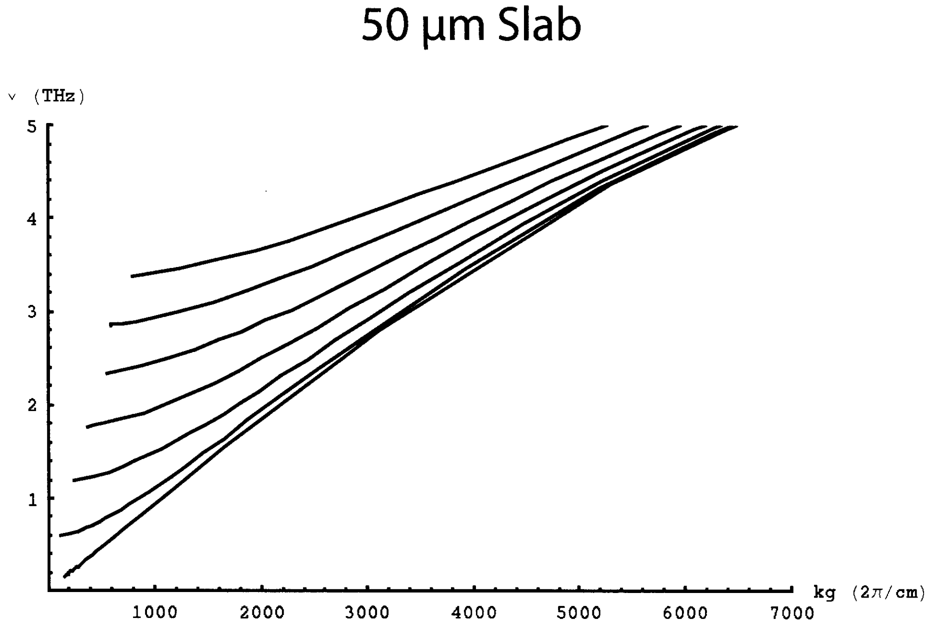

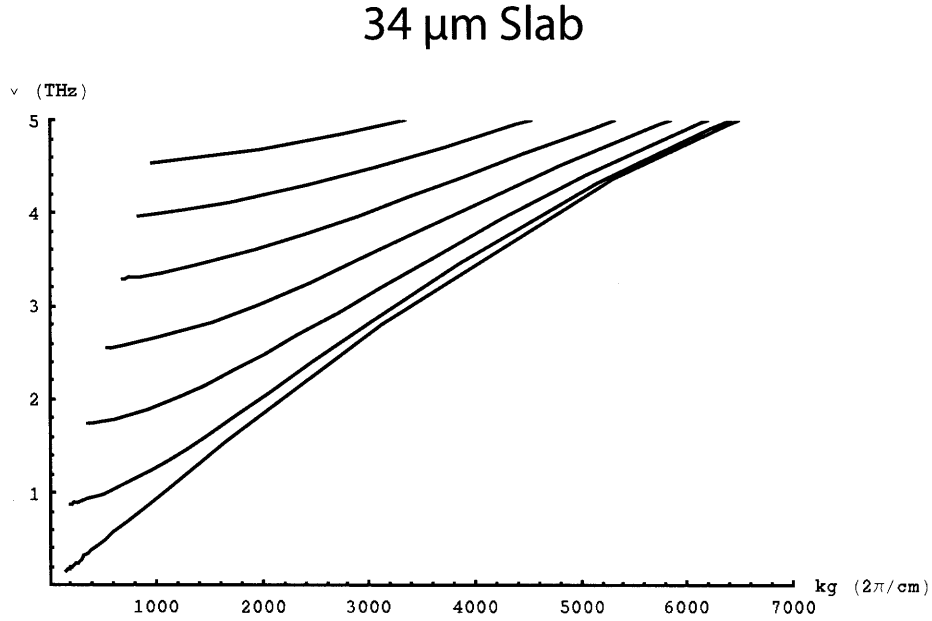

Figure 5-7: Theoretical dispersion curves for 34 *μm* and 50 *μm* LN slabs, with the lowest 7 waveguide modes indicated. The low-wavevector bound of each mode is where it intersects the light line of radiation propagating in the cladding (in this case air), and at high wavevectors all modes asymptote to the bulk dispersion relation of LN.

order mode, but the intensities of excitation are not directly related to the frequency of the mode. To first order, we can write the intensity of mode excitation as proportional to the projection of the bulk polariton Cherenkov cone angle onto the eigenmodes of the slab waveguide. Taking the slab waveguide modes to be of the form,

$$\psi_m = A_m \sin\left(k_m y + \phi_m\right), \tag{5.1}$$

defined only inside the waveguide, with $m = 0...a$, and a broadband excitation with a cherenkov cone of angle θ given by,

$$\begin{aligned} r_p &= \left[\hat{x}\cos\theta + \hat{y}\sin\theta\right] && (5.2) \\ \psi_p &= e^{\frac{(r_p - r_0)^2}{2\sigma}}, && (5.3) \end{aligned}$$

where r_0 is the pump position. The relative excitation strength, B of any given mode m by a broadband, single cycle excitation spot, is given by,

$$B_m = \int_0^a dy \psi_m \psi_p, \tag{5.4}$$

in the limit of very short (sub polariton period) excitation pulses. The values calculated through this method are roughly correct (within 20% of simulated), but for direct comparison to experiment, 2D FDTD simulations were performed. For a 50 fs, 100 μm FWHM pump pulse traveling through various thickness films, the excitation intensities are summarized in Figure 5-8.

5.4 Detection Efficiencies of Differing Modes

The velocity matching considerations of polariton detection within bulk crystals require that the probe group velocity match the polariton phase velocity as they both travel through the crystal, resulting in a roughly 10 degree offset angle for blue light

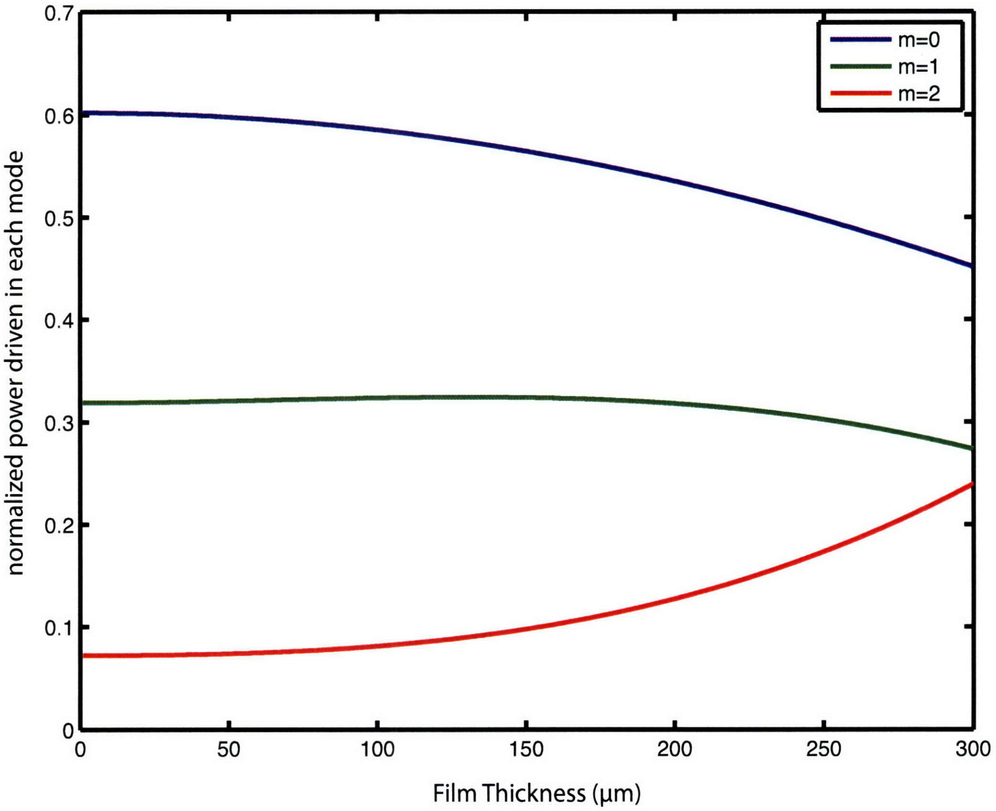

Figure 5-8: Relative driving strengths of the lowest 3 modes of a slab waveguide as a function of slab thickness, by a 50 fs, 100 μm FWHM pump pulse. Results were generated using 2D TM geometry FDTD simulations. Normalized experimental driving strengths are indicated.

probing as described in Chapter 4. As previously mentioned, for these thin films this is no longer a strong consideration, as the polariton phase fronts barely move in the amount of time it takes the probe pulse to traverse the thickness of the slab (300 fs for the 50 micron slab). Thus, for thin crystals we use a normal probing geometry, and accept the slight degradation in signal due to the non-perfect 'velocity' matching.

This approximate method works well for the lowest order slab waveguide mode, as it is isotropic in the depth of the crystal, but has difficulties when used to detect higher order modes, as they have multiple lobes of differing field sign along the direction of probe propagation. The relative probe errors as determined by 2D FDTD simulation, are summarized in Figure 5-9. One important thing to note, is that in practice, polariton experiments in relatively thick >100 μm slabs typically entail the excitation of ten or more waveguide modes, and the overall detection efficiency of the excitation is given by a weighted average of all the modes which comprise the excitation.

The errors due to this poor phase matching are relatively constant as a function of frequency, primarily depending only on waveguide thickness and mode order, thus allowing direct comparison of differing frequency components of the same mode. For the lowest order mode, the signal is approximately 85% of what would be detected by an infinite velocity probe pulse.

5.5 Data Filtering though 2D Fourier Transforms

Shot-to-shot noise and pointing instabilities in the pump laser result in significant (primarily temporal)noise in space time plots, which needs to be filtered out to allow for quantitative analysis. Additionally, pump and probe scattering due to crystal imperfections, dirty samples and optics, and machined structures also introduce noise, primarily in the spatial dimension. Two general methods of filtering have been used, the aforementioned bandpass filtering in both wavevector and frequency, and an adaptive filter which takes into account the specific character of the dispersion curves of slab wave guides.

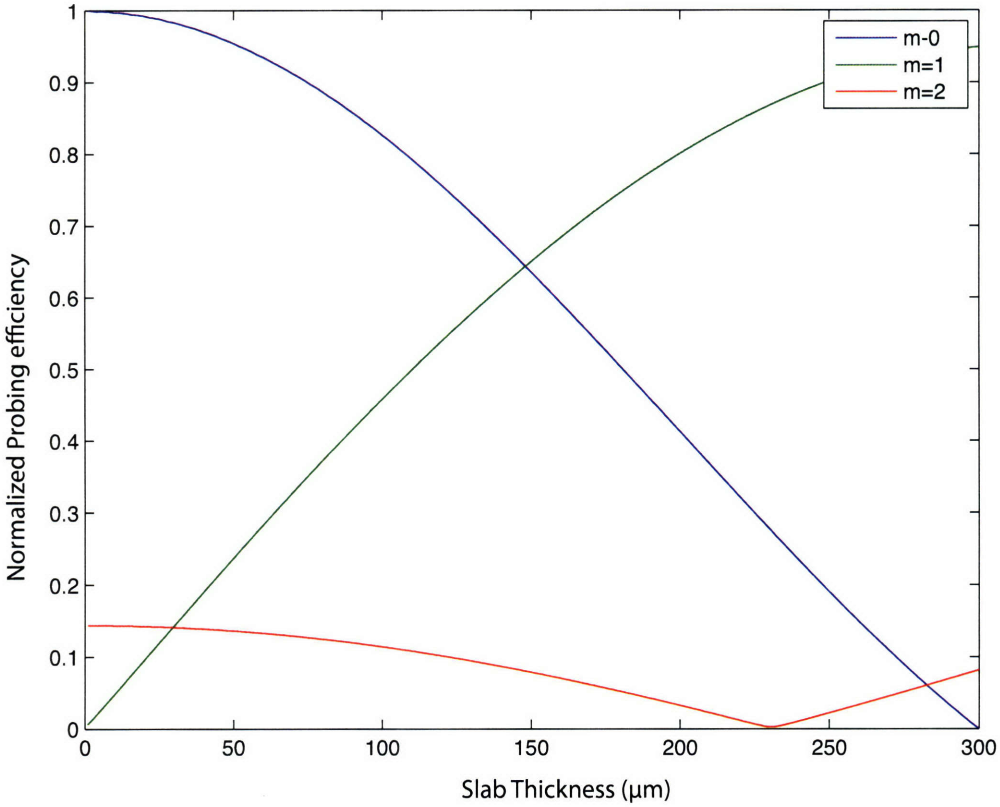

Figure 5-9: Relative detection strengths of the lowest 3 modes of a slab waveguide as a function of slab thickness, by a 50 fs probe pulse. Results were generated using 2D TM geometry FDTD simulations.

5.5.1 Bandpass filtering

The goal of bandpass filtering is to remove three sources of noise: slow fluctuations (on the time period of tens of minutes) in laser output, shot-to-shot and pointing instabilities that produce strong differences between sequential time-steps, and pump scatter off of crystal imperfections.

In a space time plot, the first two of these errors occurs at very long and very short time scales, and thus can be significantly reduced by filtering out the low and high temporal frequency fourier components. Additionally, pointing instability and long term laser intensity modulations typically affect most of the image at the same time, so filtering out low-wavevector signals also serves to reduce their impact.

Pump scatter, although primarily dealt with through spectral filtering and experimental geometry, can also be partially compensated for by filtering out high wavevector components of the space-time plot. Pump scatter artifacts typically will appear as interference patterns with wavelengths of 2-10 microns, and especially when probing long wavelength polaritons in the 50-200 micron regime, these can be filtered away.

5.5.2 Intelligent filtering

Slab waveguide dispersion exhibits several notable features. The lowest order mode has no cut off, and will intercept the origin of frequency and wavevector. All higher modes intercept the light line corresponding to light propagating in the cladding (in most cases this is air, and the speed can be assumed to be c_0), and each mode is monotonic in wavevector.

Thus, we can perform two filtering options on the dataset. All points within the light cone of the cladding, which would suggest propagation at faster than the speed of light in air, can be discarded. This has the advantage of throwing away all the low wavevector components that were advantageous to discard in the bandpass filtering case, and also allows discarding higher wavevectors at higher frequencies, improving the effectiveness of the filtering.

A stronger, more risky, filtering can be performed if we can identify the modes within the unfiltered data set. Typically, large portions of the modes have relatively strong signals, and they can be isolated using thresholding: setting all data points inside the 2D array which have values less than half the median value to 0. Splitting the dispersion relation into different modes by inspection, then fitting each mode with a polynomial fit, all data within a 'distance' $\delta \approx 2 - 10$ data points of a fit line can be retained, with all other parts of the array discarded. One important check against this method is to check the phase terms of the 2D fft. Noise will typically have random phase, and valid data will have some sort of smooth phase progression, with the only 'noise' due to phase wrapping.

5.6 Slab Waveguides as Detectors

The strong dependences of slab waveguide dispersion on both crystal thickness and material properties has been considered. The observation of multiple waveguide modes, especially when separated from each other using both wavevector and frequency provides a useful measure of both material properties and slab thickness.

The well behaved nature of radiation propagating through slabs allows for the direct calculation and measuring of driving and detection efficiencies, with any given mode in a specific waveguide having directly calculable values for these efficiencies which unlike in the bulk case do not change over the course of propagation. This reduced detection experimental complexity makes slab waveguides prime candidates for quantitative measurements of polariton fields.

Chapter 6

Confinement in two dimensions

Introducing a second dimension of confinement, the z direction (vertical in the images shown here), yields the rectangular waveguide regime. Now there are two orthogonal eigenvalues for the system, corresponding to confinement in the y and z dimensions.

Qualitatively, pumping and probing in these thin square waveguides is identical to the case of the slab waveguide. As in that case, what in bulk is described as a forward wavevector component has to be expressed as a sum of the eigenmodes of the system. As the pump intensity profile is always very uniform in the z dimension, it is reasonable to assume that over the height of these small waveguides driving force on the polaritons is uniform. It follows that only the modes of even symmetry in z are driven with any significance. The modes driven in y resemble those of the slab waveguide considered in chapter 5.

6.1 Femtosecond laser machining

To introduce structure into transverse dimensions of a LN crystal requires some method of chemically or mechanically patterning the crystal, starting from the polished slabs considered in the previous section. Typically, when patterning wafers is required, it is advantageous to take advantage of the massive capabilities of photolithography. For ferroelectric crystals, it is possible to do wet etching[61], but the

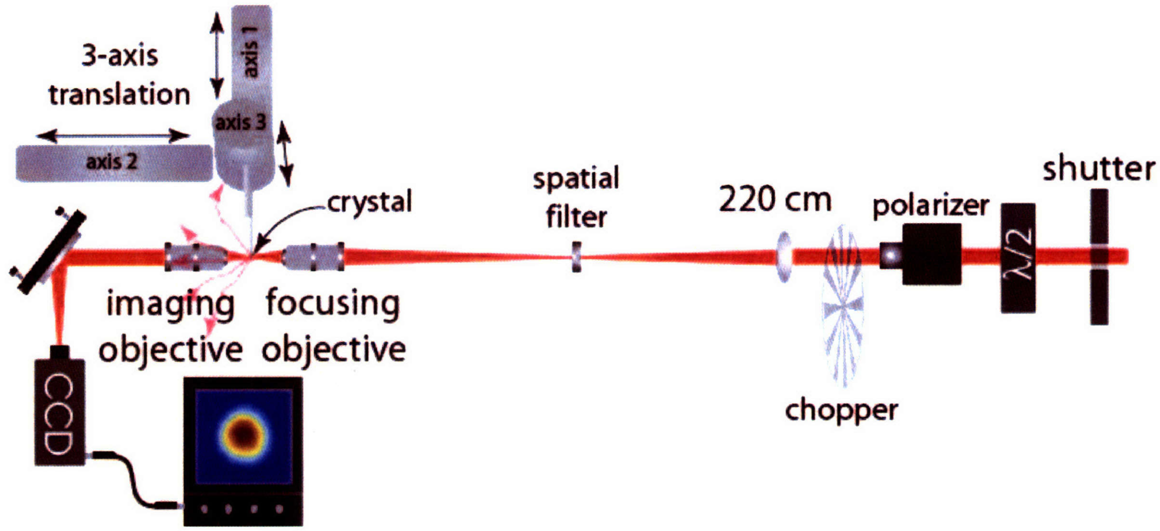

Figure 6-1: Femtosecond laser machining apparatus. The substrate to be patterned is positioned within the beam focus using a computer-controlled 3D linear stage, and machining is executed by using a computer-controlled shutter to allow the intense pulses to reach the sample only at specified locations. The chopper reduces the laser repetition rate to 500 Hz in order to separate successive pulses by a time period that is longer than the 1 ms response time of the shutter.

extreme conditions required, for example etching in 80 °C hydrofluoric acid, and preferential etching along non-desirable crystalline axes[5], means that other methods are preferable.

Ultraviolet and sub-bandgap laser ablation have been used for surface patterning of waveguids in LN with good success, but the high fluences required cause significant heating-related damage to the crystal in the area surrounding the patterning[8, 39]. Femtosecond laser machining allows patterning without significant unintentional damage to the surrounding crystal[20, 48, 60].

The femtosecond laser maching setup is depicted in Figure 6-1. Roughly 100 μJ, 100 fs, 800 nm pulses are focused to a spot size of 10 microns through a N/A 0.1 microscope objective. The laser intensity is modulated by a computer-controlled shutter, and the substrate to be patterned is moved around in the focus by using a computer-controlled 3D linear translation stage.

For the sake of repeatability, the crystal is only moved when the shutter is closed to block the laser beam. The crystal is moved to a location where a hole is to be drilled into the substrate crystal, then the shutter is opened for an exposure time varying from 0.1-3 seconds, depending on crystal thickness and desired hole diameter. The shutter is then closed, the crystal moved, and the process repeated for the next hole.

To achieve linear cuts, for example the boundaries of the waveguides considered in this section, the same method is used, but the distance between sequential holes is set to roughly 10% of the machined hole diameter, and for additional smoothness, the cut is performed over the course of 3-5 passes, each pass of machining penetrating a bit further into the crystal. Machining in this iterative manner also serves to minimize the stresses on the crystal, allowing the production of fine structures with a reasonably low chance of breakage.

6.2 Single square waveguides

Unlike in the slab waveguide case, where measured k_x and ω yield complete characterization of the modes driven, adding confinement in the vertical dimension means we now have to consider which eigenmode the k_x, ω pair corresponds to. Once again, polariton imaging provides the information conveniently. Since we do have spatial field information in the z dimension, and the different modes should have differing k_z, if we take the fourier transform in z instead of integrating in z, we are able to separate out the different modes.

It follows from the trancendental equations for a TE and TM slab waveguide mode that the tranverse wavelength of the modes should approximately follow $\lambda_{TM} = \sqrt{\varepsilon_r}\lambda_{TE}$. Because of this, for square waveguides in the limit $a << \frac{c}{\omega}$, 98% of the energy is in the lowest mode, having zero nodes in z. The ability to filter based on k_z does become important though, for the case of waveguides not in this limit, such as the ouput waveguide of the mode converter structure described in chapter 7.

6.3 Waveguide coupling efficiency

The coupling of energy between LN crystals has been considered before. Two relatively thick, 250 m slabs were put in direct contact, and polaritons were coupled from one slab to the other. In these qualitative experiments, in the region of interaction it was impossible to tell which crystal the energy was in, and coupling was only indicated by the presence of significant polariton amplitude in the coupled-to slab after the interaction region. Measurements were not conducted as a function of sparation between the slabs.

Using square waveguides like those considered in the previous section, and coupling them in the z dimension, we are able to directly observe the polaritons in both waveguides before, during, and after interaction. It is also possible to control the distance between the two waveguides, and thus to do a study of coupling as a function of separation distance.

Fairly narrowband, TEM$_{00}$, phonon-polariton wave-packets ($\sim$10 cycles, $\sim$0.4 THz, 100 μm wavelength) were generated near one end of a 50 μm x 50 μm x 3 mm LN waveguide, using an optical interference pattern as described in section 4.2.2. The overall generation laser spot was roughly 500 μm x 500 μm. The two initially counter-propagating 5-cycle polariton waves were combined after reflection of one of the waves from the end of the waveguide, to effectively double the number of cycles in the wave. The polariton response was monitored using real-space imaging as in section 4.3, showing the evolution in both the generation waveguide and the coupled waveguide, which was separated from the first by a variable distance d, see Figures 6-2 and 6-3.

To prevent accidental excitation of polaritons in the coupled waveguide, it is offset by 0.8 mm in the direction of propagation. Fourier filtered experimental images of polaritons in both waveguides, for separation distance d=20 microns and d=10 microns, 35 ps after excitation are shown in figure 6-4.

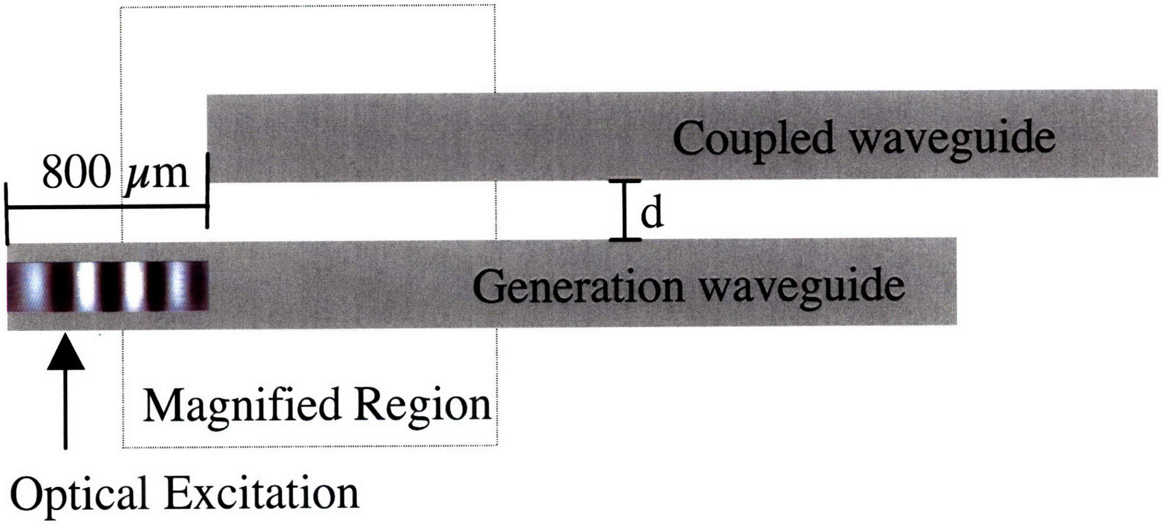
800 μm
Coupled waveguide
d
Generation waveguide
Magnified Region
Optical Excitation

Figure 6-2: Coupled waveguide sample geometry. Two 50 μm x 50 μm x 3 mm LN waveguides were separated by a variable distance d. Narrowband 400 GHz phonon-polaritons were driven in the generation waveguide, and their evolution within both waveguides was observed through real-space imaging.

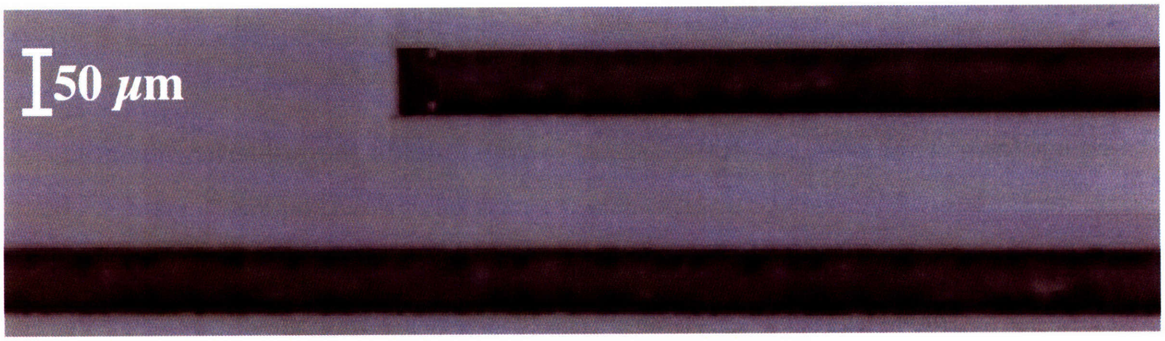

Figure 6-3: Optical micrograph of the coupled waveguides within the coupling region. All surface irregularities are substantially sub-wavelength for the 100 μm wavelength polariton excitations observed.

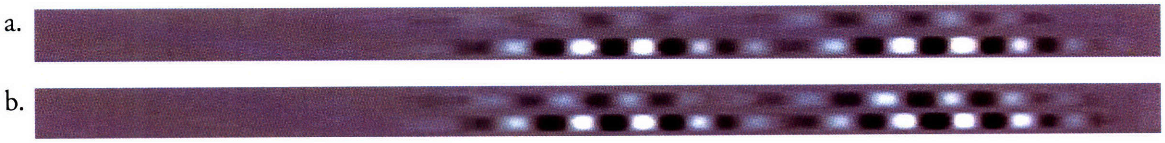

Figure 6-4: Polariton field inside two coupled 50 μm waveguides, observed 35 ps after excitation through real-space imaging, for two waveguide seperations $d = 20$ microns (a) and $d = 10$ microns (b). Images were filtered using 3D fourier bandpass filtering.

6.3.1 Expected coupling efficiency

Taking the solutions of a rectangular waveguide of dimension a x a, as derived in section 2.4, and coupling two waveguides across a separation distance d, we can describe the system as two perturbatively coupled waveguides, with solutions akin to the solutions of the double-square-well potential treated as a model in quantum mechanics.

Considering only the two lowest modes of the coupled system $(k_z)_1$ and $(k_z)_2$, they can be approximated as the linear combinations $\psi_\pm = (k_z)_1 \pm (k_z)_2$, with a wavevector separation of the two modes proportional to $e^{\kappa d}$.

In the z direction, assuming coupling primarily through H, we can write an a equation for the coupling rate[34],

$$\kappa_z = \frac{2\varepsilon_r k_z^2 k_z'}{k_x a(k_z^2 + \varepsilon_r^2 (k_z')^2)} \left[1 + \frac{\varepsilon_r}{k_z' a} \frac{k_z^2 + (k_z')^2}{k_z^2 + \varepsilon_r^2 (k_z')^2}\right]^{-1} e^{-dk_z'} \tag{6.1}$$

which for $a = 50\ \mu m$, $\omega = 400\ GHz$, $\varepsilon_r = 25.96$ yields the numerical formula,

$$\begin{aligned} \lambda_x = \frac{2\pi}{k_x} = 100\ \mu m,\ \lambda_y = \frac{2\pi}{k_y} = 20.6\ \mu m,\ \lambda_z &= \frac{2\pi}{k_z} = 702\ \mu m \\ \lambda_y' = \frac{2\pi}{k_y'} = 160\ \mu m,\ \lambda_z' &= \frac{2\pi}{k_z'} = 118\ \mu m \\ \kappa_z &= 1.46\ mm^{-1}\ e^{-\frac{d}{24.4\ \mu m}} \end{aligned} \tag{6.2}$$

For this symmetric system, the falloff rates for the coupled field (inversely proportional to k_z' and k_y', which are the transverse wavevectors in the cladding of the square-waveguide solution) are very similar in both y and z, though the field internal to the waveguide is much more uniform in z than in y. This uniformity enhances the efficiency of the initial driving of the TEM$_{00}$ mode.

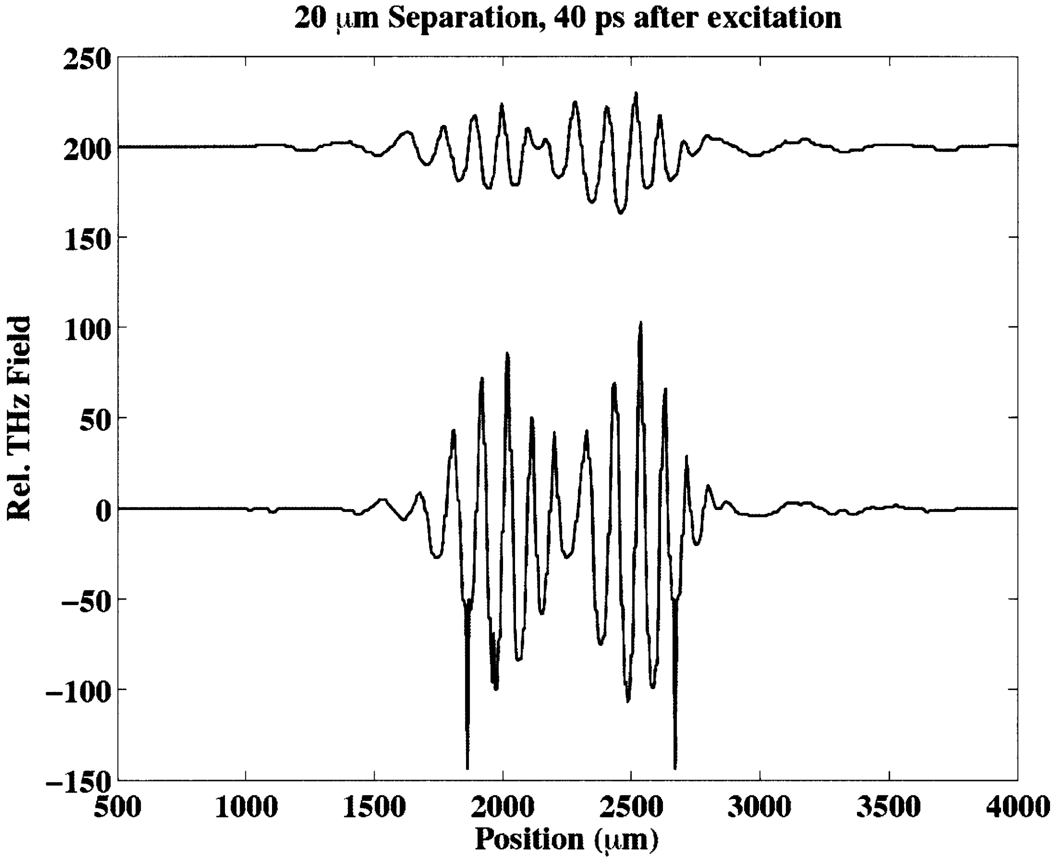

Figure 6-5: Polariton response in both coupled 50 μm waveguides, 40 ps after excitation, for a separation distance of 20 μm. Roughly 10% of the energy has been transferred into the coupled waveguide, and the two waves are $\pi/2$ out of phase.

6.3.2 Experimental coupling efficiency

By vertically integrating (in z) the polariton signal in each waveguide separately, a measure of the coupled THz field amplitudes is obtained for various separation distances d, ranging from 5 μm to 100 μm. It is possible to compare the THz fields in the two waveguides directly, as in Figures 6-5 and 6-6, where the signal is proportional to E_z in the waveguide. The phase shift of the THz carrier between the generating and coupled waveguides is $\frac{\pi}{2}$ within the accuracies of the experiment, which is in agreement with theory.

The rate of THz power transfer is determined by squaring the field values after background subtraction, and then temporally integrating. Taking the ratio of power

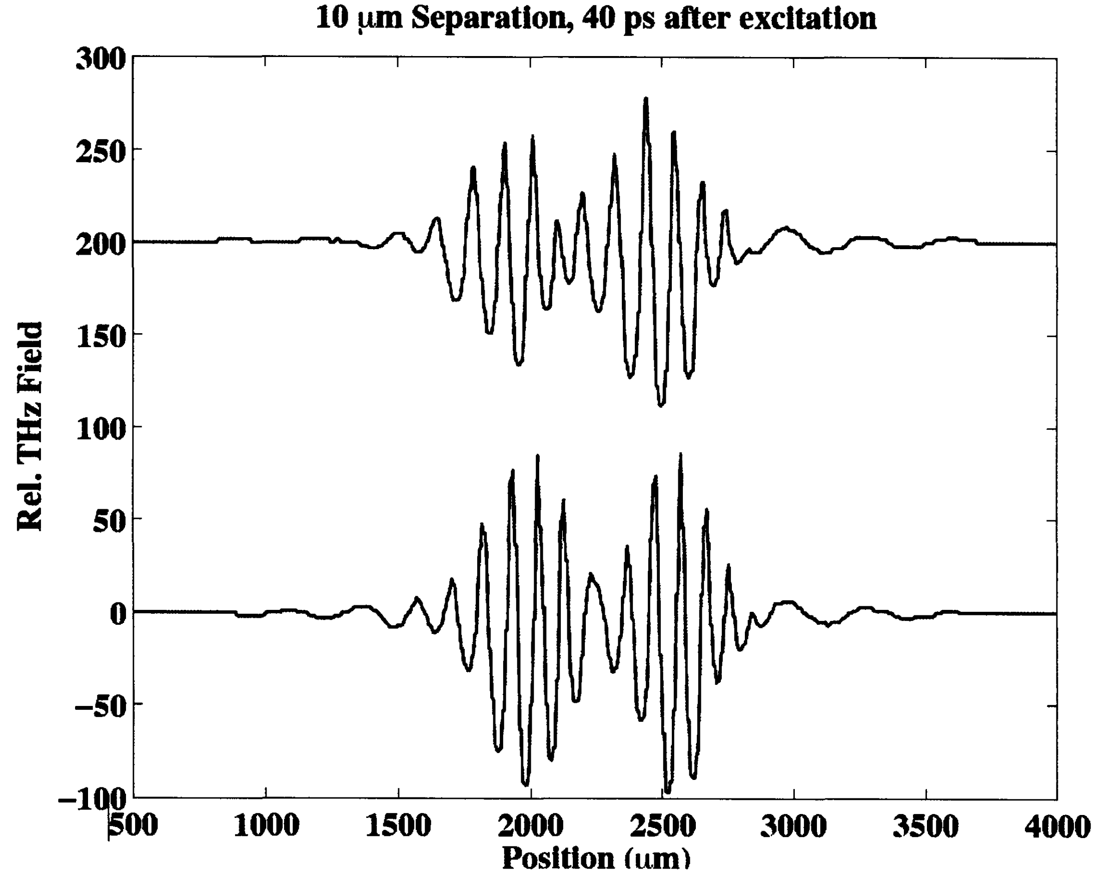

Figure 6-6: Polariton response in both coupled 50 μm waveguides, 40 ps after excitation, for a separation distance of 20 μm. Roughly 50% of the energy has coupled into the coupled waveguide, and the two waves are $\pi/2$ out of phase.

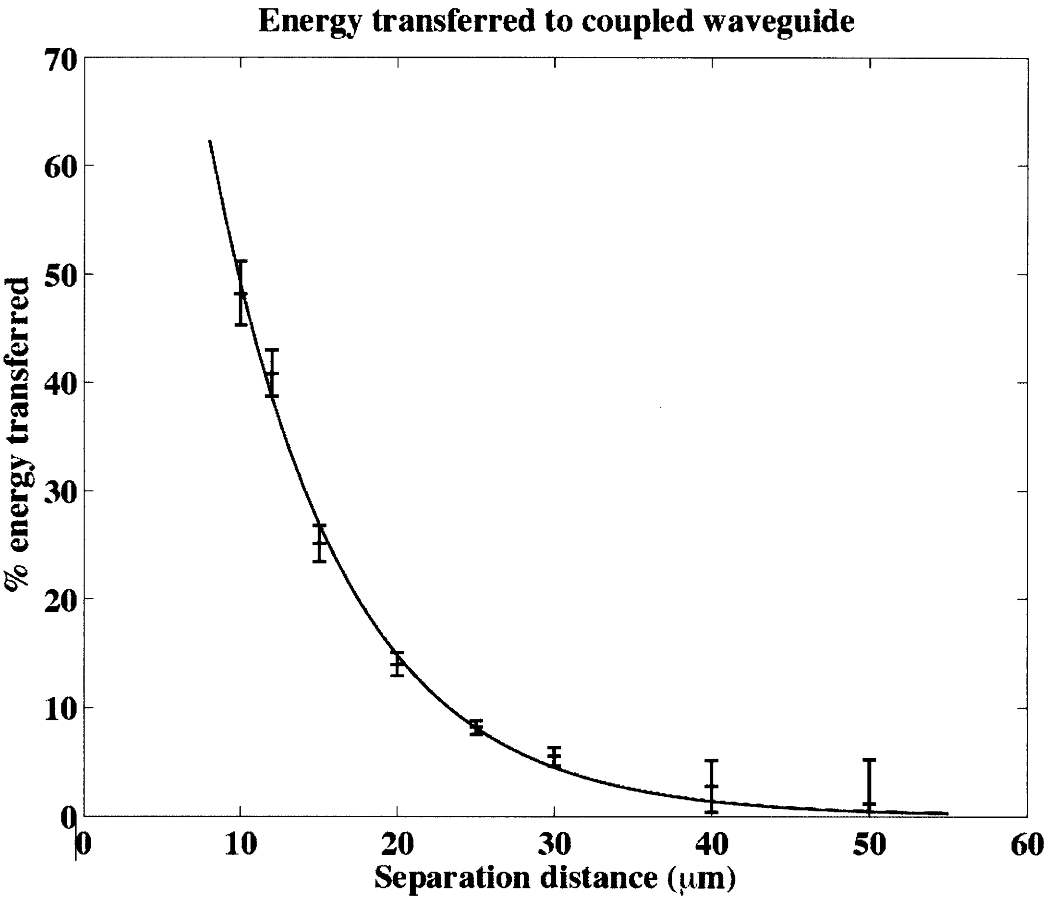

Figure 6-7: Energy transfer into the coupled waveguide as a function of separation distance, monitored 1 mm from the onset of coupling.

in the coupled waveguide to that in the generation waveguide yields figure 6-7. The large error bars at small separation distance are due to difficulties in separating the images of the two waveguides successfully, and at large separation due to the overall small amount of energy transfer.

Chapter 7

Mode Converting Structures

This work produced in collaboration with Kung-Hsuan Lin and David W. Ward of the Massachusetts Institute of Technology, and Kevin Webb of Purdue University.

Having considered the case of 2D confinement in two coupled square waveguides, the next level of complexity comes from patterning in the direction of propagation. Irregular mode converting structures, designed through eigenmode frequency domain calculations have been demonstrated both in the microwave[63] and optical[64] regimes. These structures are designed to operate in a frequency-dependent manner, delivering different outputs at selected frequency ranges, and although they introduce periodic patterning in the direction of propagation, the periodicity only partially occludes the propagating excitation, allowing for relatively strong signals to be observed through polariton real-space imaging.

7.1 Structure Design

In collaboration with Kevin Webb, a device for the conversion of wavelength dependent TE_{10} to TE_{30} modes in LT was designed, with the design frequency of 100 GHz. The design was generated though an iterative computational method based on the eigenmodes of the system[62], and as such, assumed CW input THz radiation. The structure was fabricated out of 250 μm thick LT, and coated with indium tin oxide

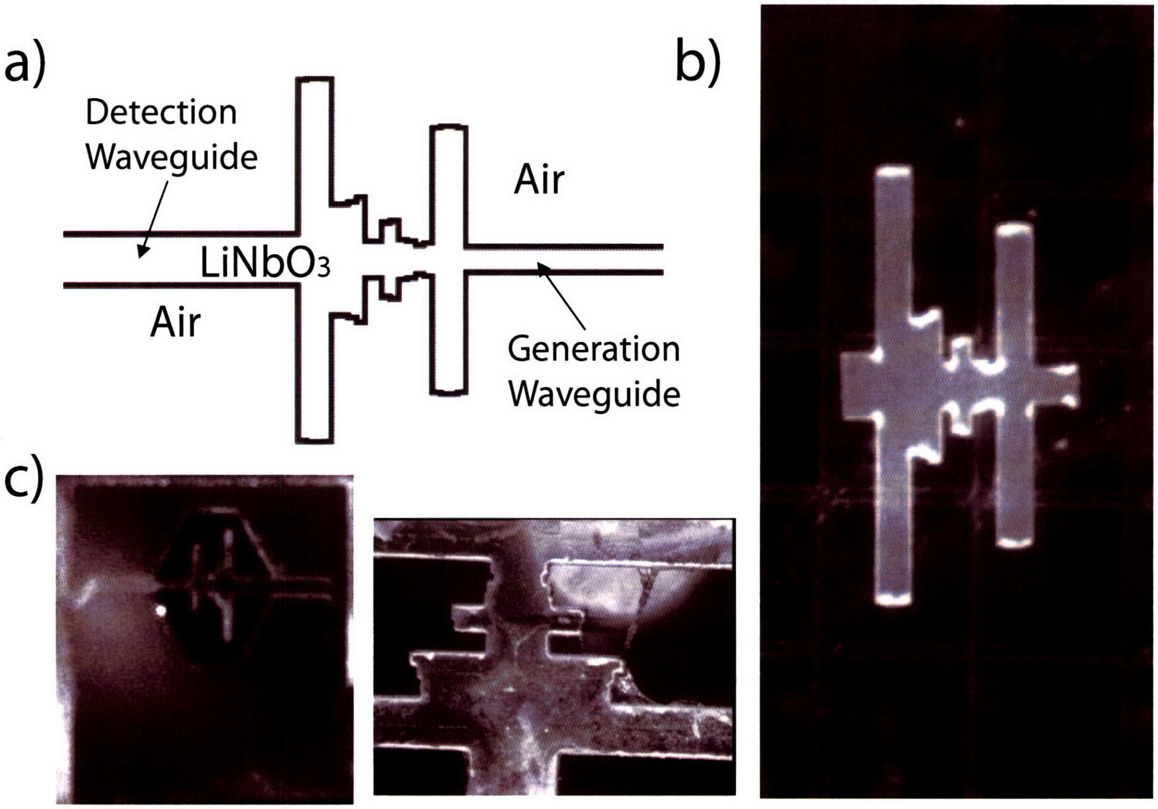

Figure 7-1: Mode converter structure, as designed (a), fabricated for 100 GHz in 250 μm thick $LiTaO_3$ (b), and fabricated for 300 GHz in 50 μm thick $LiNbO_3$ (c).

(ITO) to produce the desired PEC boundary conditions, see figure 7-1. However, due to the very long wavelengths required to measure at at 100 GHz, and the high frequency accuracy required, an experimental redesign was required.

By using uncoated crystals, the structure can be approximated as a TM waveguide, as dielectric waveguides with high dielectric contrast are quite well approximated by PMC boundary conditions. Therefore, the designed structure can be re-tasked as a TM_{10} to TM_{30} mode converter. Instead of the primary E component of the modes now being normal to the crystal surface (E_y), it is primarily E_z, which is also much better suited for detection purposes.

As Maxwell's equations scale, the structure could also be redesigned for 300 GHz by merely scaling by the indices of refraction at the two wavelengths, and by the ratio of the desired wavelength to the design wavelength. The structure was scaled

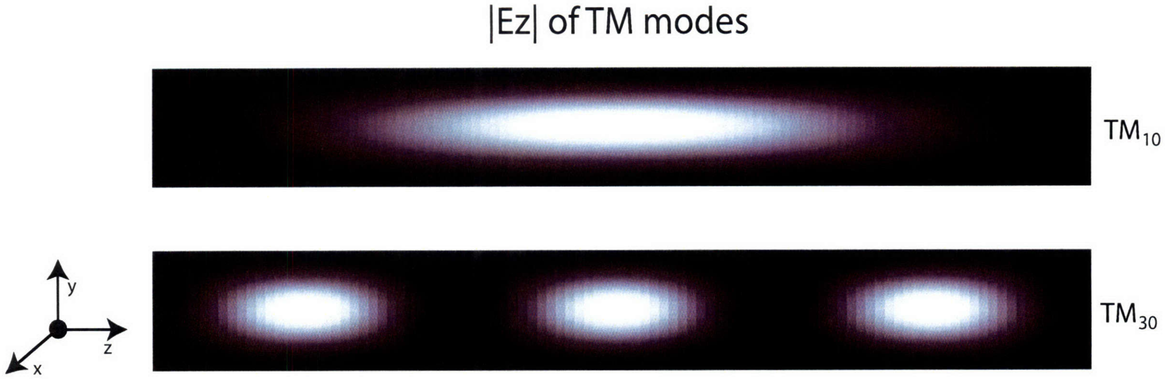

Figure 7-2: Magnitude of the E$_z$ component of the electric field of the TM$_{10}$ and TM$_{30}$ modes respectively of a perfect magnetic conductor (PMC). The transverse wavevector, k_z, is higher for the TM$_{30}$ mode.

to operate at 300 GHz in LN, with the scaling factors S_o and S_e in the ordinary and extraordinary axis dimensions given by,

$$S_o = \frac{\lambda}{\lambda_0} = \frac{n_{e0}(\omega_0)\omega_0}{n_e(\omega)\omega}, S_e = \frac{\lambda}{\lambda_0} = \frac{n_{e0}(\omega_0)\omega_0}{n_o(\omega)\omega}, \tag{7.1}$$

where λ, ω, n_o and n_e (λ_0, ω_0, n_{o0},n_{e0}) correspond to the wavelength, frequency, and ordinary and extrodinary refractive indicies in LN (LT).

The values of the indicies of refraction of LN were the corrected indicies of refraction for a slab waveguide of thickness 50 μm, as described in Section 2.4. For this scaling, effective values of $n_o = 3.5$, $n_e = 3.0$ yielded the scaling factors, $S_o = 0.43$ and $S_e = 0.52$, by which the dimensions of the structure were reduced. See Figure 7-1.

7.2 Experimental

The output of a Coherent Legend-HE Ti:sapphire regenerative amplifier (800 nm central wavelength, 60 fs pulse duration, 1 kHz repetition rate, 2.5 mJ/pulse) seeded by a KM Labs oscillator was used. A frequency selective TM$_{10}$ to TM$_{30}$ mode converter was fabricated out of x-cut 50 μm thick LiNbO$_3$ slabs using femtosecond laser machining[60]. The produced structure, shown in Figure 7-1c has surface irregularities of less than 5 μm in the transverse dimensions, and a bevel of less than 10 μm in the depth dimension, for a surface quality of better that $\lambda/10$ in all dimensions. The optic axis of the crystal was parallel to the longer transverse dimension of the input and output waveguides.

An 800 μJ excitation pulse was split by a transmissive binary phase mask, and the resultant ± 1 orders of diffraction were crossed in the input waveguide using cylindrical imaging optics. The crossed pulses formed an optical interference pattern whose wavevector was aligned with the long waveguide direction and whose period was 300 μm, resulting in a THz phonon-polariton response in the waveguide with the same spatial period.

Polariton propagation was recorded over a time period of 200 ps through real-space imaging using a variably delayed, 400-nm probe pulse [33]. The probe illuminated the entire structure to permit monitoring of polaritons within it. Since the sample was thin, requirements for phase-matching of the probe angle of incidence (such that the pump and probe propagation times through the sample were approximately equal) were relaxed. The excitation and probe light was polarized along the LN optic axis.

The optical interference pattern was roughly 1800 μm wide (the horizontal dimension if Fig. 7-4) x 1200 μm high, yielding about six interference fringes and ensuring uniformity across the short fabricated waveguide dimension (the vertical dimension of Fig. 7-4). The excitation was almost entirely of the TM_{10} mode of the waveguide. The initial spectrum of the excitation was determined through Fourier transformation of the temporal profile of the field within the input waveguide, just outside of the excitation region, see Figure 7-4. The several-fringe spatial excitation pattern generated a polariton wave with a center frequency of 300 GHz, with significant frequency components from 100-500 GHz.

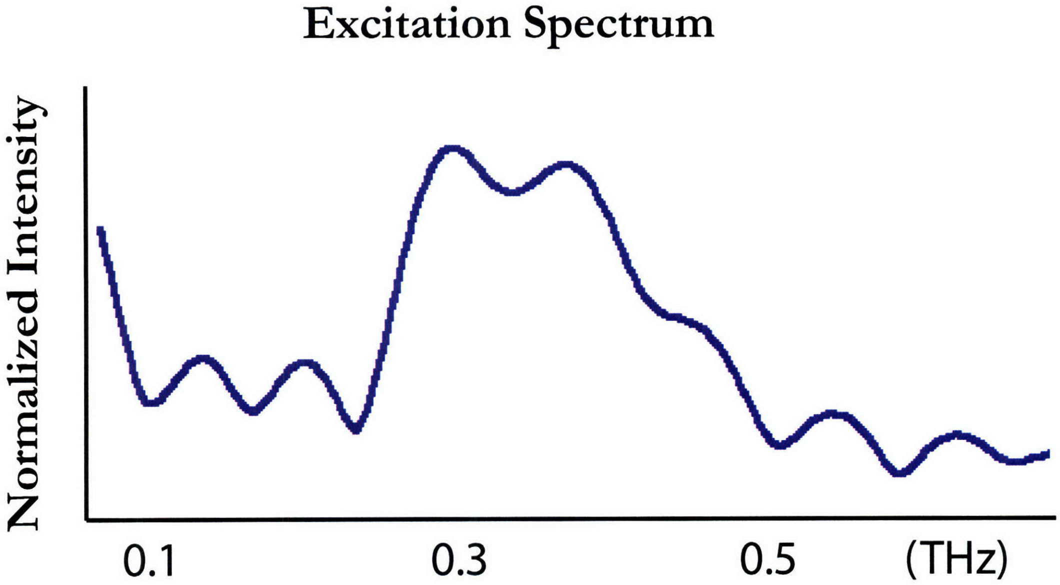

Figure 7-3: Mode converter excitation spectrum, measured throughout the input waveguide, outside of the initial generation region. The 300 GHz center frequency spectrum has significant components from 100-500 GHz.

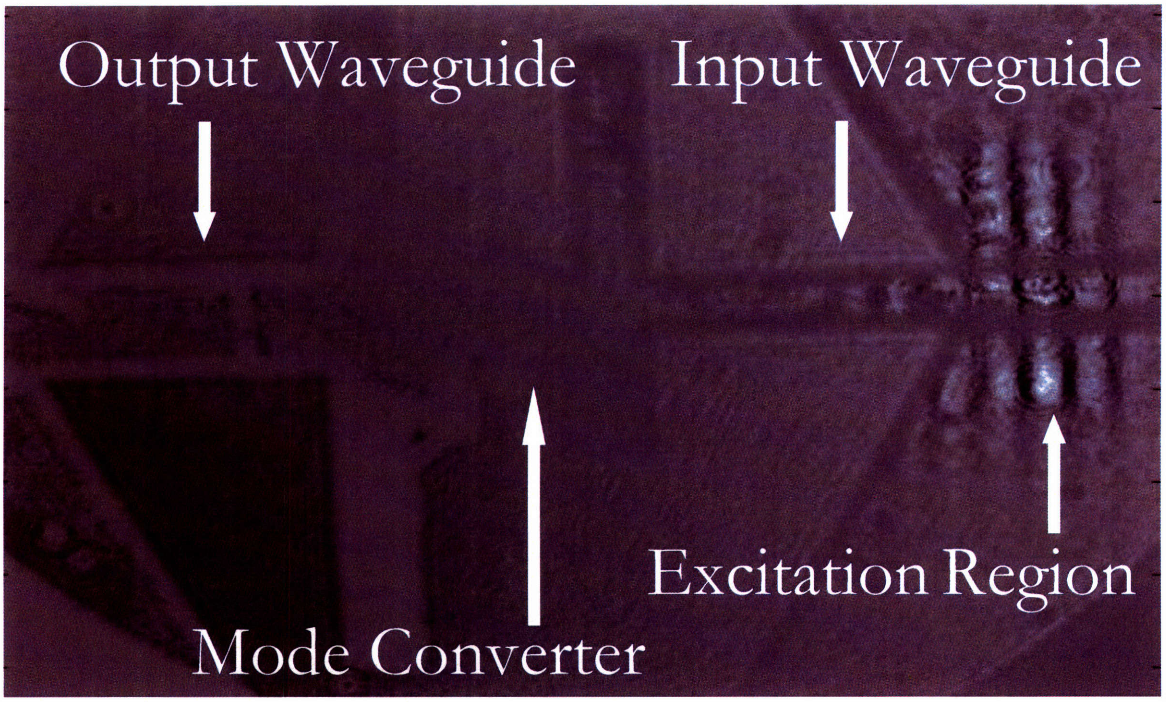
Output Waveguide
Input Waveguide
Excitation Region
Mode Converter

Figure 7-4: 300 GHz phonon-polaritons, inside the input waveguide of the mode converting structure, 2 ps after generation. The six cycle wave packet is almost entirely in the TM_{10} mode of the input waveguide.

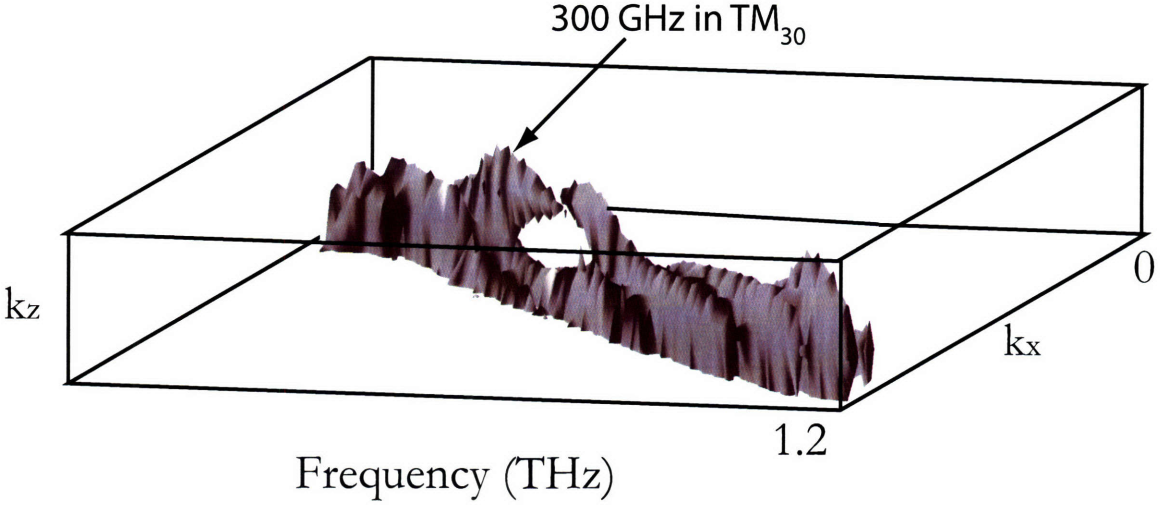

Figure 7-5: 3D Fourier transform of the output waveguide signal. The peaks of high k_z correspond to conversion to the TM_{30} mode of the waveguide.

7.3 3D Fourier Analysis

The two modes to be detected in the output waveguide, TM_{10} and TM_{30}, differ primarily in k_z (see Figure 7-2) which is detectable along the vertical dimension of the polariton images. To this end, instead of vertically integrating, as in usually done to generate two dimensional space-time plots, the images were also fourier transformed along z, maintaining a three dimensional data set with two wavevector dimensions k_x and k_z, and a frequency dimension ω, see Figure 7-5. Filtering out high k_z corresponding to the TM_{30} mode, and back fourier transforming, yields the space-time plot of the TM_{10} mode in the output waveguide, see Figure 7-6.

Taking each mode and integrating its amplitude for all k_x, normalizing based on the input spectrum, and plotting as a function of frequency yields the impulse response spectrum of the system, see Figure 7-7. Significant coupling of THz fields into the TM_{10} and TM_{30} modes of the output waveguide is observed, with total energy transfer to the output waveguide of roughly 25% of the input. Frequency selective

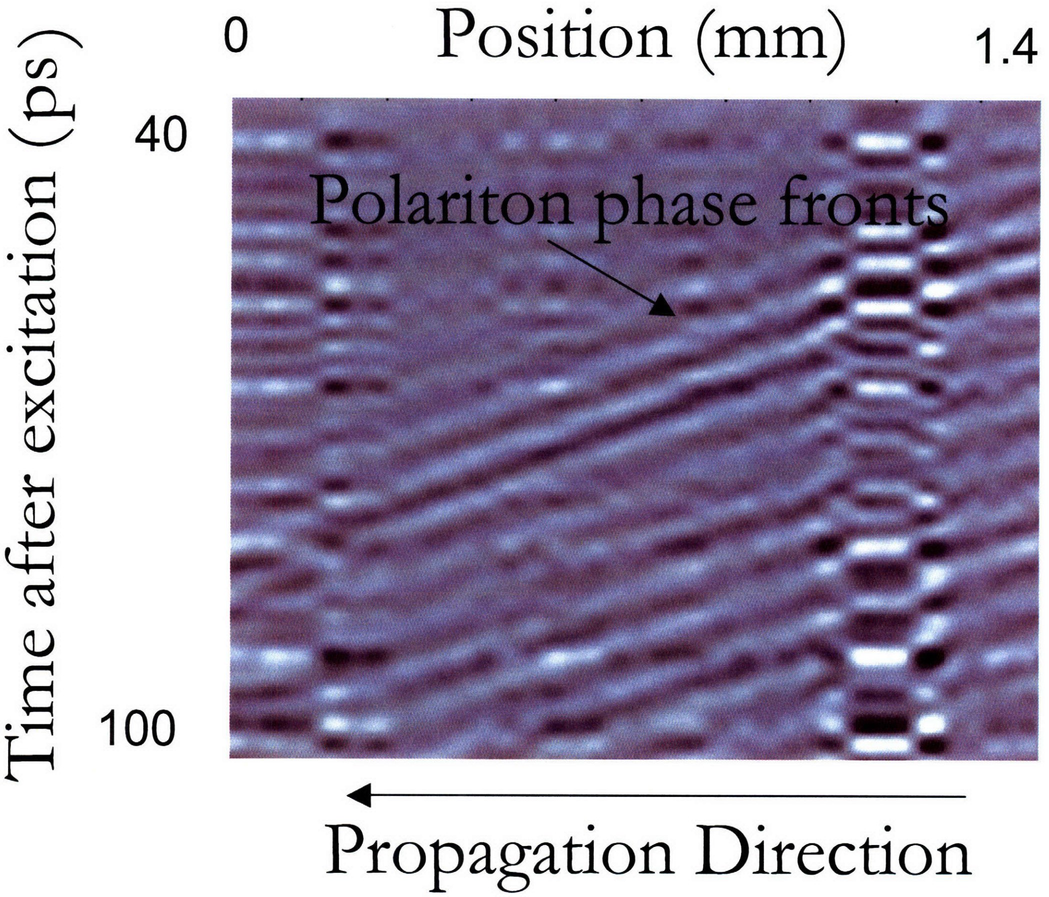

Figure 7-6: Space-time plot of the lowest order TM_{10} mode in the output waveguide. Generated by back Fourier Transforming the full data set, after filtering out high k_z signal.

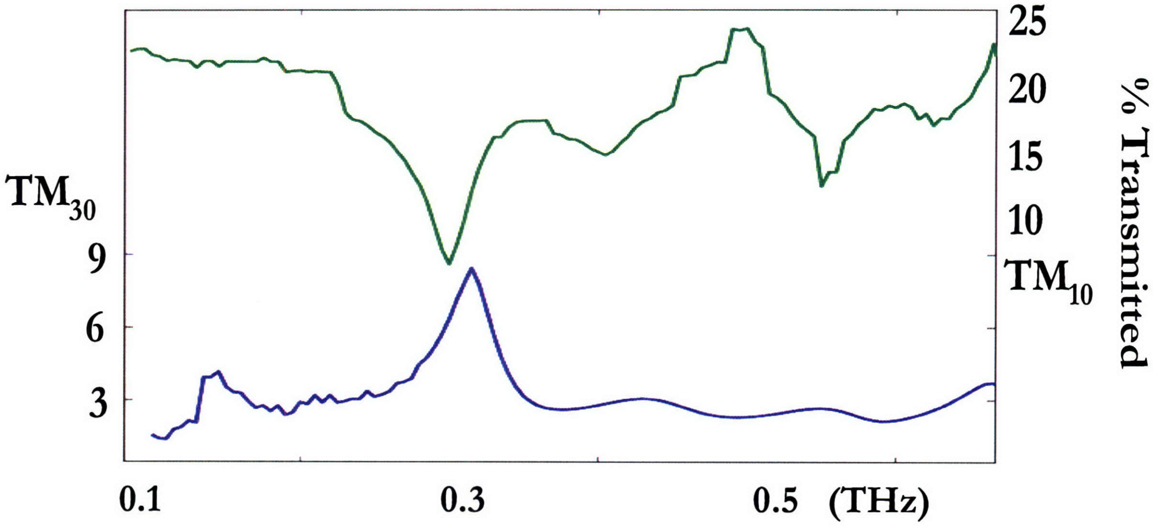

Figure 7-7: Mode converter output spectrum, normalized to the input spectrum shown in Figure 7-3. The TM$_{30}$ mode is selectively outputted at 300 GHz.

conversion into the TM$_{30}$ mode is demonstrated by the strong peak at 290 GHz. The deviation from the 300 GHz target frequency is likely due to slight errors in the indices of refraction used for the redesign.

Chapter 8

Photonic Crystals

This work partially produced in collaboration David W. Ward of the Massachusetts Institute of Technology.

The introduction of index of refraction periodicity in the direction of propagation yields the photonic crystal domain. Ranging from the one-dimensional photonic crystals used as dielectric mirrors[21], which at their simplest can be expressed as quarter-wave stacks, to full three-dimensional photonic crystals made by filling voids around polystyrene beads[19], the frequency responses of these structures have been well characterized in the visible, near IR, and even microwave frequencies, typically by looking at the transmission and reflection spectra of these fabricated structures.

Polariton imaging allows us to perform these experiments in the THz regime, imparting specific frequencies upon a patterned photonic crystal, and detecting both the transmission and reflection. In addition to this standard experiment, the ability to probe fields propagating transverse to a probe beam, and to fabricate the photonic structure out of our polariton generation and detection medium (LN), allows the direct imaging and characterization of the fields within the interaction region. Additionally, the wavevector-specific nature of the ISRS pumping mechanism allows the excitation of all the resonant frequencies of a photonic structure at the same time.

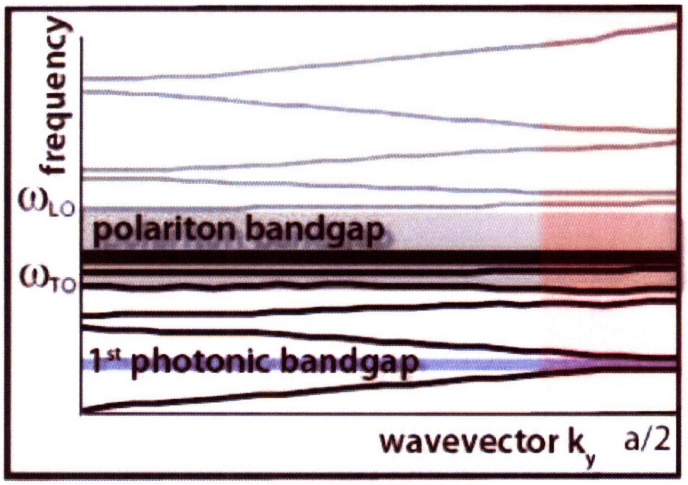

Figure 8-1: Schematic dispersion relation of a photonic crystal in a material such as LN with a polariton mode. The imposed photonic bandgap and the intrinsic polariton bandgap interact to produce propagating modes at frequencies which would be forbidden in an upatterned crystal[29].

8.1 Photonic Crystal Fabrication

Using femtosecond laser machining, holes of various sizes ranging from 1-50 microns in diameter were carved into a 50 micron thick LN slab. Holes of constant size were arranged in six square arrays of 21x21 holes with a 100 micron periodicity, to produce six different 2D slab photonic crystals of overall dimension 2 mm x 2 mm, Figure 8-2. The higher-filling fraction (larger hole) photonic crystals exhibit relatively irregularly shaped holes, Figure 8-3, but the imperfections are significantly sub-wavelength, and thus have little effect on the crystal properties[28].

8.2 2D Photonic Slab Experiments

The square lattice, air-hole-in-LN photonic crystals with lattice periodicity $a = 100\mu m$ and hole diameters $d = \{9, 15, 30, 50\}\mu m$ were probed using the real-space imaging techniques described in Chapter 4. The signal was recorded on a Pixis 1024 camera using a roughly normal incidence 400 nm probe, with the transmitted pump blocked at an interim focal plane of the imaging telescope.

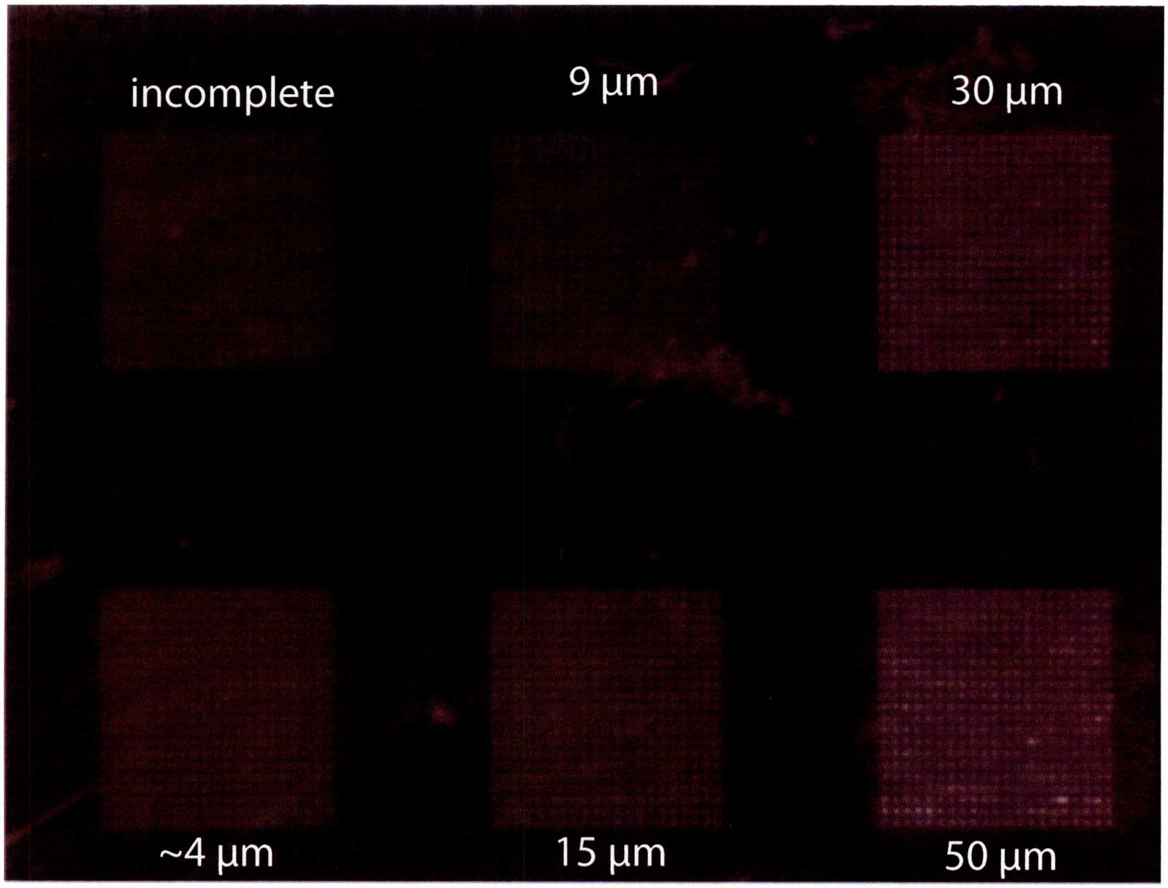
incomplete
9 µm
30 µm
~4 µm
15 µm
50 µm

Figure 8-2: Photonic crystal sample machined in 50 micron thick LN. Six individual 2D slab photonic crystals were fabricated, with hole diameters ranging from 50 microns down to 4 microns as indicated. All photonic crystals have 20 periods in both the x and z dimensions, with a lattice spacing, a of 100 microns between neighboring holes.

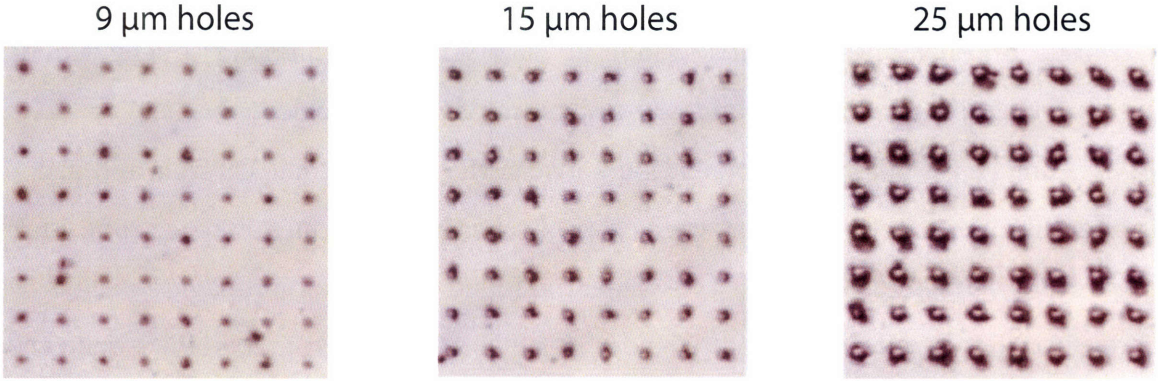
9 µm holes
15 µm holes
25 µm holes

Figure 8-3: Close-up images of photonic crystals machined in 50 micron thick LN.

Diffraction of the pump beam off of the periodic structure of the photonic crystal caused reduced signal to noise when compared to typical real-space imaging techniques. To improve signal to noise sufficiently required extremely long averaging at each time step, and careful filtering of the resultant data set using 3D fourier transform methods similar to those used in Chapter 7.

The slab photonic crystals fabricated should exhibit a first photonic band gap for radiation propagating primarily in x at approximately 275 GHz, with a photonic crystal with a filling fraction of 50% (hole diameter $d = 80\mu m$) having the largest band gap. The 50 micron diameter hole photonic crystal was the highest filling fraction crystal which could be fabricated, as larger hole diameters caused the LN slab to fracture.

Two types of excitation were used to study the frequency response of the photonic crystals, a broadband 'frequency-specific' excitation, and a wave-vector specific excitation.

8.2.1 Frequency-Specific Excitation

A broadband, initially single-cycle phonon polariton excitation was driven in the 50 micron thick LN slab waveguide in between the highest filling fraction (hole diameters of 30 and 50 microns) photonic crystals shown in Figure 8-2. The initial excitation had a spatial FWHM of 200 microns, which primarily drove the two lowest slab waveguide modes, producing a mode symmetric into the depth of the slab at 300 GHz and another anti-symmetric mode at 800 GHz. The higher frequency mode exhibited significant damping and dispersion and thus was neglected.

The images of polariton propagation between the two photonic crystals and inside the lower filling-fraction crystal were integrated in z to produce a space-time plot, Figure 8-4. As indicated, most of the broadband excitation propagates right on through the photonic crystal, but a small, highly narrowband fraction of it is reflected off of the photonic crystal, and is observed as it propagates back to the generation slab region. Fourier transforming the time domain response of the reflected signal off

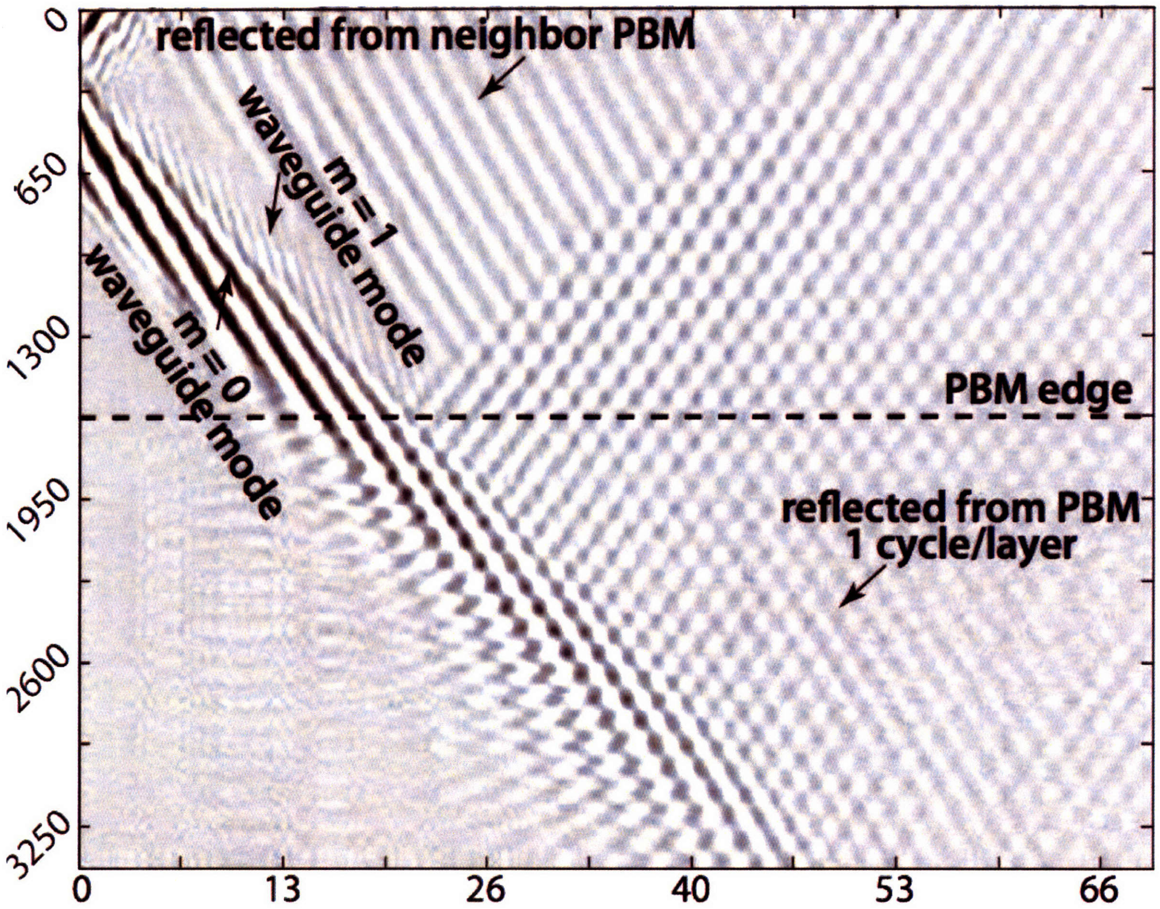

Figure 8-4: Space-time plot showing polariton signals, driven by a 300 GHz center-frequency broadband excitation in the unpatterned LN slab region between two neighboring photonic crystals of hole diameters 50 and 30 microns. The narrowband signals appear due to reflections off of the bandgap structures.

of both photonic crystals yields Figure 8-5. Both photonic crystals reflected ~285 GHz polaritons with the higher filling fraction crystal reflecting a significantly broader bandwidth.

8.2.2 Wavevector-Selected Excitation

Broadband phonon-polaritons with a center wavelength in the material of twice the lattice periodicity ($\lambda_{\text{center}} = 200\mu m$) were generated directly in the 30 micron diameter hole photonic bandgap crystal shown in Figure 8-3. By driving the excitation inside of the photonic crystal as opposed to in the surrounding slab, all branches

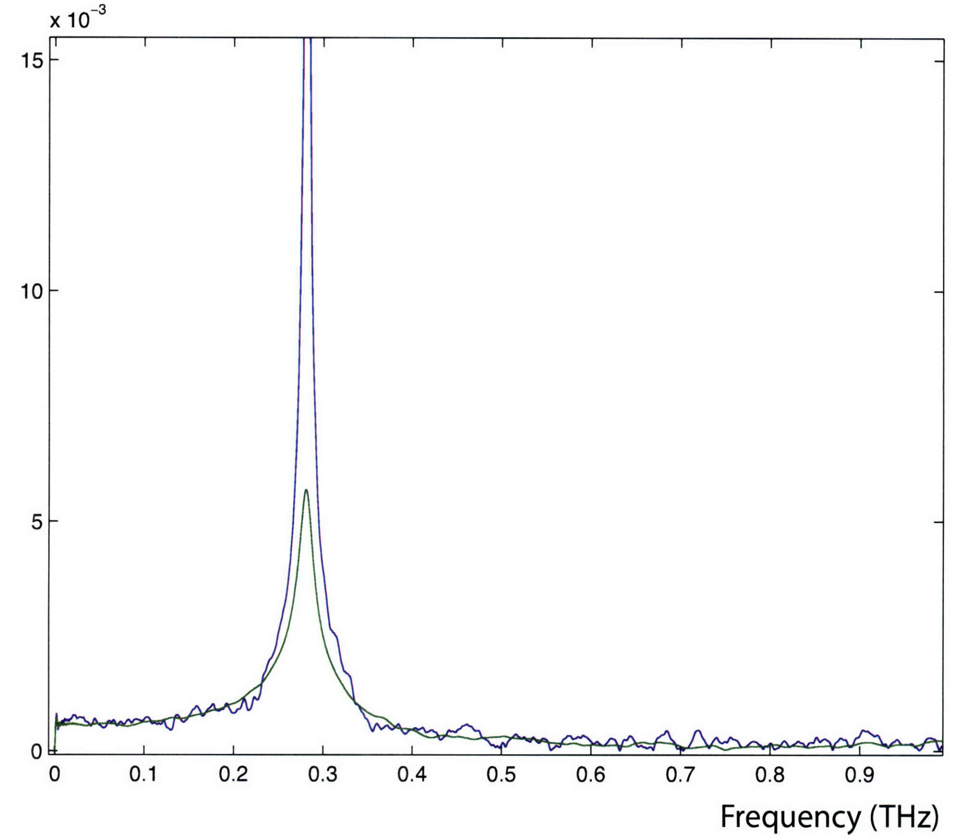

Figure 8-5: Un-normalized spectra of the two reflected polariton responses in Figure 8-4. The blue line corresponds to radiation rejected by the lower filling fraction 30 micron diameter hole photonic crystal, the green to radiation rejected by the 50 micron diameter hole photonic crystal.

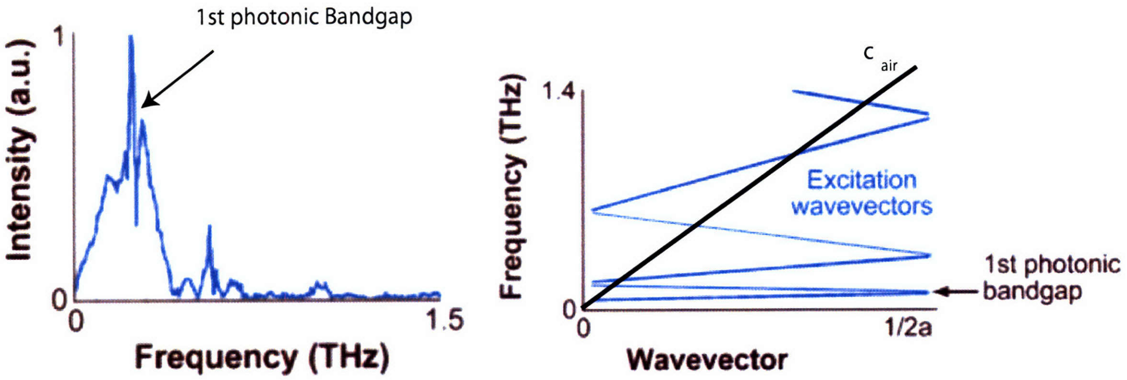

Figure 8-6: Square lattice photonic crystal excited by a 200 micron center-wavelength wavepacket, inside of the photonic crystal. The six branches of the photonic crystal dispersion relation are driven, with two distinct photonic bandgaps observable at 280 and 610 GHz. A third bandgap at 1.1 THz is also suggested by the data.

of the photonic crystal dispersion relation will be driven, thus producing additional frequency components in the signal that were not observed in the previous section.

The response was Fourier transformed in time, at a position $\sim$1 mm away from the initial excitation location, windowing the time response to neglect the elements of the THz excitation which do not couple to an eigenmode of the system, Figure 8-6a. The excitation wavevector range is indicated on the right-hand side of the theoretically calculated dispersion curve shown in Figure 8-6b. All parts of the dispersion curve which lie above and to the right of the c_{air} line, or at higher wavevectors than $1/2a = 1/200\mu^{-1}$, are non-propagating responses of the system.

The lowest 5-6 modes of the photonic crystal at the driven wavevector are evident in the spectrum. Because we have excited the system at the high end of its supported wavevectors, the modes show up as doublets in the spectrum, The first two branches are at around 300 GHz, with the narrow bandgap observed in the previous section dividing them at 285 GHz. The second pair occurs at 600 GHz, and the last at 1.1 THz. These six modes are the only modes of the system which lie under the light line of the photonic crystal, as the speed of light in the air cladding produces an effective frequency cap of 1.5 THz on the dispersion relation of the system.

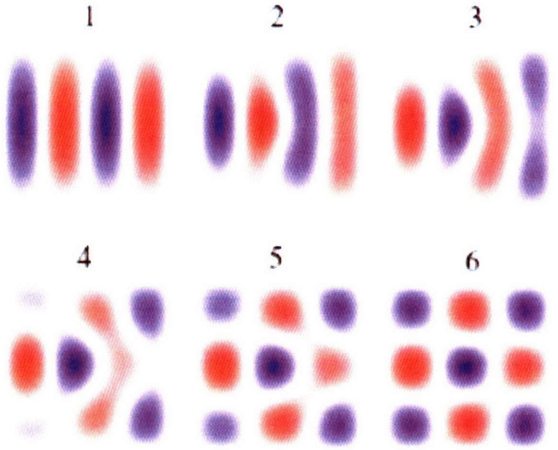

Figure 8-7: Lowest six photonic crystal modes of an air-hole-in-high dielectric 2D slab photonic crystal[27]. Higher order modes exhibit more nodes in the z direction. In the case of the LN photonic crystal studied, these correspond to all 6 eigenmodes of the lower polariton branch.

8.2.3 Normal Mode Imaging

Ideally, it should be possible to use the raw images used to generate the 1D spectra to directly visualize the photonic crystal modes, schematically depicted in Figure 8-7, and to use time domain Fourier filtering to separate the different photonic crystal modes based on their different frequencies. The low signal to noise of the experiment requires careful 3D Fourier filtering to produce good images of the modes.

Filtering out all spatial signals that appear inside the air holes (due to out of focus imaging), all wave-vectors higher than 0.005 μm^{-1} in both x and z, all signals above and to the left of the air light-line, and all responses a magnitude of less than 0.35 of the median in the 3D fourier transform, yields Figure 8-8a. This particular image is of the polariton field 80 ps after excitation, The non-real artifact signals from inside the air holes are occluded.

By applying an additional level of fourier filtering to the data-set, it is possible to isolate a single eigenmode of the crystal, Figure 8-8b. The 285-400 GHz bandpass filter applied to generate this image corresponds to the second eigenmode of the system, as evident by the variation in z which has developed. Higher order modes

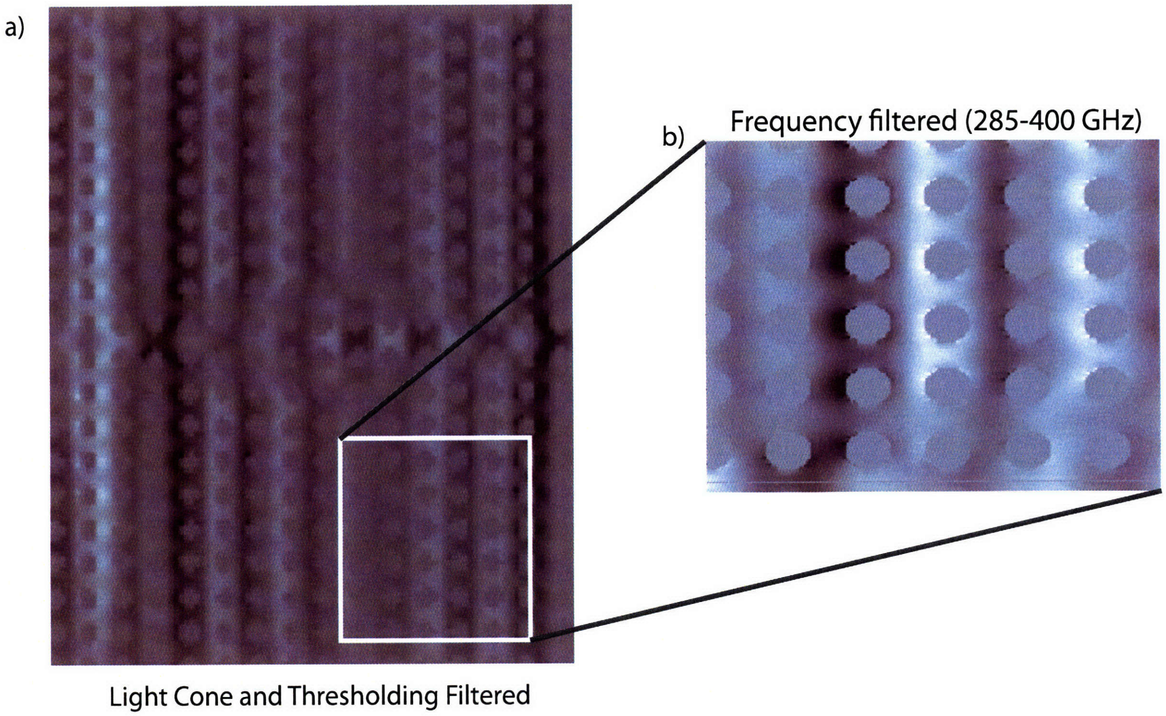

Figure 8-8: Photonic crystal with 15 micron diameter holes, driven with a 200 micron center-wavelength broadband polariton excitation. The resultant three dimensional dataset was Fourier-filtered in all three dimensions, discarding all signal which are unsupported by the photonic crystal. The resultant filtered fields approximately 80 ps post excitation are pictured in (a), and a subset image with an additional tight frequency bandpass filter applied is depicted in (b). The image in (b) is of the first excited mode of the photonic crystal.

have insufficient signal to generate images of their modal character. Overall, the excitation strength seen in the different modes corresponds well with the expected distribution. Primarily, the photonic crystal is driven in modes 1 and 2, which are most similar to the vertically uniform initial excitation spot.

In conclusion, we have shown the ability to excite two-dimensional slab photonic bandgap crystals in both a frequency-specific, and wavevector-specific manner, measured the properties of the first photonic bandgap with both methods to good agreement, and have directly imaged the THz electric field profile within these structures. Unlike many other methods of probing the properties of photonic crystals, polariton imaging allows the first direct detection of the fields while still inside the structure.

Chapter 9

Conclusions

The ability to directly image electromagnetic fields though their coupling to the phonon modes of a crystal allows the imaging of light while it is interacting with various imposed structures. In this thesis examples of THz dispersion relations in slab and rectangular waveguides, mode converting structures, and photonic crystal were probed using this method, and the first direct images of fields while inside the structures generated.

Polariton real-space imaging allowed the isolation of specifically-spatially variant data from these structures which would normally have been inaccessible due to either signal to noise considerations, such as in the slab and rectangular waveguides, or average signal being unchanged except for its spatial characteristic, such as in the photonic bandgap crystals and mode converting structures. Future applications of this technique should allow the direct monitoring of THz fields as they are absorbed or emitted by THz chromophores such as quantum dots.

One challenge of all the work in this thesis was the extreme amounts of data processing required to produce meaningful datasets from the very noisy experimental data. Without the use of selective Fourier filtering of the datasets, directed and confirmed by FDTD simulations, the results from both the photonic crystals and mode converting structures would have been unintelligible. Future work, which is already ongoing and partially successful will improve the imaging of the fields by at least an order of magnitude, thus allowing far easier interpretation of structure responses.

Ongoing improvements on signal acquisition will also finally allow the experimental determination of all the distinct components of the THz electric field. Unlike in the preceding experiments, where final signals were a conglomeration of all three THz field polarizations, which were then confirmed by simulation, it will soon be possible to directly measure the field components opening the door to the measurement of fields within full three dimensional structures such as 3D-polaritonic crystals and TE-TM mode converting structures.

Both the numerical simulation methods and experimental techniques developed in this thesis should enable the development and understanding of THz spectroscopic techniques whether in free space, or performed entirely within a $LiNbO_3$ optical workbench.

Bibliography

[1] D. H. Auston and M. C. Nuss. Electrooptic Generation and Detection of Femtosecond Electrical Transients. *IEEE Journal of Quantum Electronics*, 24(2):184–196, 1988.

[2] A. S. Barker, A. A. Ballman, and J. A. Ditzenberger. Infrared Study of the Lattice Vibrations In $LiTaO_3$. *Phys. Rev. B*, 2(10):4233–4239, 1970.

[3] A. S. Barker and R. Louden. Dielectric Properties of Optical Phonons in $LiNbO_3$. *Phys. Rev.*, 158(2):433–445, 1967.

[4] W.L. Barnes, A. Dereux, and T.W. Ebbesen. Surface plasmon subwavelength optics. *Nature*, 424:824–830, 2003.

[5] I.E. Barry, G.W. Ross, P.G.R. Smith, R.W. Eason, and G. Cook. Microstructuring of lithium niobate using differential etch-rate between inverted and non-inverted ferroelectric domains. *Materials Letters*, 37(4-5):246–254, 1998.

[6] S.I. Bozhevolnyi, V.S. Volkov, T. Søndergaard, A. Boltasseva, P.I. Borel, and M. Kristensen. Near-field imaging of light propagation in photonic crystal waveguides: Explicit role of Bloch harmonics. *Physical Review B*, 66(23):235204, 2002.

[7] C.J. Brennan. *Femtosecond Wavevector Overtone Spectroscopy of Anharmonic Lattice Dynamics in Ferroelectric Crystals.* PhD thesis, Massachusetts Institute of Technology, 1997.

[8] P.T. Brown, S. Mailis, I. Zergioti, and R.W. Eason. Microstructuring of lithium niobate single crystals using pulsed UV laser modification of etching characteristics. *Optical Materials*, 20(2):125–134, 2002.

[9] A. Cavalleri, S. Wall, C. Simpson, E. Statz, D. W. Ward, K. A. Nelson, M. Rini, and R. W. Schoenlein. Tracking the motion of charges in a terahertz light field by femtosecond X-ray diffraction. *Nature*, 442:664–666, 2006.

[10] D. J. Cook, J. X. Chen, E. A. Morlino, and R. M. Hochstrasser. Terahertz-Field-Induced Second-Harmonic Generation Measurements of Liquid Dynamics. *Chem. Phys. Lett.*, 309(3-4):221–228, 1999.

[11] P. Dawson, F. de Fornel, and JP Goudonnet. Imaging of surface plasmon propagation and edge interaction using a photon scanning tunneling microscope. *Physical Review Letters*, 72(18):2927–2930, 1994.

[12] H. Deng, G. Weihs, C. Santori, J. Bloch, and Y. Yamamoto. Condensation of Semiconductor Microcavity Exciton Polaritons. *Science*, 298(5591):199, 2002.

[13] V. G. Dmitriev, G. G. Gurzadyan, and D. N. Nikogosyan. *Handbook of Nonlinear Optical Crystals*, volume 64 of *Springer series in optical sciences.* Springer-Verlag, New York, 3^{rd} edition, 1999.

[14] T. P. Dougherty, G. P. Wiederecht, K. A. Nelson, M. H. Garrett, H. P. Jenssen, and C. Warde. Femtosecond Resolution of Soft Mode Dynamics in Structural Phase Transistions. *Science*, 258(5083):770–774, 1992.

[15] T. P. Dougherty, G. P. Wiederecht, K. A. Nelson, M. H. Garrett, H. P. Jenssen, and C. Warde. Femtosecond Time-Resolved Spectroscopy of Soft Modes in Structural Phase Transistions of Perovskites. *Phys. Rev. B*, 50(13):8996–9019, 1994.

[16] T. Feurer, N.S. Stoyanov, D.W. Ward, J.C. Vaughan, E.R. Statz, and K.A. Nelson. Terahertz Polaritonics. *Annu. Rev. Mater. Res.*, 37:317–350, 2007.

[17] T. Feurer, J. C. Vaughan, and K. A. Nelson. Spatiotemporal Coherent Control of Lattice Vibrational Waves. *Science*, 299:374–377, 2003.

[18] G. Gallot, S. P. Jamison, R. W. McGowan, and D. Grischkowsky. Terahertz Waveguides. *J. Opt. Soc. Am. B*, 17:851–863, 2000.

[19] B. Gates, S.H. Park, and Y. Xia. Tuning the Photonic Bandgap Properties of Crystalline Arrays of Polystyrene Beads by Annealing at Elevated Temperatures*. *Adv. Mater*, 12(9), 2000.

[20] E. N. Glezer and E. Mazur. Ultrafast-Laser Driven Micro-Explosions in Transparent Materials. *Appl. Phys. Lett.*, 71:862–864, 2001.

[21] S.D. Hart, G.R. Maskaly, B. Temelkuran, P.H. Prideaux, J.D. Joannopoulos, and Y. Fink. External Reflection from Omnidirectional Dielectric Mirror Fibers, 2002.

[22] H. A. Haus. *Waves and Fields in Optoelectronics.* Prentice Hall, New York, 1983.

[23] Kerwyn Casey Huang, Peter Bienstman, J.D. Joannopoulos, Keith A. Nelson, and Shanhui Fan. Field Expulsion and Reconfiguration in Polaritonic Photonic Crystals. *Phys. Rev. Lett.*, 90:196402, 2003.

[24] Kerwyn Casey Huang, Peter Bienstman, J.D. Joannopoulos, Keith A. Nelson, and Shanhui Fan. Phonon-Polariton Excitations in Photonic Crystals. *Phys. Rev. B*, 68:075209, 2003.

[25] I. Inbar and R. E. Cohen. Comparison of the Electronic Structures and Energetics of Ferroelectric $LiNbO_3$ and $LiTaO_3$. *Phys. Rev. B*, 53(3):1193–1204, 1996.

[26] J. D. Jackson. *Classical Electrodynamics.* John Wiley & Sons, New York, 3 edition, 1999.

[27] J.D. Joannopoulos, R.D. Mead, and J.N. Winn. *Photonic Crystals: Molding the Flow of Light.* Princeton, New York, 1995.

[28] S.G. Johnson and J.D. Joannopoulos. *Photonic Crystals: The Road from Theory to Practice.* Kluwer, Boston, 2002.

[29] Steven G. Johnson and J.D. Joannopoulos. Block-Iterative Frequency-Domain Methods for Maxwell's Equations in a Planewave Basis. *Optics Express*, 8(3):173–190, 2001.

[30] I. P. Kaminow and J. W. D. Johnston. Quantitative Determination of the Sources of the Electro-Optic Effect in $LiNbO_3$ and $LiTaO_3$. *Phys. Rev.*, 160(3):519–522, 1967.

[31] C. Kittel. *Quantum Theory of Solids.* John Wiley and Sons, New York, second edition, 1987.

[32] R. M. Koehl. *Spatial and Temporal Ultrafast Imaging and Control of Terahertz Wavepackets.* PhD thesis, Massachusetts Institute of Technology, 2000.

[33] R. M. Koehl, S. Adachi, and K. A. Nelson. Real-Space Polariton Wave Packet Imaging. *J. Chem. Phys.*, 110(3):1317–1320, 1999.

[34] M. Kuznetsov. Expressions for the coupling coefficient of a rectangular-waveguide directional coupler. *Optics Letters*, 8:499–501, 1983.

[35] R. J. Leubbers and F. Hunsberger. . *IEEE Trans. on Electromagnetic Compatibility*, 32:222, 1990.

[36] R. J. Leubbers and F. Hunsberger. FDTD for N^{th}-Order Dispersive Media. *IEEE Trans. Antennas and Propagation*, 40(11):1297–1301, 1992.

[37] M. Levy, Jr. R. M. Osgood, R. Liu, L. E. Cross, III G. S. Cargill, A. Kumar, and H. Bakhru. Fabrication of Single-Crystal Lithium Niobate Films by Crystal Ion Slicing. *Appl. Phys. Lett.*, 73:2293–2295, 1998.

[38] Chiyan Luo, Mihai Ibanescu, Steven G. Johnson, and J.D. Joannopoulos. Cerenkov Radiation in Photonic Crystals. *Science*, 299:368–371, 2003.

[39] S. Mailis, C. Riziotis, IT Wellington, PGR Smith, CBE Gawith, and RW Eason. Direct ultraviolet writing of channel waveguides in congruent lithium niobate single crystals. *Optics Letters*, 28(16):1433–1435, 2003.

[40] G. Malpuech, A. Kavokin, A. Di Carlo, and JJ Baumberg. Polariton lasing by exciton-electron scattering in semiconductor microcavities. *Physical Review B*, 65(15):153310, 2002.

[41] P. Meier and T. Feurer. Characterization of Methods of Real Space Imaging. *In Process*, 2008.

[42] N. Mitsugi and H. Nagata. Challenges in Electron Cyclotron Resonance Plasma Etching of $LiNbO_3$ Surface for Fabrication of Ridge Optical Waveguides. *J. Vac. Sci. Technol. A*, 16:2245–2251, 1998.

[43] F.D. Morrison, J.F. Scott, M. Alexe, T.J. Leedham, T. Tatsuta, and O. Tsuji. Use of the 'Mist' (Liquid-Source) Deposition System to Produce New High-Dielectric Devices: Ferroelectric-Filled Photonic Crystals and HF-Oxide and Related Buffer Layers for Ferroelectric-Gate FETs. *Microelectronic Eng.*, 66:591–599, 2003.

[44] M. Popovic, K. Wada, S. Akiyama, HA Haus, and J. Michel. Air trenches for sharp silica waveguide bends. *Lightwave Technology, Journal of*, 20(9):1762–1772, 2002.

[45] A. M. Radojevic, M. Levy, Jr. R. M. Osgood, A. Kumar, H. Bakhru, C. Tian, and C. Evans. Large Etch-Selectivity Enhancement in the Epitaxial Lift-Off of Single-Crystal $LiNbO_3$ Films. *Appl. Phys. Lett.*, 74:3197–3199, 1999.

[46] T. A. Ramadan, M. Levy, and Jr. R. M. Osgood. Electro-Optic Modulation in Crystal-Ion-Sliced Z-cut $LiNbO_3$ Films. *Appl. Phys. Lett.*, 76:1407–1409, 2000.

[47] Evan J. Reed, Marin Soljacic, and J.D. Joannopoulos. Color of Shock Waves in Photonic Crystals. *Phys. Rev. Lett.*, 90:203904, 2003.

[48] Chris B. Schaffer, Andre Brodeur, and E. Mazur. Laser-Induced Breakdown and Damage in Bulk Transparent Materials Induced by Tightly-Focused Femtosecond Laser Pulses. *Meas. Sci. Technol.*, 12:1784–1794, 2001.

[49] Marin Soljacic, Chiyan Luo, J.D. Joannopoulos, and Shanhui Fan. Non-Linear Photonic Crystal Mico-Devices for Optical Integration. *Opt. Lett.*, 28(8):637–639, 2003.

[50] N. S. Stoyanov, T. Feurer, D. W. Ward, and K. A. Nelson. Integrated Diffractive Terahertz Elements. *Appl. Phys. Lett.*, 82(5):674, 2003.

[51] N. S. Stoyanov, D. W. Ward, T. Feurer, and K. A. Nelson. Terahertz Polariton Propagation in Patterned Materials. *Nat. Mat.*, 1(2):95, 2002.

[52] Nikolay S. Stoyanov. *Phonon-Polaritons in Bulk and Patterned Materials.* Ph.d., Massachusetts Institute of Technology, 2004.

[53] N.S. Stoyanov, T. Feurer, D.W. Ward, and K.A. Nelson. Direct Visualization of the Gouy Phase Shift. In R.D. Miller, M.M. Murnane, N.F. Scherer, and A.M. Weiner, editors, *Ultrafast Phenomena XIII*, pages 214–216, Vancouver, Canada, 2002. Springer-Verlag.

[54] A. Taflove and S. C. Hagness. *Comupational Electrodynamics: The Finite-Difference Time-Domain Method.* Artec House Inc., Boston, 2000.

[55] H. F. Talbot. Facts Relating to Optical Science. *Philos. Mag.*, 9(4):401–407, 1836.

[56] C.H. Townes and A.L. Schawlow. *Microwave Spectroscopy.* Courier Dover Publications, 1975.

[57] Joshua C. Vaughan. *Two-Dimensional Ultrafast Pulse Shaping and its Application to Coherent Control and Spectroscopy.* Ph.d., Massachusetts Institute of Technology, 2005.

[58] K. Wang and D.M. Mittleman. Metal wires for terahertz wave guiding. *Nature*, 432(7015):376–379, 2004.

[59] David W. Ward. *Polaritonics: An Intermediate Regime between Electronics and Photonics.* Ph.d., Massachusetts Institute of Technology, 2005.

[60] D.W. Ward, E.R. Statz, and K.A. Nelson. Fabrication of polaritonic structures in LiNbO3 and LiTaO3 using femtosecond laser machining. *Applied Physics A - Materials Science & Processing*, 86(1):49–54, 2007.

[61] RS Weis and TK Gaylord. Lithium niobate: Summary of physical properties and crystal structure. *Applied Physics A: Materials Science & Processing*, 37(4):191–203, 1985.

[62] M.C. Yang, J.H. Li, H.T. Chen, and KJ Webb. Wavelength-scale functional waveguide mode conversion. *Lasers and Electro-Optics, 2003. CLEO/Pacific Rim 2003. The 5th Pacific Rim Conference on*, 1, 2003.

[63] M.C. Yang, J.H. Li, and K.J. Webb. Functional field transformation with irregular waveguide structures. *Applied Physics Letters*, 83:2736, 2003.

[64] M.C. Yang, J.H. Li, and KJ Webb. Functional waveguide mode transformers. *IEEE Transactions on Microwave Theory and Techniques*, 52(1):161–169, 2004.

[65] A. Yariv. *Quantum Electronics.* John Wiley & Sons, New York, 1989.

[66] A. Yariv. *Optical Electronics in Modern Communications.* Oxford University Press, New York, 1997.

[67] K. S. Yee. Numerical Solution of Initial Boundary Value Problems Involving Maxwell's Equations in Isotropic Media. *IEEE Trans. Antennas and Propagation*, 14:302–307, 1966.

[68] J. L. Young. Propagation in Linear Dispersive Media: Finite-Difference Time-Domain Methodologies. *IEEE Trans. Antennas and Propagation*, 43(4):422–426, 1995.

[69] J. L. Young and R. O. Nelson. A Summary and Systematic Analysis of FDTD Algorithms for Linearly Dispersive Media. *IEEE Antennas and Propagation Magazine*, 43:61–77, 2001.

[70] A. Zee. *Quantum Field Theory in a Nutshell.* Princeton University Press, Princeton, 2003.

[71] J. Zhang and D. Grischkowsky. Waveguide terahertz time-domain spectroscopy of nanometer water layers. *Optics Letters*, 29(14):1617–1619, 2004.

Eric R. Statz

EDUCATION

Massachusetts Institute of Technology

Ph.D. in Physical Chemistry, Spring 2008

"THz Phonon-polariton interactions with photonic structures and polaritonic crystals"

Pennsylvania State University

B.S. in Chemistry, B.S in Physics, with Honors in Chemistry and a Minor in Mathematics, Spring 2001

EXPERIENCE

Massachusetts Institute of Technology

Research Assistant, 2001-present. Conducted research into the interactions of terahertz frequency light with patterned optical systems including photonic crystals, waveguides, and quantum dots using amplified femtosecond lasers. Development of a novel Finite Difference Time Domain simulation of phonon polaritons in ferroelectric crystals. *Thesis Advisor: Keith A. Nelson*

Teaching Assistant 2001-2002. Taught recitations for classes in introductory chemistry, quantum mechanics, and thermodynamics.

Pennsylvania State University

Undergraduate Research, 1998-2001. Conducted research into copper and aluminum cluster reactions using Time of Flight Mass Spectrometry. *Thesis Advisor: A. J. W. Castleman Jr.*

Agilent Technologies

Summer Internship, Summer 2000. Investigated the application of UV-vis techniques to chemical sensing.

Hewlett Packard

Summer Internship, Summer 1999. Studied instrumental drift of a mass spectrometry based chemical nose. Independently developed computational methods of correcting for short and long term errors in the product.

SKILLS

Use and optimization of ultra-fast titanium sapphire oscillators, KHz regen and multipass amplifiers, and NOPAs. Design of various time domain optical experiments.

Femtosecond laser machining of ferroelectric crystals, design and fabrication of photonic crystals.

Simulation development and data processing in C, Java, Matlab, and Perl, including parallelization using MPI for a home designed and built cluster.

Instrumental control software design using Labview, C++, and Matlab. Experience with system administration of multi-user UNIX systems.

HONORS

Presidential Fellow, Massachusetts Institute of Technology, 2001
Schreyer Honors College, Pennsylvania State University
Presidential Scholar, Pennsylvania State University, 1998